# TESTING THE CHRONOMETRIC ACCURACY OF STELLAR EVOLUTION MODELS USING YOUNG STARS IN OPEN CLUSTERS

By

Phillip A. Cargile

Dissertation

Submitted to the Faculty of the

Graduate School of Vanderbilt University

in partial fulfillment of the requirements

for the degree of

DOCTOR OF PHILOSOPHY

in

PHYSICS

May, 2010

Nashville, Tennessee

Approved:

Dr. Keivan G. Stassun

Dr. David J. James

Dr. David A. Weintraub

Dr. Kelly Holley-Bockelmann

Dr. Kalman Varga

# DEDICATION

I would like to dedicate this thesis to my loving wife Emily Cargile

and to my grandmother Marcella McKone.

ACKNOWLEDGMENTS

First and foremost, I am most thankful for the supervision of Dr. David James and Dr. Keivan Stassun, without their enthusiastic encouragement and thoughtful guidance this thesis would not be possible. I would also like to thank the rest of the members of my committee as they have all played critical roles in my development as a scientist.

I am also extremely grateful for my many collaborators who have patiently helped me explore my area of research, particularly Dr. G. F. Benedict for his support and guidance while I was an undergraduate at the University of Texas. I would also like to specifically thank Dr. Robin Jeffries, Dr. Robert Mathieu, Dr. Tim Naylor, and Dr. Imants Platais for their thoughtful suggestions and help putting the material in this thesis together. I would also like to acknowledge my fellow graduate students at Vanderbilt University, particularly Alicia Aarnio and Saurav Dhital as they have been a constant source of creative ideas and thoughtful discussion.

I would like to acknowledge that the research presented in this thesis has been funded by the National Science Foundation (Career Grant AST-0349075, PI: Stassun, K.G.).

Last, but not least, I would like to thank my family: my wife Emily to whom this thesis is dedicated, my parents Robert and Colleen Cargile, and my siblings Anthony, Benjamin, and Monica. Without their love and support through out the years, I would not be the scientist, nor the person, I am today.

Table of Contents

# List of Tables

## List of Figures

# Chapter I

## MOTIVATION: OBSERVATIONALLY DETERMINING ACCURATE STELLAR AGES

Comparisons between empirical data and theoretical stellar evolutionary models indicate large systematic errors in the stellar ages resulting from different age-dating techniques. Nevertheless, these chronometric tools have been used to determine fundamental timescales in many different branches of astrophysics; from understanding the formation and evolution of planets (Silverstone et al., 2006), to determining a lower-limit on the age of the Universe (Krauss & Chaboyer, 2003). The primary scientific goal of this study, resulting from research presented in my thesis, is to perform a disparate range of independent tests of stellar age. This is achieved using multiple age-dating techniques of stellar samples in order to constrain, and inform future refinement of, the existing theoretical stellar evolutionary models.

In this chapter, we highlight several different age-dating techniques used in this thesis. First, we discuss commonly used method of determining stellar parameters from the Hertzsprung-Russell (H-R) diagram. Second, we describe the activity-rotation-age paradigm, a causal relationship between magnetic activity and stellar rotation which can be exploited in order to characterize stellar ages. Third, we discuss using the depletion of lithium in young stars to determine ages of open clusters. We end this chapter with an executive summary of this thesis.

## 1.1 The H-R Diagram

### 1.1.1 Pre-Main-Sequence Models

Fundamental properties, such as luminosity and temperature, of pre-main-sequence (PMS) stars were first calculated over a range of masses by Iben (1965) and Ezer & Cameron (1967b,a). These authors used numerical methods to solve the equations of stellar structure given by Henyey et al. (1955) and Hayashi (1961). In the 1990s, the development of large-scale computing facilities drove the development of stellar structure models that incorporated complex assumptions regarding their input physics. Many of these models produces tables of predicted stellar properties which are available to the community, notably models from D'Antona & Mazzitelli (D'Antona & Mazzitelli, 1994, 1997); Siess et al. (Forestini, 1994; Siess et al., 1997, 2000); and Baraffe et al. (Baraffe et al., 1998; Chabrier & Baraffe, 2000; Chabrier et al., 2007). An example of evolutionary tracks for stars of various masses, as predicted by the D'Antona & Mazzitelli models, is displayed in Fig. 1.1.

Comparisons of various PMS models have shown significant inconsistencies between theoretical predictions (Siess et al., 2000; Hillenbrand & White, 2004). In Fig. 1.2, we show the predicted evolution of luminosities and temperatures for different stellar masses. Systematic offsets are apparent in the model's predictions, particularly for stars with low-masses ($< 0.5$ $M_{\odot}$) and very young ages (towards the right of the evolutionary tracks). These inconsistencies are primarily due to the various flavors of input physics that each model incorporates, particularly in their treatment of

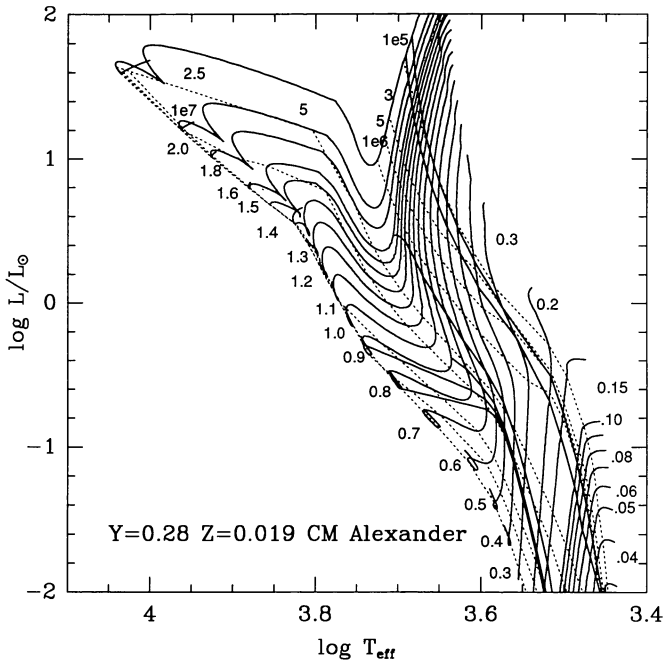


Figure 1.1: H-R diagrams comparing solar metallicity theoretical predictions of the D'Antona & Mazzitelli stellar evolutionary models for various mass stars. Solid lines are the individual mass tracks for stellar masses given at their left edge. Dotted lines are isochrones from 0.1 to 10 Myr and are labeled at their upper edge. This plot is reproduced from Fig. 3 in D'Antona & Mazzitelli (1994).

convection. The theoretical mass tracks plotted in Fig. 1.2 show the largest variation in predicted effective temperature between models. Indeed, it is predicted effective temperatures that are dictated largely by how the models incorporate convection throughout stellar interiors. Because of the relative complexity of a realistic treatment of convection, the majority of PMS models (*e.g.,* Siess et al., Baraffe et al.) rely on the mathematically simple Mixing Length Theory (MLT, Böhm-Vitense, 1958). This approach uses a single convective cell mixing length that is proportional to the pressure scale height in the modeled star. Typically, larger mixing lengths (more efficient convection) result in hotter evolutionary tracks, and yield lower ages for a

given position on the H-R diagram. The MLT models all predict a nearly adiabatic contraction for low-mass ($< 0.5$ $M_\odot$) PMS stars, causing stellar evolution paths to be close to vertical in the H-R diagram.

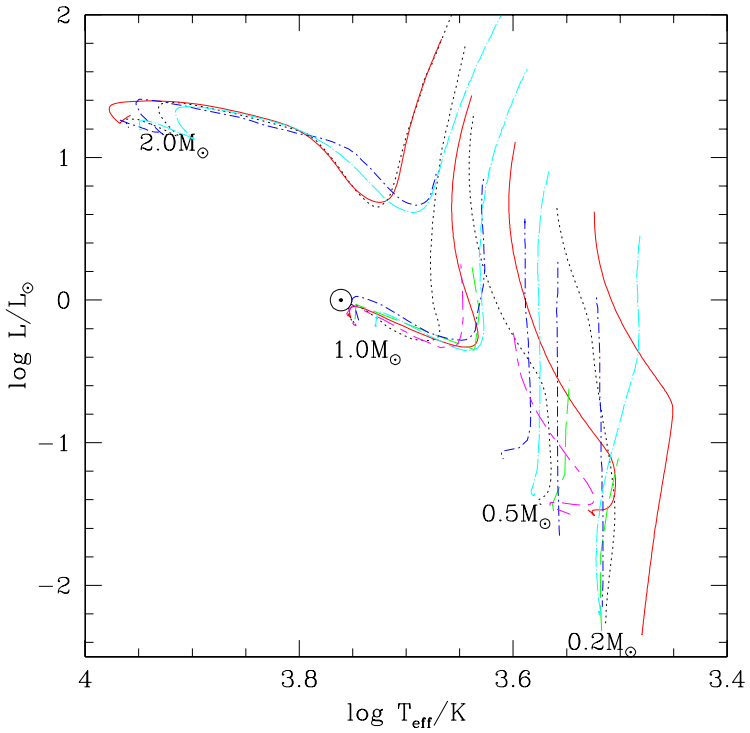


Figure 1.2: H-R diagram comparing theoretical predictions of various PMS stellar evolutionary models for different mass stars. The references are as follows: solid line – Swenson et al. (1994); dotted line – D'Antona & Mazzitelli (1997); long-dashed line – Baraffe et al. (1998); dot-short-dashed line – Palla & Stahler (1999); dot-long-dashed line – Siess et al. (2000); long-dash-short-dashed line – Yi et al. (2003). The position of the Sun is indicated with the solar symbol. This plot is reproduced from Fig. 1 in Hillenbrand & White (2004).

Alternatively, the D'Antona & Mazzitelli models use a more sophisticated treatment of convection called Full Spectrum Turbulence (FST, Canuto & Mazzitelli, 1991, 1992). This prescription of convection uses a variety of convective cell sizes, as com-

pared to one average cell size used in MLT. The effect of using a number of different convective cell sizes is that the overall convective flux increase, resulting in higher stellar effective temperatures compared to models using MLT. In addition, FST convection is found to cause PMS stars to be super-adiabatic at large radii (or young ages), resulting in a decrease in stellar temperature with contracting radius (*i.e.,* evolutionary track are not vertical in the H-R diagram). However, at smaller radii (or later PMS ages), FST convection returns to being adiabatic, resulting again in nearly vertical evolutionary tracks on the H-R diagram. Therefore, the largest difference in predicted stellar temperatures between PMS evolutionary models using MLT and FST are at young ages ($<$ 1 Myr) where differences of $\sim$400 K are observed. These systematic effective temperature offsets directly affect stellar ages derived from a star's position on the H-R diagram.

Another related effect on the predicted temperatures of stars is the treatment of opacity used by the models, particularly in stellar atmospheres. Stellar atmospheres are modeled in two ways, either using a computationally-simple gray approximation where the opacity is wavelength independent, or using a more realistic atmosphere that contains wavelength-dependent individual elemental and molecular opacity sources, as well as in some cases dust grains (*e.g.,* Hauschildt et al., 1999). Siess et al. (2000) report systematically lower effective temperatures ($\sim \Delta$ 100 K) for models that incorporate more realistic non-gray stellar atmospheres. They claim that this is a result of molecular blanketing in the outermost atmospheric layers (*e.g.,*

Chabrier et al., 1996).

Despite the known inconsistencies due to differences in input physics, PMS models have been heavily relied upon for determining the properties (ages, luminosities, temperatures, and masses) of young, low-mass stars, and are therefore a key fundamental input for current theories of stellar formation. For example, the initial mass function (the stellar formation history of a particular region), angular momentum evolution, and timescales for circumstellar disk evolution, and planet formation all hinge on ages measured directly from PMS models.

### 1.1.2 Upper-Main-Sequence Models

The upper-main-sequence *turn-off*, *i.e.,* the location on a Hertzsprung-Russell (H-R) diagram where higher-mass stars have depleted their hydrogen content in their cores, is one of the most commonly used tools for determining stellar ages. By comparing the highest mass star on a stellar population's main-sequence to main-sequence lifetime models for various stellar masses, one can derive a precise population age (Sandage, 1958; Mermilliod, 1981a,b; Meynet et al., 1993). As this dating technique relies on the placement of intrinsically bright high-mass stars on the H-R diagram (Demarque & Larson, 1964), it has been employed in dating of nearby open clusters, galactic globular clusters, as well as stellar populations in other galaxies (*e.g.,* Smecker-Hane et al., 2002).

Similar to PMS models, the first numerical models characterizing the evolution

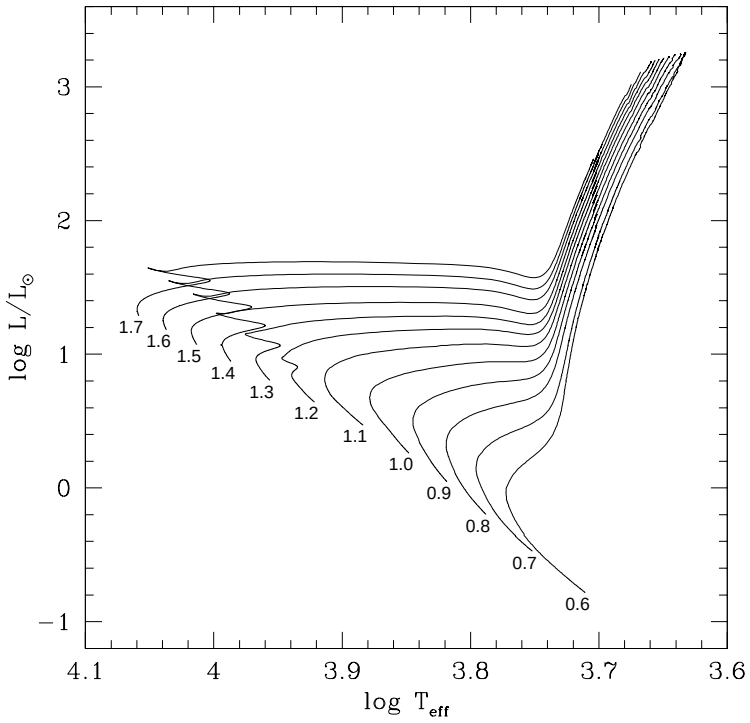


Figure 1.3: H-R diagrams comparing theoretical predictions of the Padova upper-main-sequence stellar evolutionary models for various mass stars. Solid lines are the individual mass tracks for stellar masses given at their left edge. This plot is reproduced from Fig. 2 in Girardi et al. (2000).

of the upper-main-sequence were produced in the 1960s (see Iben, 1967). Currently, the most often used high-mass stellar evolution models are from the Padova (Girardi et al., 2002) and Geneva (Schaller et al., 1992; Lejeune & Schaerer, 2001) groups. An example of the predicted H-R diagram for the Padova models is presented in Fig. 1.3. Current models incorporate complex input physics including varying composition, equations of state, internal and atmospheric opacities, as well as other effects important to high-mass stellar evolution, such as convective overshoot and mass-loss due to strong stellar winds.

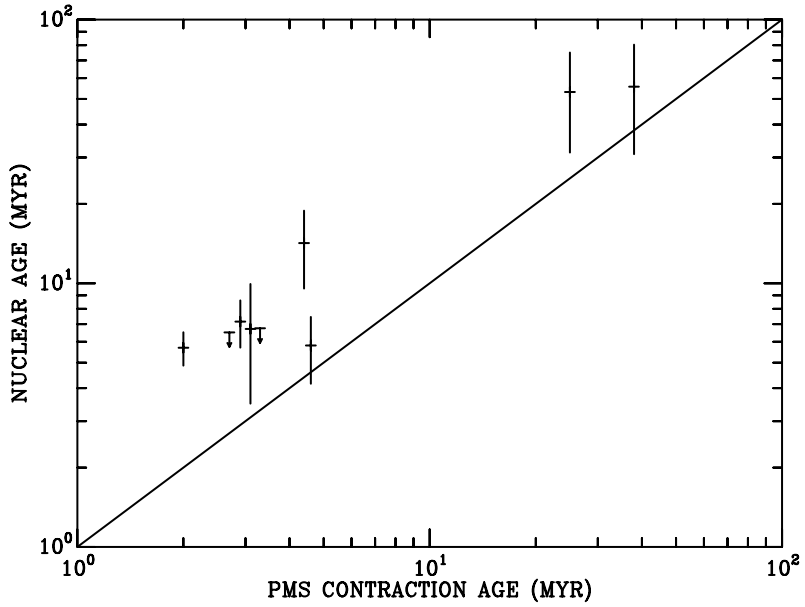


Figure 1.4: Measured upper- (nuclear) and pre-main-sequence ages for a collection of open clusters. The solid line indicates the one-to-one correlation. This figure is a reproduction of Fig. 9 in Naylor (2009).

Comparison between Padova and Geneva models show only slight differences between the predicted upper-main-sequence evolution (Naylor, 2009); however, observations have shown significant differences between the ages derived from upper-main-sequence models and PMS models. Fig. 1.4, a reproduction of Fig. 9 in Naylor (2009), displays a comparison of measured upper-main-sequence *turn-off* and PMS ages for individual open clusters. These data suggest a significant trend of older upper-main-sequence ages by a factor of 1.5-2 (also see similar studies by Chiosi et al., 1992; Meynet et al., 1993; Meynet & Maeder, 1997, 2000; Baraffe et al., 1998, 2002; Siess et al., 2000; Mayne & Naylor, 2008). Over the last few decades, authors have typically suggested that the problem is associated with upper-main-sequence models not

including realistic values for their input physics, specifically their treatment of convective overshooting (*e.g.,* Chiosi et al., 1992). Convective overshooting has the effect of mixing more hydrogen into the stellar core, thus prolonging main-sequence lifetimes. Therefore, by setting the amount of overshooting to be very small, and thus reducing upper-main-sequence ages, you can account for the observed age offset. However, Maeder & Mermilliod (1981) show that a moderate amount of core overshooting is necessary to model the upper-main-sequences of several benchmark open clusters, such as the Pleiades and Hyades. More recently, Naylor (2009) explains the offset seen in Fig. 1.4 is a result of predicted PMS ages being less robust than upper-main-sequence ages, citing the lack of a single, consistent, and absolute PMS age scale due to the large systematic discrepancies in the stellar parameters predicted by the various PMS models (particularly luminosities and temperatures, see Section 1.1.1). Nevertheless, the physical mechanisms proposed to be behind the observed inconsistencies seen in Fig. 1.4 are difficult to empirically constrain (*e.g.,* internal convection), therefore this issue remains a matter of debate.

## 1.2 Activity-Rotation-Age Paradigm

Whether it is confinement of plasma in coronal loops or coronal heating mechanisms, there is a fundamental relationship between magnetic fields produced and amplified by a rotationally induced dynamo and X-ray emission seen in solar-like stars. Therefore, it is not surprising that a correlation between magnetic activity and

stellar rotation rates is observed. Here, we describe the current understanding of this relationship and how it evolves with age. In addition, it outlines the current theories on this so called Activity-Rotation-Age Paradigm (ARAP), as well as observational support for its existence.

### 1.2.1 Dynamo – Stellar Wind Feedback Loop

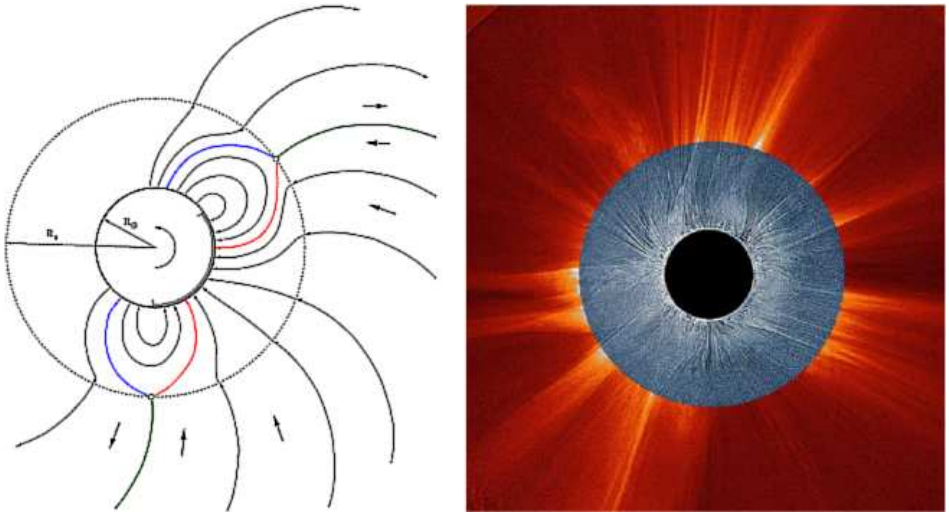

Figure 1.5: (*left*) A sketch of open and closed magnetic field lines in the corona of the Sun as seen from above the Solar North pole. The outer circle in the plot indicates the Alvén radius ($R_s$), lines that extend beyond this radius are considered "open". (Figure from Schwenn, 2006) (*right*) Comparison image of the Sun in eclipse taken simultaneously with the space based solar observatory, SOHO, (outer image) and a white-light observation (inner image). Note the very similar structures seen in the sketch and in the image, namely closed field lines producing high levels of coronal emission, and streaming open field lines. (Figure from Koutchmy et al., 2004)

Parker (1960) first showed that plasma confined to magnetic field lines in stellar corona could escape into space if they extend beyond a certain radius, called the

Alfvén radius. At this radius, the particles in the hot coronal plasma have thermal velocities greater than the escape velocity of the confining magnetic tube and the star, therefore the magnetic field lines that extend to Alvén radius are considered "open", allowing plasma to run along them and stream into space, resulting in a stellar wind (see Fig. 1.5). The result of these open field lines is a loss of mass and angular momentum associated with the charged ions in the stellar wind. Kawaler (1988) presents a model of the angular momentum evolution in solar-like stars using stellar winds as the method of mass loss. The general outline of this model is as follows: the star loses angular momentum through a solar-like magnetized wind, resulting in the star spinning down, thereby weakening the $\Omega$-effect (*i.e.,* the rotation dependency) in the $\alpha\Omega$ dynamo. Since the dynamo is the mechanism for amplifying magnetic fields, it affects the buoyancy of magnetic flux tubes. Therefore, reducing the strength of the dynamo in turn reduces the number and strength of magnetic field lines reaching the stellar surface. This results in a reduction of stellar winds and angular momentum loss. This negative feedback loop converges at a characteristic rotation period that only depends on mass and age. Soderblom et al. (1993) showed that this convergence typically takes place on the order of $\sim$100 Myr (see Fig. 1.6).

Because of the fundamental causal relationship between magnetic fields and stellar rotation, one would then expect that observed magnetic activity, as a result of heated coronal plasma, would decrease as a function of slower rotation rate. Skumanich (1972) first empirically determined that in field stars, Hyads, and the Sun, $Ca^{+}$

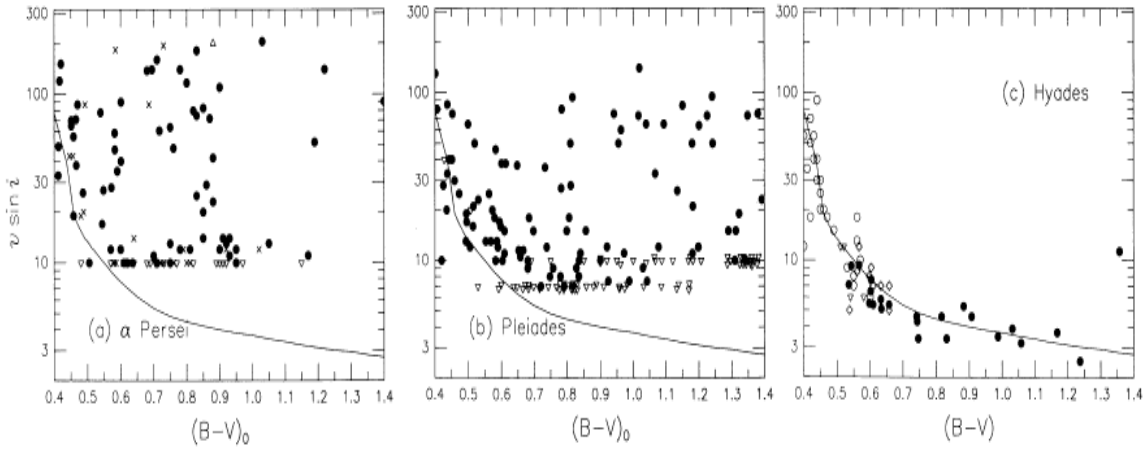


Figure 1.6: Distribution of projected rotation velocities (Vsin $i$) for three open clusters: (a) $\alpha$ Persei (Age - 80 Myr), (b) Pleiades (Age - 125 Myr), and (c) Hyades (Age - 650 Myr). The fit to the Hyades data is marked by the solid line. Downward facing triangles denote velocity upper limits. (Figures from Soderblom et al., 1993)

emission, as an indicator of magnetic activity, correlated as a linear power law with rotation rate (Vsin $i$) of the star and inversely proportional to the square root of the star's age. Kawaler (1988) accurately replicated these finding in their angular momentum evolution model. Thereafter, Pallavicini et al. (1981) showed a similar trend for X-ray luminosity ($L_x$) and rotation rate, $L_x \propto (\mathrm{Vsin}\, i)^2$, for stars with spectral types ranging from G to M (see Fig. 1.7). They also find that for higher mass stars, *i.e.,* O to F spectral types which possess little or no surface convection, little or no X-ray emission is seen, along with a lack of dependence of observed X-ray emission on stellar rotation rates. Pallavicini et al. (1981) argue that this demonstrates further evidence that a convection zone is an essential part of stellar X-ray emission.

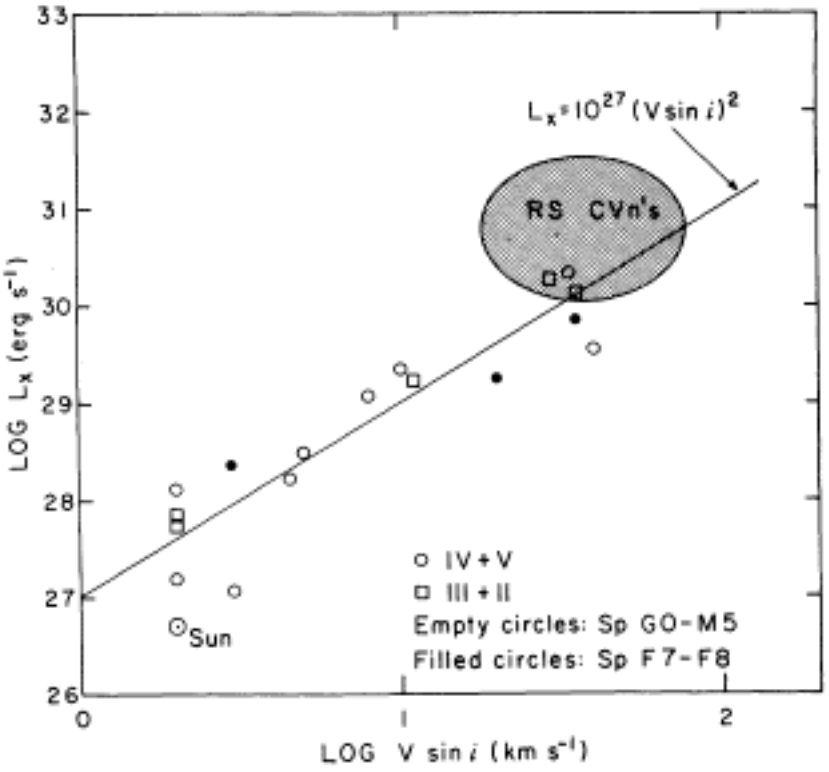


Figure 1.7: Scatter plot X-ray luminosity ($L_x$) as a function of Vsin $i$ for main-sequence stars with spectral types F7 to M5. Different points indicate different luminosity classes. The solid line is a linear fit to the data resulting in the quoted relationship between X-ray luminosity and rotation velocity. (Figure from Pallavicini et al., 1981)

### 1.2.2 Rossby Number: The Magnetic Activity-Convection Connection

In order to further describe the relationship between X-ray activity and the underling stellar dynamo, Noyes et al. (1984) and Mangeney & Praderie (1984) introduced the use of a Rossby number, $R_0$. The Rossby number is defined as the ratio of rotation period, $P_{rot}$, to the convective turnover time, $\tau_c$, which is only dependent on stellar mass. In a sense, this number tells you the strength of the rotationally induced dynamo as a function of the mass dependent efficiency in producing observed magnetic

activity from the internal magnetic fields, in other words, stars with higher $R_0$ are more convectively efficient than ones with lower numbers.

It is observed that the fractional X-ray to bolometric luminosity is well described by the inverse square of the Rossby number (Pizzolato et al., 2003) for stars with Rossby numbers greater than $10^{-1.2}$. In other words, for two stars with identical masses (and $R_0 > 10^{-1.2}$), you would expect the star with a higher rotation rate to show higher levels of magnetic activity. Conversely, for two stars having the same rotation rate, you can predict that lower coronal X-ray emission level will be seen in the higher mass star. You can also make the same argument with activity and age using the Skumanich-relationship (*i.e.,* $P_{rot} \propto Age^{-\frac{1}{2}}$). From this relationship, you can derive that for two stars of the same age, the higher mass star will have lower levels of X-ray emission. Or, for two stars of the same mass, the older star will have lower X-ray activity levels. These relationships are the fundamental principles behind the Activity-Rotation-Age Paradigm.

### 1.2.3 Saturation

The description of the X-ray emission as a function of age and rotation holds for many main-sequence stars. However, observations show that as one goes to higher rotation rates, or lower masses for stars of the same age, the fraction of X-ray to bolometric luminosity levels off at $\sim 10^{-3}$ (Vilhu, 1984; Vilhu & Walter, 1987). This phenomenon, called X-ray saturation limit, appears to extend all the way along the

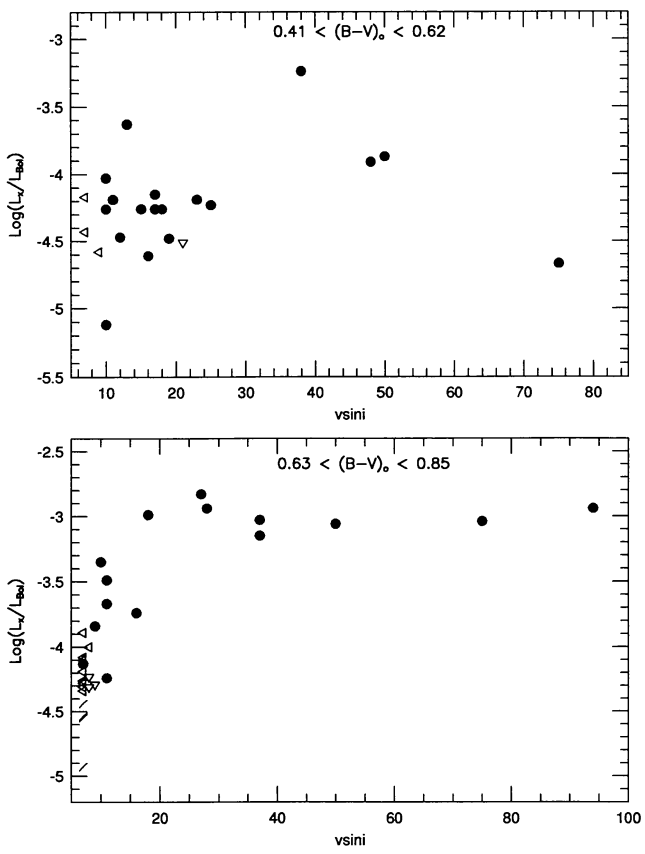


Figure 1.8: Ratio of X-ray to bolometric luminosity versus Vsin $i$ for Pleiades members. The distributions are divided up over the color ranges given at the top of each plot. Downward facing arrows indicate a X-ray luminosity upper-limit was detected, leftward facing arrows indicate calculated Vsin $i$ was below sensitivity level of survey. (Figure from Stauffer et al., 1994)

main sequence from G-type stars to the latest M dwarfs (Fleming et al., 1993). Using ROSAT X-ray data for the Pleiades open cluster, Stauffer et al. (1994) found two interesting trends: first, stars with spectral-types earlier than ∼G-type do not show any significant trend between X-ray emission and rotation (see top plot of Fig. 1.8); and second, for Pleiads with later spectral-types, X-ray emission is seen to increase with stellar rotation up to Vsin $i <\sim 15$ km s$^{-1}$, while stars with higher rotation rates

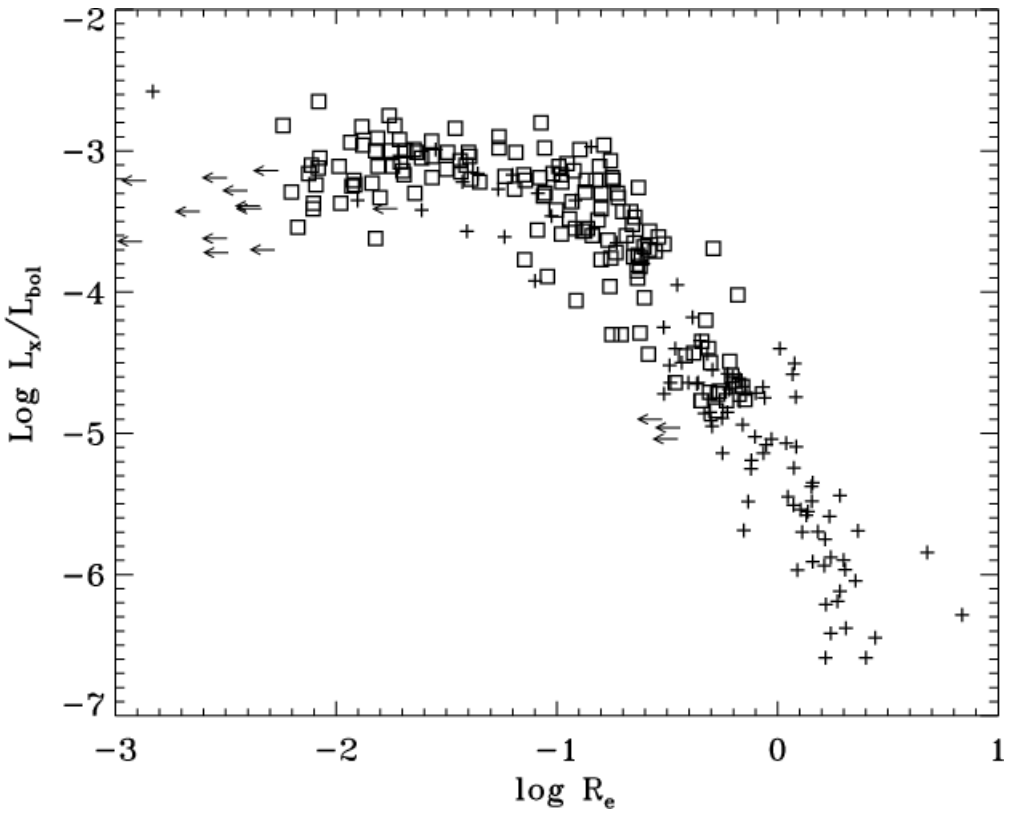


Figure 1.9: X-ray to bolometric luminosity ratio versus Rossby number ($R_e = P/\tau_c$) for field (*crosses*) and cluster (*open squares*) stars. Cluster stars are from a sample of X-ray sources with known rotation periods in the Pleiades, $\alpha$ Persei, IC 2602 and IC 2391 (ages from ∼50-100 Myr). Leftward arrows indicate field stars with periods derived from V$\sin i$ data. (Figure from Pizzolato et al., 2003)

exhibited saturated levels of X-ray emission (see bottom plot of Fig. 1.8).

More recently, (Pizzolato et al., 2003) compiled an extensive catalog of X-ray photometry and stellar rotation data for 149 dwarf stars with a color range of B−V=0.5-2.0; 110 field stars and 149 open cluster dwarfs with an age range of $\sim 40 - 650$ Myr. With this large amount of data, they were able to place quantitative empirical constraints on the characteristics of X-ray emission in solar-type stars. Namely, that there are two X-ray emission regimes, one in which the ratio of X-ray to bolometric

luminosity is proportional to the Rossby number, and the other in which X-ray emission is saturated (see Fig. 1.9), with the dividing line between regime located at a $R_0 = 10^{-1.2}$. They also empirically determined the rotation period, as a function of bolometric luminosity, that defines this boundary to be $P_{sat} \sim 1.2(L_{bol}/L_{\odot})^{-\frac{1}{2}}$ days, which they claim to be accurate to within a factor of two.

The physical causes for saturation are not well understood. Hypotheses that have been found in the literature include the following: (1) X-ray emission saturation is a direct consequence of the internal dynamo saturating (Gilman, 1983; Vilhu & Walter, 1987). In other words, at some rotation rate the dynamo cannot amplify the stellar magnetic fields any further. (2) The surface is completely covered with magnetically active regions. It has been shown that if the entire stellar surface was covered with magnetic flux, the star's $L_x/L_{bol}$ value would fall short of $10^{-3}$ by one order of magnitude (Vilhu, 1984). Also, there have been detections of rotational modulation in the X-ray emission of some saturated stars (e.g. Collier Cameron et al., 1988). These findings subsequently cast doubt on the idea of completely filling the stellar surface with active regions. (3) Jardine & Unruh (1999) proposes that as rotation increases, the radius where centrifugal forces balance the star's gravity (the co-rotation radius) becomes smaller. For very fast rotation rates, this co-rotation radius eventually crosses the outer X-ray coronal radius. This will effectively "open" any magnetic field loops that extend past this radius, thus stripping the confined plasma. This would result in limiting the available volume of confined plasma which

produces the observed X-ray emission.

At very high rotation rates, a decrease in $L_x/L_{bol}$ has been observed (Prosser et al., 1996; James et al., 2000). Currently, this phenomenon, called supersaturation, has been relatively unconstrained due to a paucity of supporting observational evidence; for example, the comprehensive supersaturation study of James et al. (2000) cautiously determined from ∼10 stars that supersaturation is exhibited in stars with rotational velocities $> 100$ km s$^{-1}$. Much like with saturation, the mechanism behind this anomaly is still in dispute. Some examples of proposed physical causes include that the dynamo itself is self-limiting, maybe via a Lorentz back-reaction and shear stresses across field boundaries (Charbonneau & MacGregor, 1992), or that X-ray emitting coronal volume of rapid rotators is reduced via centrifugal stripping (Jardine & Unruh, 1999).

### 1.2.4 X-ray Emission in Very-Low-Mass and PMS Stars

Later than a spectral-type of mid-M, main-sequence stars are expected to be fully convective (Chabrier & Baraffe, 1997). The solar-like $\alpha\Omega$ dynamo can therefore no longer operate due to the lack of a tachocline. However, a rotation independent, small-scale ($\alpha^2$) dynamo may still exist. One might expect that this change to a small-scale dynamo would perhaps alter the observed X-ray emission, due to changes in the topology of the magnetic fields. However, observations do not seem to support this idea. Studies of volume limited M-dwarf samples show that there are no dis-

continuities in X-ray characteristics as you move to lower masses (e.g. the maximum levels of $L_x/L_{bol}$ are $\sim 10^{-3}$, Fleming et al., 1993). This has also been seen in with other magnetic activity indicators in much larger samples (*e.g.,* West et al., 2008). Therefore, it must be the case that if a change from a solar-like dynamo does take place, then the efficiency of this other type of dynamo must be similar to the $\alpha\Omega$ dynamo. Models show that classical and weak-lined T Tauri star have interiors which are fully convective (Chabrier & Baraffe, 1997). Therefore, the study of magnetic field production in fully convective stars is of great interest to understanding the angular momentum evolution of these pre-main-sequence stars.

### 1.3 Age-Dependent Abundances of Light Elements: Lithium Depletion

As low-mass stars ($< 0.6$ M$_\odot$) approach the main-sequence, their natal Li is rapidly destroyed by proton burning in regions where their interior temperature reaches above $\sim 2.5$ MK. Since the rate at which the central temperature of a young star changes is a sensitive function of stellar mass and age (Bildsten et al., 1997; Ushomirsky et al., 1998), determining the mass at which stars in an open cluster fully deplete their initial Li content allows us to measure the cluster age – the so-called *lithium depletion boundary* (LDB) method. For stars having internal temperatures $> 2.5$ MK and having very deep convection zones, thus allowing efficient convective mixing of lithium-rich material to Li-burning depths, the lithium depletion rate is rather rapid ($< 1$ Myr, see Fig. 1.10). In a given open cluster therefore, the mass-segregation

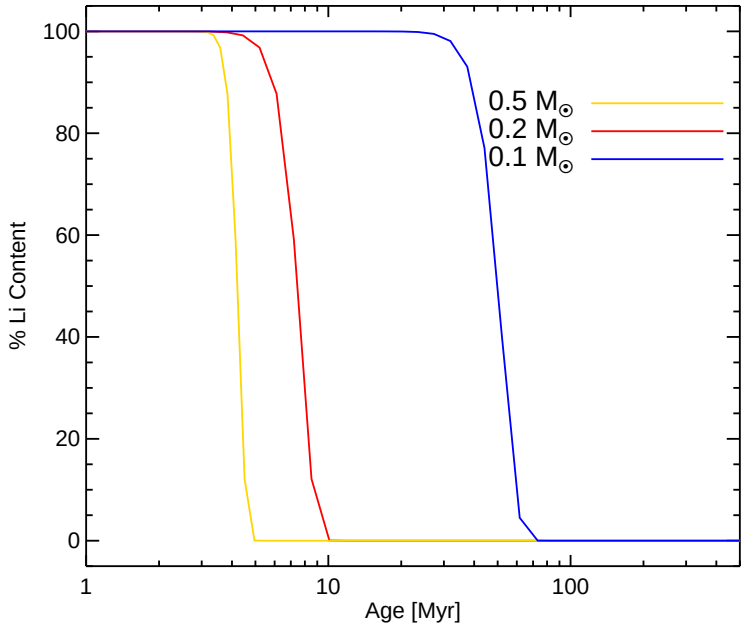


Figure 1.10: Percentage of natal Li content in low-mass stars as a function of stellar age. Li tracks are taken from the PMS models of Siess et al. (2000) for the masses given at the top-right of the plot.

of stars having fully depleted their natal lithium and those retaining their original lithium content is quite marked, and is easily identifiable (*e.g.,* see Fig. 1.11).

LDB ages are inherently difficult to measure due to the necessity of recording spectra in very faint, low-mass stars that have not yet depleted their natal lithium, typically a cluster's mid- to late-M dwarfs. Therefore with current telescopes, even 8-10 m class ones, we can only determine LDB ages for the nearest open clusters. Furthermore, this technique is most sensitive to young stellar ages, ∼10-250 Myr. At earlier ages, there aren't enough stars with depleted Li to define the depletion boundary; at later ages, brown dwarfs, which will never reach 2.5 MK in their cores, are the only very low-mass objects to still have their natal lithium content. These

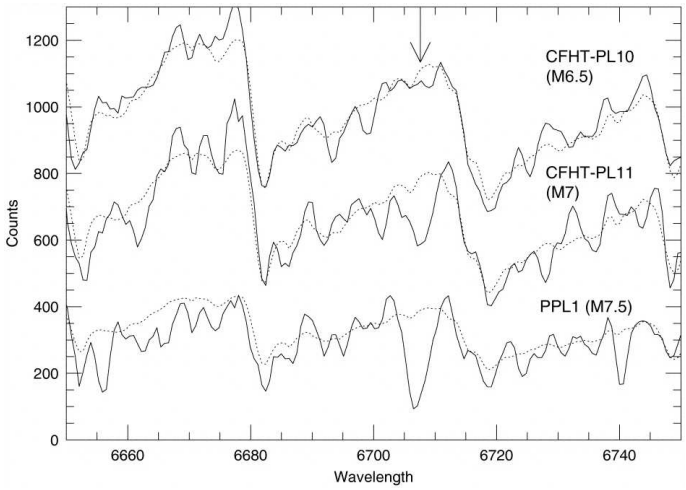


Figure 1.11: Catalog of spectra for the region around the Li 6707 Å feature (identified with arrow) for stars in the Pleiades taken from Stauffer et al. (1998). The spectra are plotted in descending mass from top to bottom. Plotted with the dotted line is the spectrum of a field M6 dwarf, assumed to have depleted its initial Li content. Li is not seen in the M6.5 star, but is clearly present in the later type stars, thus the LDB is located between M6.5 and M7 spectral-types. (Figure from Stauffer et al., 1998)

limitations have resulted in only five open clusters having LDB age determinations: Pleiades (125±8 Myr; Stauffer et al., 1998), $\alpha$ Persei (90±10 Myr; Stauffer et al., 1999), IC 2391 (50±5 Myr; Barrado y Navascués et al., 1999, 2004), NGC 2547 (35±4 Myr; Jeffries & Oliveira, 2005), and IC 4665 (28±7 Myr; Manzi et al., 2008).

## 1.4 Executive Summary

The main focus of this thesis is to address the chronometric accuracy of stellar ages. By employing various methods, we can verify and quantify observed systematic trends in calculated stellar ages. The results of the work in this thesis provides empirical limits on the precision of theoretical fundamental parameters, particularly stellar ages, and can be used to constrain and calibrate stellar evolution models.

In Chapter II, we describe the results from a extensive study of the PMS eclipsing binary Par 1802. Through detailed orbit and light-curve solutions, from which we measured individual component masses, effective temperatures, luminosities, and radii, we have identified Par 1802 to be composed of two young stars with nearly identical masses of 0.4 $M_{\odot}$, making this system the first discovered pair of PMS low-mass "identical twins." Par 1802 A & B, being of the same mass and presumably coeval, provide us with a unique opportunity to test the identical astrophysical nature of young equal-mass stars. We also use our measured physical properties of Par 1802 A & B to directly test the accuracy of the various PMS models. Surprisingly, our analysis show this system to have dissimilarities in the component's individual fundamental properties (temperatures, radii, and luminosities). These offsets can be explained by an age offset of ∼300,000 years, thus perhaps providing a lower-limit for the true coevality of binary systems. This chapter was published as Cargile et al. (2008) and Stassun et al. (2008).

Chapter III details our study that models empirical H-R diagrams using isochrones from PMS and upper-main-sequence models. We first outline the SMARTS Open Cluster Survey (SPOCS), an observing program designed to obtain high-fidelity standardized photometry for several southern open clusters. Employing a new statistical approach to modeling cluster sequences on empirical H-R diagrams, we explore the ages and distances of two open clusters, IC 4665 and Blanco 1. This new statistical approach, called Tau-squared ($\tau^2$) isochrone modeling, involves a maximum-

likelihood technique for fitting two-dimensional isochrone models to stellar data in color-magnitude space. This method allows the derivation of formal uncertainties on cluster ages and distances based on correlated errors in colors and magnitude, as well as handles complexities of modeling color-magnitude diagrams (*e.g.,* a population of unresolved photometric binaries). We use the results from this modeling procedure to identify systematic offsets between the best-fit isochrone ages for these cluster's upper- and pre-main-sequences, and we explore these derived cluster ages in the context of global trends seen in other open clusters. More specifically, we find upper- and pre-main-sequence ages of 36±9 and 42±12 Myr for IC 4665, and $115^{+2}_{-11}$ and 125±19 Myr for Blanco 1, respectively. We confirm that these ages show similar discrepancies observed in the derived upper- and pre-main-sequence isochrone ages of other open clusters. This chapter has been submitted for publication as Cargile & James (2010).

In Chapters IV, we explore age-dating techniques for stars in open clusters based on magnetic activity. First, we report a new analysis of X-ray data for Blanco 1 in order to investigate the relationship between magnetic activity and age in young stars. We provide observational data, using the distribution of stellar X-ray luminosity for the cluster, in order to constrain relative magnetic activity-age for Blanco 1, and provide details on placing its stellar X-ray emission distribution in the context of other open clusters. This is published as Cargile et al. (2009). We also include an epilogue to this chapter that contains additional analysis of rotation and X-ray emission distributions for Blanco 1, a direct comparison between the observed X-ray

emission in Blanco 1 and IC 4665, and provide details on ways to quantitatively calibrate magnetic activity and age using open clusters. This will eventually be published as Cargile & James (in prep.).

We conclude with a chapter describing current and future implications of this thesis as we work towards reconciling empirical and model-predicted stellar ages. We first address placing empirical constraints on the treatment of convection in stellar models using results from our study of Par 1802, as well as our isochrone modeling of IC 4665 and Blanco 1. In the second section of the chapter, we provide details on an on-going project to establish the LDB of Blanco 1. This includes some preliminary results, as well as their possible implications on PMS models, specifically the influence of inflated radii on their predicted ages. This is not yet published work, but rather represents preliminary ideas that will mature in future papers.

In summary, this thesis attempts to combine multiple age-dating methods to test the chronometric accuracy of theoretical stellar evolutionary models. Namely, we employ direct empirical measurements of components of a young eclipsing binary system, isochrone modeling of the upper- and pre-main-sequences, and empirically calibrated, time-dependent trends in stellar activity. We also investigate future work that may provide interesting insight into missing physics in models of stellar evolution.

We begin each chapter with a preface providing a brief background into that chapter's subject matter, and we have noted the publication status of the chapter content when applicable. We would like to note that this is an applied thesis covering

a extensive range of topics. Our goal is to not only provide scientific merit for the work completed, but also contribute a procedural outline to replicate our analysis for future studies.

# Chapter II

## LOW-MASS ECLIPSING BINARY IN ORION

(Published as: Cargile et al. 2008 ; Stassun et al. 2008)

Low-mass stars constitute the majority of stars found in stellar populations (e.g., Henry & McCarthy, 1993) and are therefore of key interest in the testing and calibrating models of stellar formation and pre-main-sequence (PMS) evolution (e.g., Hillenbrand & White, 2004). Unfortunately, only five PMS empirical mass determinations are known below 0.5 $M_{\odot}$. One of these mass measurements (Prato et al., 2002) is based on distance-dependent circumstellar disk kinematics, and the other four (Stassun et al., 2006, 2007; Irwin et al., 2007) are recently discovered eclipsing binary systems.

Eclipsing binary stars are powerful tools with which to empirically measure precise stellar parameters, including individual masses, effective temperatures, radii, and luminosities for the component stars, all in a distance-independent manner. The physical parameters determined in these system provide crucial tests to be performed on models of stellar evolution with unprecedented clarity. This is particularly true for PMS eclipsing systems where the properties of the component stars are changing rapidly as a function of age. Indeed, eclipsing systems have played a fundamental role in revealing the subtle biases of PMS models. For example, under-prediction

of stellar radii for low-mass stars (Ribas et al., 2008), assumed to be the effect of magnetic activity, as well as showing the importance of convection and rotation on predicted temperatures and luminosities (Torres et al., 2009).

In this chapter, we identify Parenago 1802 (hereafter Par 1802) as a PMS double-lined spectroscopic and eclipsing binary star system in the Orion star-forming region. We will describe the observation, reduction, and analysis of these extensive photometric and spectroscopic datasets. We will also include details of our combined radial velocity and light curve model, and finally compare our measured physical parameters of the two components of Par 1802 to the current PMS models. Most of the material presented in this chapter has been published in either Cargile et al. (2008) or Stassun et al. (2008).

## 2.1 Previous Studies of Par 1802

The first documented photometric observations of Par 1802 came in the Parenago (1954) survey of the Orion Nebula Cluster (ONC). Their catalog lists Par 1802 as a non-varying star with visual photographic magnitude of 15.1. Par 1802's membership to the ONC was determined in the Jones & Walker (1988) proper motion survey; they find Par 1802 (#363) to have a 98% ONC membership probability, based on its kinematics.

More recently, Hillenbrand (1997), in a low-resolution spectral survey of the ONC, obtained a spectral type of M2 for Par 1802. Also, Carpenter et al. (2001) included

Par 1802 in a time series, $JHK_s$ photometric survey as an extension of the 2MASS project. This survey produced photometric values of J= 11.10±0.05, H= 12.50±0.03, and $K_s$ = 9.97±0.04 mag for Par 1802. We derive an infrared reddening of $E(J-K_s)$ = 0.29 for Par 1802 using a visual extinction of $A_V$ = 0.72 mag given by Hillenbrand (1997) and the reddening law provided in Savage & Mathis (1979). Correcting for this reddening, the intrinsic $J-K_S$ color from the Carpenter et al. (2001) photometry is 0.87. Using the Kenyon & Hartmann (1995) temperature to color conversion, the effective temperature of $\sim 3500K$ (Hillenbrand, 1997) implies an intrinsic color of $J - K_s = 0.84$. Therefore, we confirm that the spectral type given by Hillenbrand (1997) is consistent with the observed $JHK_s$ colors measured by Carpenter et al. (2001) and further gives evidence that Par 1802 is a low-mass member of the ONC. The Carpenter et al. (2001) survey also produced preliminary infrared light curves that show variability in all three filters ($JHK_s$), and they use the Stetson variability index (a common statistical tool to determine photometric variability) to list Par 1802 as a likely variable star.

Stassun et al. (1999) included Par 1802 in a December 1994 photometric monitoring survey of the ONC, but it was not flagged as a candidate eclipsing binary until it was observed spectroscopically with the WIYN multi-object spectrograph (MOS) in January 1997, where it showed a clear double-lined spectrum. *Ex post facto* examination of the $I_c$-band light curve revealed what appeared to be possible eclipse events, though the limited time coverage of those preliminary data coupled with the

system's inherent variability prevented a confident identification of eclipses. Par 1802 was subsequently monitored photometrically and spectroscopically over multiple observing seasons (see Section 2.2), which confirmed its identification as an eclipsing binary.

## 2.2 Observations

Here, we describe our extensive observing program to characterize the properties of the stars in this PMS eclipsing binary system.

### 2.2.1 Photometry

An in-depth discussion of the light-curve reduction procedure and analysis is presented elsewhere (Gomez Maqueo Chew, 2010, Gomez Maqueo Chew et al., in prep.); here, we briefly describe some of the pertinent details of these photometric observations. We imaged Par 1802 repeatedly from December 1994 to March 2007 with the 0.9 m telescope at the Kitt Peak National Observatory (KPNO) and with the Small and Medium Aperture Research Telescope System (SMARTS) 0.9 m, 1.0 m and 1.3 m telescopes at the Cerro Tololo Inter-American Observatory (CTIO). In total, we acquired 2,209 flux measurements on 418 separate nights and with an average cadence of five or six measurements per night. The typical relative uncertainty in the individual flux measurements is $\sim$1%. Employing a phase dispersion minimization analysis, we find an unambiguous periodic signal of P=4.673843$\pm$0.000068 days. In

Fig. 2.1 we plot the relative $I_c$-band light-curve for Par 1802 along with our best-fit orbit model (see Section 2.4).

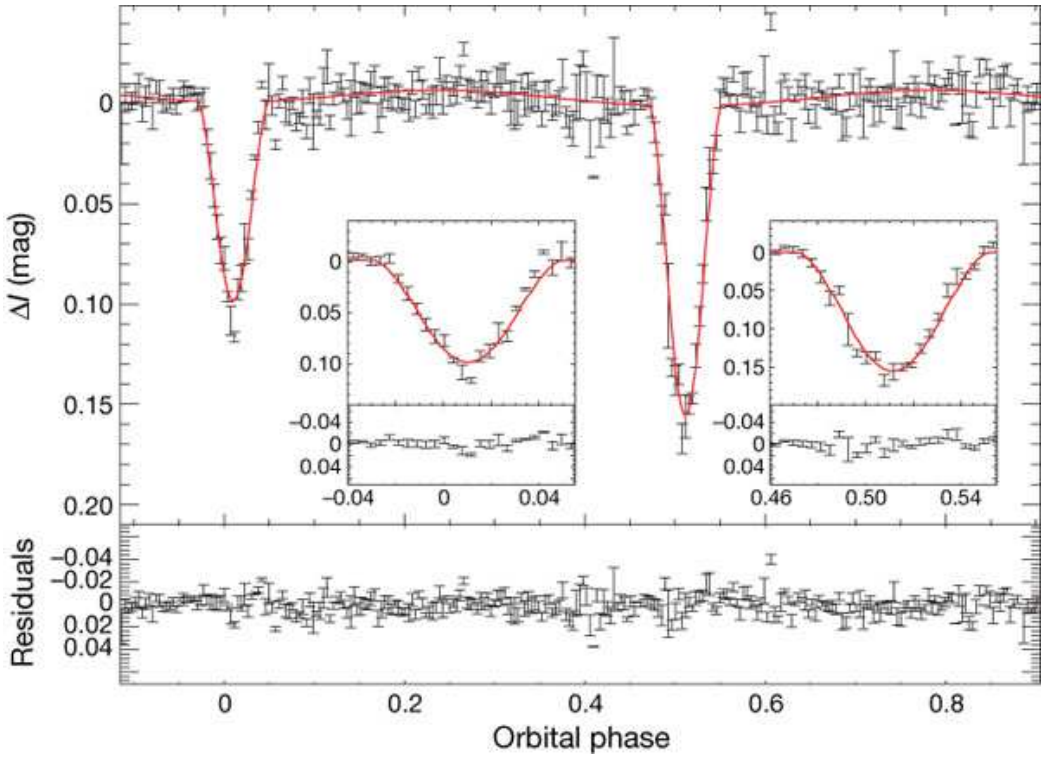


Figure 2.1: Differential $I_c$-band ($\Delta I_c$) photometry for Par 1802, folded on the period derived from our best-fit orbit solution (*red line*; see Section 2.4) and phased to periastron passage (time of closest approach of the two stars). The primary (smaller star travels behind larger star) and secondary (larger star travels behind smaller star) eclipses are found at phases of ∼0.5 and 0.0, respectively. For clarity, we plot our photometric dataset re-sampled into 250 equally spaced bins; each point represents ∼9 measurements. We do note that our best-fit orbit solution used the full unbinned dataset. Insets show the primary (*right*) and secondary (*left*) eclipses in detail, and the light-curve residuals relative to the model (observed minus calculated) are shown at the bottom. Figure adapted from Stassun et al. (2008).

### 2.2.2 Spectroscopy

#### 2.2.2.1 WIYN MOS

We observed Par 1802 with the WIYN [1] Multi-Object Spectrograph (MOS) on 8 nights between January 1997 and December 2004 (see Table II.1). We used the echelle grating centered at 6,400 Å, providing a wavelength coverage of 6,250–6,550 Å with a resolving power of R $\approx 12,000$. This spectral region contains a wealth of stellar spectral lines and is thus well suited to radial-velocity measurements via cross correlation. Typical exposure times were 2 hrs divided into 3 sub-exposures for cosmic ray rejection, yielding S/N $\sim$ 20 per resolution element for most observations. The spectra were reduced using the IRAF [2] *DOHYDRA* task. We flat-fielded the spectra using dome flats and wavelength-calibrated them using Th–Ar lamp spectra, each obtained with the same fiber configuration as was used for the target observations. Several fibers in each pointing were placed on blank "sky" positions. Because these fibers were typically placed within the nebula as well, they actually represent the sum of the true sky (solar + telluric) spectrum and the nebular spectrum at that location. For each pointing, the various sky fibers were median-combined to produce a single sky spectrum for that pointing, which was then subtracted from the target spectrum. Due to the small scale variations in the nebulosity of the ONC, the median-combined sky spectrum did not completely remove the large nebular emission lines.

[1] The WIYN Observatory is a joint facility of the University of Wisconsin-Madison, Indiana University, Yale University, and the National Optical Astronomy Observatories.

[2] IRAF is distributed by the National Optical Astronomy Observatories, which are operated by the Association of Universities for Research in Astronomy, Inc., under cooperative agreement with the National Science Foundation(Tody, 1993).

Table II.1. Par 1802 Radial Velocity Measurements

| HJD[a] | $RV_A$ (km $s^{-1}$) | $RV_B$ (km $s^{-1}$) | Telescope[b] | O−$C_A$[c] (km $s^{-1}$) | O−$C_B$[c] (km $s^{-1}$) | Phase[c] |
|---|---|---|---|---|---|---|
| 0473.6992 | 89.2 ± 1.8 | -19.4 ± 3.9 | W | 11.1 | 12.9 | 0.70 |
| 1887.9334 | -39.8 ± 2.6 | 76.9 ± 2.8 | W | -3.5 | -2.1 | 0.28 |
| 1923.6501 | 49.1 ± 1.4 | -8.1 ± 3.0 | W | -1.1 | -2.9 | 0.92 |
| 1944.6188 | -15.9 ± 5.0 | 57.5 ± 3.6 | W | -5.6 | 3.8 | 0.41 |
| 2660.6829 | 58.2 ± 0.9 | -17.2 ± 0.8 | H | -3.3 | -1.3 | 0.61 |
| 2663.6809 | -37.7 ± 0.8 | 76.2 ± 0.8 | H | -0.5 | -3.8 | 0.26 |
| 2666.6691 | 59.0 ± 0.6 | -14.3 ± 1.1 | H | 0.6 | -1.2 | 0.90 |
| 2666.7229 | 56.0 ± 1.5 | -8.9 ± 2.8 | W | 1.1 | 0.8 | 0.91 |
| 2941.9133 | 80.7 ± 1.0 | -34.6 ± 1.1 | H | 0.6 | -0.3 | 0.79 |
| 2953.8813 | -25.6 ± 2.6 | 68.6 ± 3.7 | W | 1.1 | -1.1 | 0.35 |
| 2959.8645 | 66.4 ± 1.2 | -25.2 ± 1.9 | H | -0.5 | -6.0 | 0.63 |
| 2972.8360 | -10.5 ± 1.2 | 62.6 ± 1.5 | H | 1.6 | 7.1 | 0.40 |
| 2974.8242 | 76.9 ± 1.1 | -29.3 ± 0.9 | H | 2.3 | -0.3 | 0.83 |
| 2997.7680 | 80.0 ± 1.3 | ... [d] | H | -1.4 | ... [d] | 0.74 |
| 3014.7202 | -17.3 ± 0.9 | 65.6 ± 2.4 | H | 5.5 | -0.3 | 0.36 |
| 3015.7143 | 50.3 ± 1.6 | -10.4 ± 1.5 | H | 0.7 | -5.9 | 0.58 |
| 3367.7134 | 70.7 ± 2.7 | -10.2 ± 6.1 | W | 10.3 | 4.9 | 0.89 |
| 3367.8623 | 55.5 ± 4.7 | -8.5 ± 2.2 | W | 5.0 | -3.0 | 0.92 |

[a]Heliocentric Julian Date 2450000+

[b]H = HET HRS and W = WIYN MOS

[c]Observed minus computed radial velocity

[d]Only able to measure primary correlation peak

We accounted for this in our radial-velocity analysis by masking out the affected spectral regions.

Radial-velocity standard stars were not observed concurrently with each target observation. However, a single high-S/N observation of the M2 standard GJ 411 was obtained on 10 December 1997 by K. Rhode (Rhode et al., 2001) using the same instrument setup. Below we use this spectrum as the radial-velocity template in our cross-correlation analysis of the WIYN spectra.

#### 2.2.2.2 HET HRS

We obtained 10 high-S/N observations in queue observing mode from January 2003 to January 2004 with the High Resolution Spectrograph (HRS, Tull, 1998) on the Hobby Eberly Telescope (HET)[3]. For the purpose of cosmic-ray rejection, each observation was split into two 1,650 sec exposures with average S/N of ∼50. The HET HRS setup was chosen to have a wavelength coverage from 5,263 Å to 8,915 Å and centered at 6,948 Å with a resolution of $R \approx 30,000$ (approximately 3 pixels per resolution element). At these instrument settings, the HET HRS produces 47 orders projected onto two chips, a "red" chip with 17 orders and a "blue" chip with 30 orders. After careful examination of the resulting images from these CCDs, we found that the "red" chip suffered from fringing effects, causing the orders to be unusable. The HET HRS also allows for a sky spectrum to be taken through a separate "sky" fiber, which is then dispersed and projected in between the object orders on both chips. As with the WIYN MOS, this sky spectrum generally differs compared to the Par 1802 spectrum due to variations in the nebulosity in the ONC.

We coupled each HET HRS observation of Par 1802 with an observation of a calibration Th–Ar lamp and an observation of a bright radial-velocity standard star, HD 26162. Monitoring shifts in the spectra of this radial-velocity standard helped to increase our understanding of the instrumental drifts associated with the HET HRS.

[3]Based on observations obtained with the Hobby-Eberly Telescope, which is a joint project of the University of Texas at Austin, the Pennsylvania State University, Stanford University, Ludwig-Maximilians-Universität and Georg-August-Universität.

In a previous study (Stassun et al., 2004) we obtained single, very-high-S/N (∼250) spectra of late-type (K2V, K3V, K5V, and K7V) radial-velocity standard stars with the same HET HRS instrumental setup as the current study. We search this archive of HET HRS radial-velocity standard star spectra to find the best template in our cross-correlation analysis.

The IRAF *CCDPROC* and *ECHELLE* packages were used to process the HET HRS images, using an automated *PyRAF* [4] script that performed bias subtraction, flat-fielding, masking of bad-columns, tracing the sky and object orders, sky subtraction, and wavelength calibration. In addition, this *PyRAF* script was fine-tuned to handle the complexity found in HRS spectra, including highly angled orders on the CCD, flat-topped aperture profiles in the cross-dispersion direction, and having sky and object orders closely spaced on the CCD (on the order of a few pixels). Cosmic ray removal was performed using the IRAF *CRCOMBINE* task to co-add the two 1,650 sec exposures of Par 1802 for a given night and reject deviant pixels.

We used the IRAF *ECIDENTIFY* task to derive a Th–Ar wavelength solution for each night, using a fourth-order polynomial fit in the dispersion and cross-dispersion direction. The fit involved ∼525 Th–Ar features identified with an r.m.s. value of 0.004 Å. The very low r.m.s. value on the wavelength solution is confirms that our polynomial fit to the spectra's dispersion is a good model.

[4] *PyRAF* is a product of the Space Telescope Science Institute, which is operated by AURA for NASA.

## 2.3 Spectroscopic Analysis

### 2.3.1 Radial Velocities

We utilized the IRAF cross-correlation task *FXCOR* to obtain radial velocities from the WIYN MOS and HET HRS spectra of Par 1802. This method requires using a spectrum with a known heliocentric velocity as a reference velocity template (Tonry & Davis, 1979).

The WIYN MOS spectrum of GJ 411 (spectral type M2V) was used as the cross-correlation template for our Par 1802 WIYN MOS data. The spectra obtained during the eight nights of Par 1802 WIYN observations each produced a single cross-correlation function from which heliocentric radial velocities and their formal errors were measured using the Gaussian peak fitting tools in *FXCOR*. Previous experience with WIYN MOS indicates long-term stability of the system is better than $\sim$1 km s$^{-1}$ (Geller, A.: 2006 private communication). Using the Tonry & Davis (1979) r-statistic, which is a function of the cross-correlation peak width and its height relative to the noise in the correlation function, we derived average formal uncertainties on the radial velocities of $\sim$2 km s$^{-1}$ and $\sim$3 km s$^{-1}$ for the primary and secondary, respectively (see Table II.1).

In order to find a radial-velocity template that yields the best cross-correlation with the HET HRS observations of Par 1802, we computed and compared correlation functions from each of our archived HET HRS radial-velocity standard stars against a single Par 1802 epoch. The comparison led us to choose of HD 237903, a K7V

standard star, as it produced the strongest correlation peaks. To explore the possibility of Par 1802 having a later spectral type, observations and analysis of a complete set of M spectral-type templates with HET HRS were obtained; however, a full radial velocity analysis employing these spectra has yet to be completed.

We cross-correlated the 30 spectral orders in each Par 1802 spectrum producing 30 separate output cross-correlation functions. The cross-correlation functions were then summed for each Par 1802 epoch. By co-adding the individual order's functions the overall strength of the correlation peaks was increased, and random correlations in the spectra were minimized. We obtained a radial velocity at each epoch by measuring the centroid of a Gaussian fit to the peaks in these combined cross-correlation functions. These radial velocities are consistent, albeit with higher precision, with the velocities obtained by averaging the results from each order. We derived uncertainties in these velocities using the statistical error in the centroid position of the Gaussian least-squares fit. We found that in some orders, large and broad spectral features, such as H$\alpha$, Na II doublet, and large nebular emission lines, dominated the correlation function; consequently these orders did not produce accurate centroids for radial-velocity measurement. By masking out these lines during the cross-correlation process, we were able to maximize the number of correlation functions for summation. In addition, we rejected some orders due to not clearly showing both the primary and secondary correlation peaks because of other low-level structure in the correlation function. In the end, we were left with between 5 and 15 quality orders used to derive

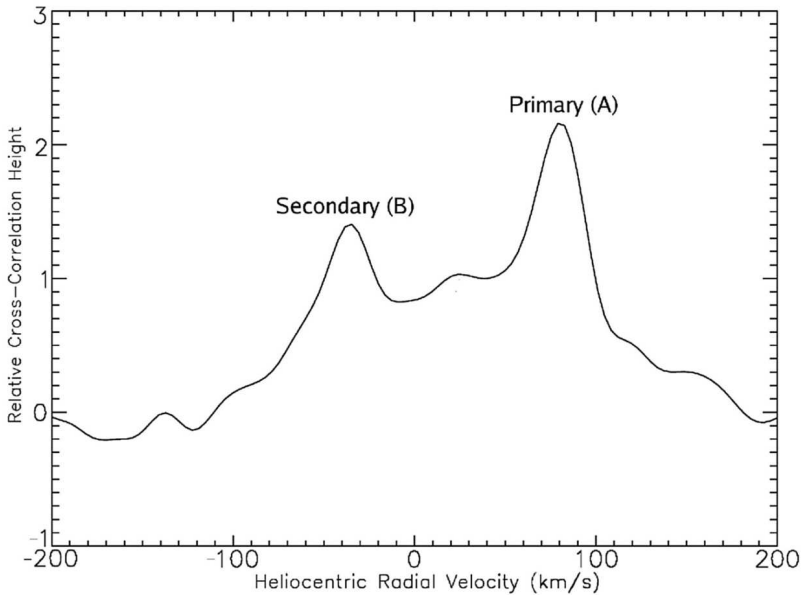


Figure 2.2: Fourier cross-correlation function derived from the HET HRS spectrum observed at HJD=2452941 (orbital phase of 0.79). The function clearly shows a double peak nature with a height ratio of ∼1.5.

a significantly improved single combined correlation function for each HET HRS epoch of Par 1802.

Our cross-correlation functions of Par 1802 show two distinct peaks (see Fig. 2.2) with a height ratio of ∼1.5. By convention, we designated the component with the stronger correlation peak as the primary (A) and the weaker peak as the secondary (B). By chance, a few epochs of Par 1802 spectra were taken near eclipse, resulting in a cross-correlation function with blended correlation peaks. Finding centroids of individual Gaussian functions that make up blended correlation functions is subject to many sources of uncertainty (Latham et al., 1996). Therefore, radial velocities within 5% phase near either eclipse were not included in our modeling of the Par 1802 orbit. The remaining velocities have mean formal measurement uncertainties of ∼2 km $s^{-1}$.

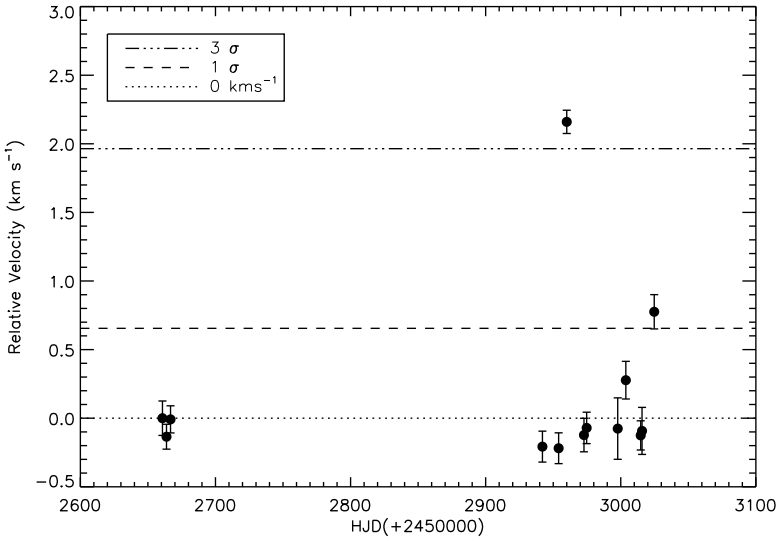


Figure 2.3: Residuals and confidence levels (dashed lines) for the radial velocity standard star, HD 26162, taken with the HET HRS on the same nights we obtained data on Par 1802. The velocities have a $\sigma = 0.65$ km s$^{-1}$ when all points are included, and a $\sigma = 0.28$ km s$^{-1}$ when the outlying (above 3-$\sigma$) datum is excluded.

To investigate any possible systematics in the radial velocities derived from the HET HRS spectra, we reduced the observations of the radial-velocity standard star HD 26162 in the same manner as the Par 1802 data. Fig. 2.3 shows the results for this monitoring of HD 26162. The overall velocity deviations show that the HET HRS system is quite stable. Nevertheless, there was a radial velocity measurement (2.2±0.1 km s$^{-1}$ at HJD=2452959) obtained that deviated significantly from the mean (3.3$\sigma$). We subtracted this epoch's instrumental shift from the Par 1802 radial velocities obtained on the same night. Except for this one outlier, the HD 26162 data reveal a high level of stability (0.28 km s$^{-1}$ r.m.s.) of the HRS over the 364-day time span of the HET observations and thus we opted to not subtract any offset from any other

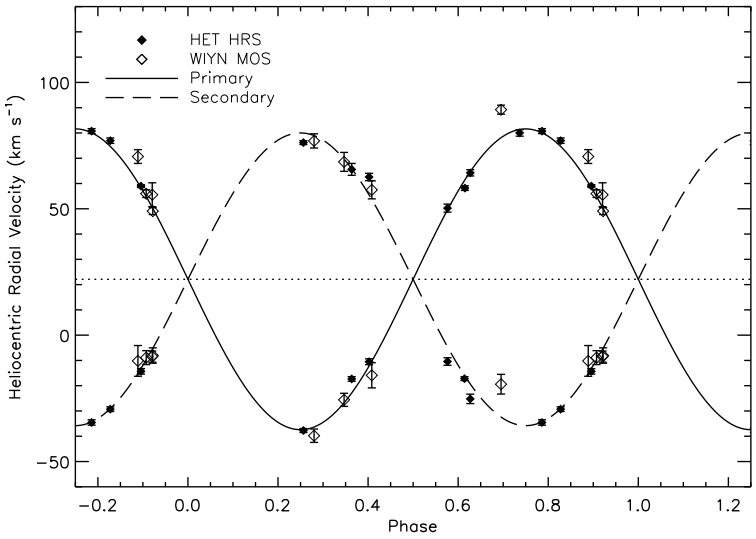


Figure 2.4: Radial velocity orbital solution where the orbital period is held constant at the value determined by the photometric light-curve, $P = 4.673845$ days. Phasing is set such that the zero point corresponds to time of primary eclipse minimum and is folded on the above period. The velocity curves show the orbital fit for the primary (solid line) and secondary (dashed line) of Par 1802. The dotted line marks the systemic radial velocity (23.5 km s$^{-1}$). Heliocentric radial velocity measurements are from HET HRS (filled symbols) and WIYN MOS (open symbols). We model a total of 18 epochs of observations, 10 HET HRS and 8 WIYN MOS, in this orbit solution.

Par 1802 epoch.

In Table II.1, we list in columns 1–4 the Julian dates, the primary and secondary radial velocities with their respective uncertainties, and the telescope used. Also listed in columns 5–7 are the residuals of these radial velocities relative to the best-fit orbit solution (Fig. 2.4), and the corresponding orbital phase. We note that the residuals to the orbit solution are large compared to the uncertainties in the radial velocity measurements; the source of these large offsets is not currently understood.

### 2.3.2 Orion Nebula Cluster Membership

In order to investigate the age of Par 1802, we inspect the system's spectra (see Section 2.2.2.2) for pre-main-sequence signatures. We measure the $\lambda$6,708 Å lithium line equivalent widths for the individual components of Par 1802 from a continuum-normalized, high-resolution HET HRS spectrum (HJD=2,452,664), where the two components were significantly Doppler-shifted (114 km s$^{-1}$) relative to each other. We measured equivalent widths (EW) of the two Li features, using the spectral-line deblending function in the IRAF task *SPLOT*, to be EW$_A \approx$ 210 mÅ and EW$_B \approx$ 110 mÅ. Correcting for the difference in continuum fluxes between the two stars (based on the relative strengths of their cross-correlation peaks; see Section 2.3.1), we get EW$_A \approx$ 330 mÅ and EW$_B \approx$ 300 mÅ. Li EW values like these are an intrinsic characteristic of PMS stars in the Orion star-forming region (e.g. Dolan & Mathieu (1999) observe Li EWs above 250 mÅ for low-mass ONC stars).

Additionally, in the HJD=2,452,664 HET HRS spectrum we measure the H$\alpha$ lines of each component apart from the large nebular emission line (see Fig. 2.3). Again using the IRAF task *SPLOT*, we find each component only displays a few hundred mÅ of H$\alpha$ emission. Classical T Tauri stars in the Orion star-forming region are found to have H$\alpha$ EWs >10 Å (Herbig & Bell, 1988; Strom et al., 1989). Therefore, coupled with the small total amount of photometric variability (see Section 2.2.1), Par 1802's components do not appear to be actively accreting material from a circumstellar disk and are thus classified as weak-lined T Tauri stars.

Furthermore, our derived center-of-mass velocity for Par 1802 of $\gamma$ =23.7±0.5 km $s^{-1}$ (see Section 2.4) is comparable to the currently accepted ONC systemic cluster velocity of 25±2 km $s^{-1}$ (Sicilia-Aguilar et al., 2005). Our kinematic membership determination is in agreement with the 98% proper motion ONC membership probablity calculation of Jones & Walker (1988).

Finally, based on a 480±80 parsec distance to $\theta^1$ Ori C (Genzel & Stutzki, 1989), the designated center of the ONC, the projected separation of Par 1802 from the cluster center is 1.8 parsecs. This places Par 1802 within 8 core radii from the ONC center (Hillenbrand & Hartmann, 1998). In fact, combining the luminosities and fluxes for each component of Par 1802 from our combined light-curve and radial-velocity orbit solution (see Section 2.4) we calculate a distance of 420±15 pc for this binary system. This distance is in very good agreement with the assumed distance to the ONC.

All of the preceding characteristics of Par 1802, plus the apparent agreement between the large component radii for Par 1802 A & B and the sizes predicted by PMS models (see Section 2.5), suggest that Par 1802 is a young PMS system in the Orion star-forming region and most likely a member of the ONC (age of 1±1 Myr, Hillenbrand, 1997).

## 2.4 Characterizing Par 1802 A & B

In this section, we describe the modeling of Par 1802's radial velocities and light curves, including our calculated physical properties of the system's two components.

To calculate the orbital properties and physical parameters of Par 1802, we preformed simultaneous modeling of the radial velocity and light curve data using the eclipsing binary software *PHOEBE* (Prša & Zwitter, 2005). This package uses an optimized Wilson & Devinney code to solve the fundamental parameters of the binary orbit solution: orbit period, P; time of periastron passage, $T_P$; eccentricity, $e$; angle from the node to periastron, $\omega$; semimajor axis, $a$; center-of-mass velocity, $\gamma$; ratio of secondary to primary mass, q; total mass, $M_{tot} = M_A + M_B$; inclination, $i$; primary mass, $M_A$; secondary mass, $M_B$; sum of component radii, $R_A + R_B$; and ratio of surface temperatures, $T_A/T_B$. The actual modeling was performed in an iteratively to derive realistic initial guesses and to constrain the solution of the many parameters in the code. In the final fit, we allowed all of the component and orbit parameters to be free variables. In Table II.2, we report our best-fit solution for the radial velocities and $I_c$-band light-curve. We find that Par 1802 is composed of twin $0.41 \pm 0.01$ $M_\odot$ PMS stars in a very nearly circular orbit. This makes Par 1802 the first confirmed PMS, low-mass *identical twin* system.

We would like to point out that the eclipsing nature of Par 1802 allows us to remove ambiguity in the derived masses, because we know the inclination angle ($i$) of the system; in addition, we can calculate the sum of the radii and the temperature

Table II.2. Orbital and Physical Parameters of Par 1802 A & B

| Parameter[a] | Value |
|---|---|
| P [days] | 4.673843±0.000068 |
| $T_p$ [yr] | 2003.834996±0.000055 |
| $e$ | 0.029±0.005 |
| $\omega$ [deg] | 266.1±1.8 |
| $a\sin(i)$ [AU] | 0.0501±0.0006 |
| $\gamma$ [km $s^{-1}$] | 23.7±0.5 |
| q | 0.98±0.01 |
| $M_{tot}\sin^3(i)$ [$M_\odot$] | 0.768±0.028 |
| $i$ [deg] | 78.1±0.6 |
| $M_A$ [$M_\odot$] | 0.414±0.015 |
| $M_B$ [$M_\odot$] | 0.406±0.014 |
| $R_A$+$R_B$ [$R_\odot$] | 3.51±0.05 |
| $T_A/T_B$ | 1.084±0.007 |

[a]See text for full description of parameters

ratios of the binary components. This is not possible for other spectroscopic binaries, and illustrates the power of eclipising systems for determining absolute fundamental stellar parameters.

Supplementary analysis of Par 1802 allows us to derive additional properties for the components of this system. Using archived broadband flux measurements from 0.35 $\mu$m to 8 $\mu$m (Stassun et al., 2008), we find that Par 1802's spectral energy distribution is best fit by a single-temperature model stellar atmosphere of T=3800 K, with a systematic uncertainty of ∼100 K. Combining this with the temperature ratio found from our orbit/light-curve solution, we measure component temperatures of $T_A = 3945\pm15$ K and $T_B = 3655\pm15$ K. Although these temperatures have measured errors of only 15 K, we note they also have a systematic, correlated uncertainty of ∼100 K.

In addition, the individual radii of Par 1802 A & B can be estimated from the flux ratio of the two stars. We use two different techniques to calculate the flux ratio: two-dimensional cross-correlation (TODCOR) and tomographic reconstruction. First, TODCOR (Zucker & Mazeh, 1994) uses a grid of spectral templates to determine what combination of stellar spectra produces the highest cross-correlation peak (i.e., the best match). We applied this technique to an HET spectrum where the two components are at maximal radial velocity separation. Using a grid of templates ranging from K2 to M2, we find that Par 1802's spectrum is matched best by a combination of K7 and M2 spectral types, thus suggesting a flux ratio to be $F_B/F_A = 0.61 \pm 0.10$, where the error is estimated from the dispersion in the multiple HET orders used. Second, the tomographic reconstruction technique (Bagnuolo & Gies, 1991) uses a gradient-search algorithm to determine the primary and secondary spectra that, when recombined, minimize the $\chi^2$ of the residuals with respect to the observed spectra. Using multiple spectra with known orbital parameters provides enough information to successfully reconstruct the component spectra, with the only free parameter being the continuum levels of the two stars. By finding the continuum ratio that best reproduces the observed spectra, we can directly determine the best-fit flux ratio of the two components. We again use our high-resolution HET spectra at three different, but well separated orbit phases, but when the component spectra are still well seperated, and use spectral templates of M1V for the primary and M3V for the secondary. We find from our analysis that a flux ratio of $F_B/F_A = 0.50 \pm 0.07$ best

reconstructs Par 1802's spectrum around a wavelength of 0.6 $\mu$m. The uncertainty in the ratio is estimated from the scatter in orders used from the HET spectra. This flux ratio is compatible, within the known uncertainty, to the ratio determined using the TODCOR method.

We adopt the mean flux ratio of the two techniques outlined above, i.e., $F_B/F_A = 0.55 \pm 0.06$, where the error is the uncertainty on the mean. This, in combination with the temperature ratio from our light curve solution and bolometric corrections for 0.6 $\mu$m, implies a radius ratio of $R_A/R_B = 1.08 \pm 0.05$. Using the sum of the component radii, as determined by the observed eclipse durations and orbital velocities, we find individual radii of Par 1802 A & B to be 1.82$\pm$0.05 $R_\odot$ and 1.69$\pm$0.05 $R_\odot$, respectively. Lastly, the ratio and individual luminosities for Par 1802 A & B can be determined using the Stefan-Boltzmann law. We find the ratio of luminosities to be $L_A/L_B = 1.58 \pm 0.10$, or $L_A = 0.72$ $L_\odot$ and $L_B = 0.46$ $L_\odot$.

## 2.5 Comparison to Pre-Main-Sequence Models

During its PMS evolution, the physical characteristics (temperature, radius, and luminosity) of a star are governed by the balance between gravitational collapse and internal pressure (Hayashi, 1961). As young stars emit thermal radiation, their internal pressure decreases, and subsequently they contract under the force of gravity. This process, identified as the Hayashi track on the Hertzsprung-Russell (H-R) diagram (Hayashi, 1961), is typically assumed to be determined by two parameters: mass and

chemical composition. Therefore, we expect that the properties of two equal-mass stars born at the same time out of the same material should follow very similar, if not identical, evolutionary paths.

The predicted temperatures, radii, and luminosities of PMS stars are highly dependent on the choice of PMS stellar evolution model (see Fig. 2.5). More specifically, the D'Antona & Mazzitelli (1997, DAM97) models predict a significant decrease in surface temperature at an age $\sim$1 Myr; Palla & Stahler (1999, PS99) and Siess et al. (2000, SDF00) suggest that surface temperatures stay roughly constant ($\pm$50 K); and Baraffe et al. (1998, BCAH98) predicts a warming trend at the earliest stellar ages.

The *identical twins*, Par 1802 A & B, provide a unique opportunity to test the accuracy of these models. We find that the two components have surprising differences in their surface temperatures of $\sim$300 K ($\sim$10%), in their radii of $\sim$0.1 $R_{\odot}$ ($\sim$5%), and in their luminosities of a factor of 2. Furthermore, when we compare the properties of Par 1802 A & B to current PMS models (see Fig. 2.5), we see that DAM97 is the only model that is able to replicate the surface temperatures of both components, due the predicted high initial temperatures in the model, and a rapid decrease in the temperatures of the low-mass star at $\sim$1 Myr. The DAM97 model suggests that the observed temperature, radius, and luminosity offsets indicate that the larger, warmer, more luminous Par 1802 A component is at an earlier evolution stage than Par 1802 B, with an age difference of $\sim$300,000 yr.

We suggest two possible explanations for the observed agreement/disagreement

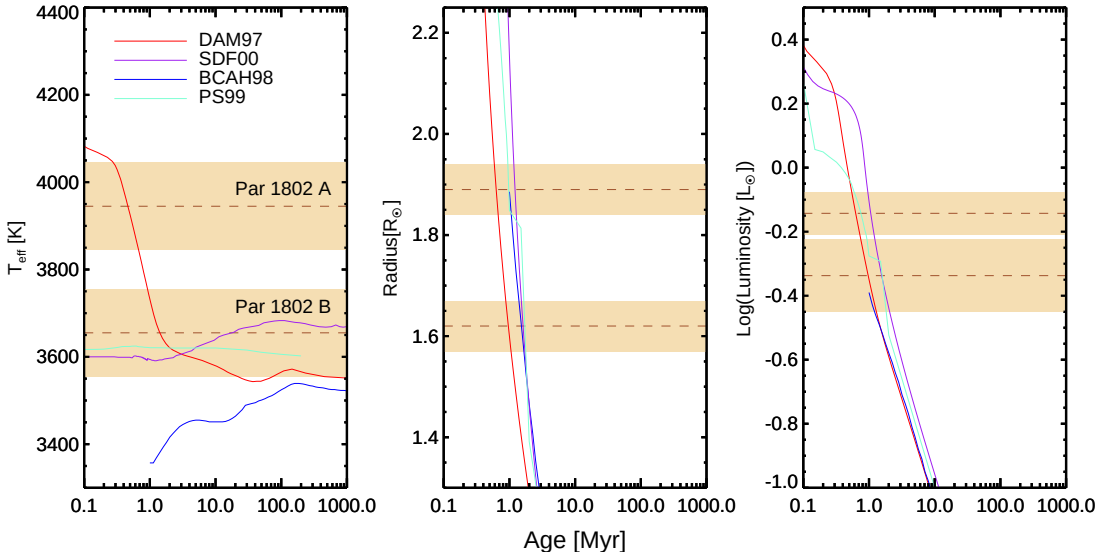


Figure 2.5: Comparison of physical properties of Par 1802 with theoretical models. In each panel, the solid lines show the evolution of a 0.4 $M_\odot$ star as predicted by various PMS models (see legend in left panel and text for references). Also plotted are the measured properties of Par 1802 A & B as determined from our combined radial-velocity and light-curve orbit solution. The shaded regions represent the combined measurement and systematic uncertainties on the determined individual parameters. Note that the uncertainties in the temperatures, radii and luminosities are not independent between the two stars, because they are connected by precisely determined ratios; thus, for example, the primary star cannot be forced cooler while simultaneously forcing the secondary warmer.

between the PMS models and Par 1802: *(a)* the temperature of Par 1802 B is in agreement, within 1–2 $\sigma$, of the majority of the PMS models, therefore, perhaps there is something different about Par 1802 A that causes it to have an abnormally high temperature and radius; or *(b)* DAM97 alone correctly predicts an apparent difference in the star formation history of Par 1802 A & B on the order of ∼300,000 yr. We have not found any significant other differences in the properties of Par 1802 A, such as our measurements from the HET HRS spectra of rotation rate, H$\alpha$ emission (an indicator of magnetic activity), Li absorption (a probe of internal structure), when compared

to its companion. If case *(a)* is correct, one would have to address the question of why two coeval, equal-mass stars showing such similar properties would have significantly different temperatures and radii. The difficulty in answering this question suggests that case *(b)* is more likely correct, that the age synchronization of binary systems might have an astrophysical precision limit of several hundred thousand years, as suggested by the DAM97 evolution tracks.

# Chapter III

## PHOTOMETRIC SEQUENCES OF GALACTIC OPEN CLUSTERS

(Published as: Cargile & James 2010 *submitted* ; James et al. *in prep.*)

Open clusters, being natural samples of coeval, equidistant, and chemically homogeneous stars, have long been considered powerful laboratories to test the models of stellar formation and evolution in our Galaxy. Through studying open clusters at several different ages, we are able to gain insight into the complex, inter-dependent roles of age, composition, mass, and initial conditions play in determining the observed properties of stars.

The classic approach to determining fundamental properties, ages and distances, of open clusters, as well as the properties of individual stars, luminosities and effective temperatures, is finding a best-fitting isochrone for the apparent cluster sequence in a Hertzsprung-Russell (H-R) diagram. This is typically performed on a cluster's color-magnitude diagram (CMD), an empirical H-R diagram on which a star's apparent magnitude and color are proxies for luminosity and effective temperature, respectively (Sandage, 1958; Mermilliod, 1981a,b; Meynet et al., 1993). In principle, this technique can yield results solely using broadband photometry; however, in practice this method can be hampered by uncertainties in the photometric systems, as well as by intrinsic limitations due to the properties of the stars themselves (*e.g.,* degeneracy of blue colors

of low-mass stars, binarity, star-spots, *etc.*). Furthermore, this technique suffers from being heavily dependent on the input physics used by the stellar evolution models. For instance, one can show for the same cluster that different nuclear *turn-off* and pre-main-sequence (PMS) models can give stellar ages that differ by a factor of 1.5-2 (Chiosi et al., 1992; Meynet et al., 1993; Meynet & Maeder, 1997, 2000; Baraffe et al., 1998, 2002; Siess et al., 2000; Naylor, 2009).

In this chapter, we report the results of our campaign to determine the properties of two open clusters, IC 4665 and Blanco 1, employing a new photometric survey of open clusters using the SMARTS telescopes at CTIO. We detail our observations, photometric reduction and analysis, and outline our isochrone analysis of these clusters' CMDs using a recently developed statistical tool, $\tau^2$ modeling. Our results for IC 4665 have been submitted for publication in the *Astronomical Journal*, and we are publishing the finding of our Blanco 1 photometric survey later this year.

## 3.1 SMARTS Photometric Open Cluster Survey (SPOCS)

The majority of the standardized photometry included in this chapter and, in fact, in this thesis, stems from the SMARTS Photometric Open Cluster Survey (SPOCS)[1]. This project is a dedicated effort to observe southern open clusters that lack or have unreliable photometry, and to ultimately provide high-fidelity standardized colors and magnitudes for these clusters' members. Over a span of ∼3 years beginning in 2005 we

[1] SPOCS data are publicly available at http://people.vanderbilt.edu/ p.cargile/SPOCS/SPOCS.html

have observed ∼10 clusters in the SPOCS survey using the SMARTS 1.0 m telescope at the Cerro Tololo Interamerican Observatory (CTIO). The data were acquired with the quad-amplifier Y4KCam CCD camera. With its 15 $\mu$m pixels and 0.289 arcsec/pixel plate scale, the Y4KCam has an on-sky field of view per CCD field of $19\farcm3 \times 19\farcm3$. Since open clusters are extended objects that at times suffer from image crowding, this large field of view and high resolution made the Y4KCam perfectly suited for the SPOCS survey. We observed each cluster with a combination of the Johnson-Cousins $UBVI_c$ filters (for a summary of this filter system, see Landolt, 1983). Also included in each night of our observing runs were observations of Landolt standard star fields at various air masses, which we use to define our photometric equations (see below).

We processed our SPOCS images using standard *IRAF* software, primarily tasks found in the *IMRED* and *DOAPHOT* photometric data reduction libraries in the *NOAO* package. As typically done with CCD imaging, our first step in our reduction procedure is the removal of the instrument signature. We subtract the readout bias and the CCD response function using the general reduction task *CCDPROC*. We then use *DAOFIND* to identify the point sources in the images. This task identifies count density enhancements in the image that are best described by the instrument's point-spread-function (PSF) for a point source, thus identifying stellar-like objects and rejecting extended objects, such as galaxies. It uses a 2-D Gaussian to calculate X and Y coordinates for the centroid of the identified sources. When image crowding is not an issue (which is the case for the open clusters studied in this chapter), we use the aperture

photometry task *PHOT* to determine the instrumental $\mathrm{UBVI_c}$ photometry for each source identified by *DAOFIND*. This task calculates magnitudes by summing the pixel values within a circular annulus, or aperture, centered at the X and Y coordinates specified by *DAOFIND*.

In order to standardize the instrumental SPOCS $\mathrm{UBVI_c}$ photometry, we calculated nightly extinction coefficients, color transformation coefficients, and zero-points for our photometry. The standardization equations are listed in (3.1a), (3.1b), and (3.1c), showing the relationship between instrumental, $u, b, v, i_c$, and standardized, $\mathrm{UBVI_c}$ , magnitudes and colors:

$$V = v + \epsilon\ (B - V) + \xi_v - \kappa_v\ X \tag{3.1a}$$
$$(B - V) = \mu\ (b - v) + \xi_{bv} - \mu\ \kappa_{bv}\ X \tag{3.1b}$$
$$(V - I_c) = \psi\ (v - i_c) + \xi_{vi} - \psi\ \kappa_{vi}\ X \tag{3.1c}$$
$$(U - B) = \phi\ (u - b) + \xi_{ub} - \phi\ \kappa_{ub}\ X \tag{3.1d}$$

Here, we define the equation's coefficients:

$\kappa_v$, $\kappa_{bv}$, $\kappa_{vi}$, and $\kappa_{ub}$ are filter-dependent extinction coefficients

$\epsilon$, $\mu$, $\psi$, and $\phi$ are color-transformation coefficients

$\xi_v$, $\xi_{bv}$, $\xi_{vi}$, and $\xi_{ub}$ are zero-point coefficients

and $X$ is defined as the airmass of the stars ($X = \sec(z)$ — where $z$ is the zenith distance).

We derive the unknown coefficients by simultaneously solving this self-similar set of equations using a least-squares fit algorithm. Comparing measured instrumental

magnitudes and colors of Landolt standard stars to their precisely determined published values (Landolt, 1992, 2009) allows an iterative rejection process to take place, thereby eliminating seriously discrepant standard star measurements. More specifically, by substituting the instrumental magnitudes and derived coefficients back into (3.1a), (3.1b), (3.1c), and (3.1d), we are able to calculate standardized photometric magnitudes and colors for each Landolt star. Comparison of these derived values and the star's published photometry yields residual errors in our color-equations. Any inconsistent photometric values are probably caused by an imperfect CCD frame, cosmic ray contamination, or even photometric variability in a standard star. Therefore, if these discordant standard stars show residual offsets larger than $\sim$2.5 times the standard deviation, they were rejected from the calibrations and the color-equation coefficients were recalculated. This is repeated until the solution of the color-equations does not include any significantly discrepant photometric values (r.m.s. values of $\sim$0.01 mag). Typically, out of approximately 80 standard stars observed in each filter each night, a minimum of 60 stars were retained to constrain the color equations.

In order to investigate the stability of our SPOCS photometric system, we typically observe a control field where we do a repeat observation of the same set of stars on different nights. The relative comparison of the photometry in these control fields allows us to estimate our internal error. Normally, we find that our photometric measurements are typically consistent between control fields at the $\sim$1-4% level for our V and $I_c$ photometry brighter than 16 magnitude. For these same objects, the

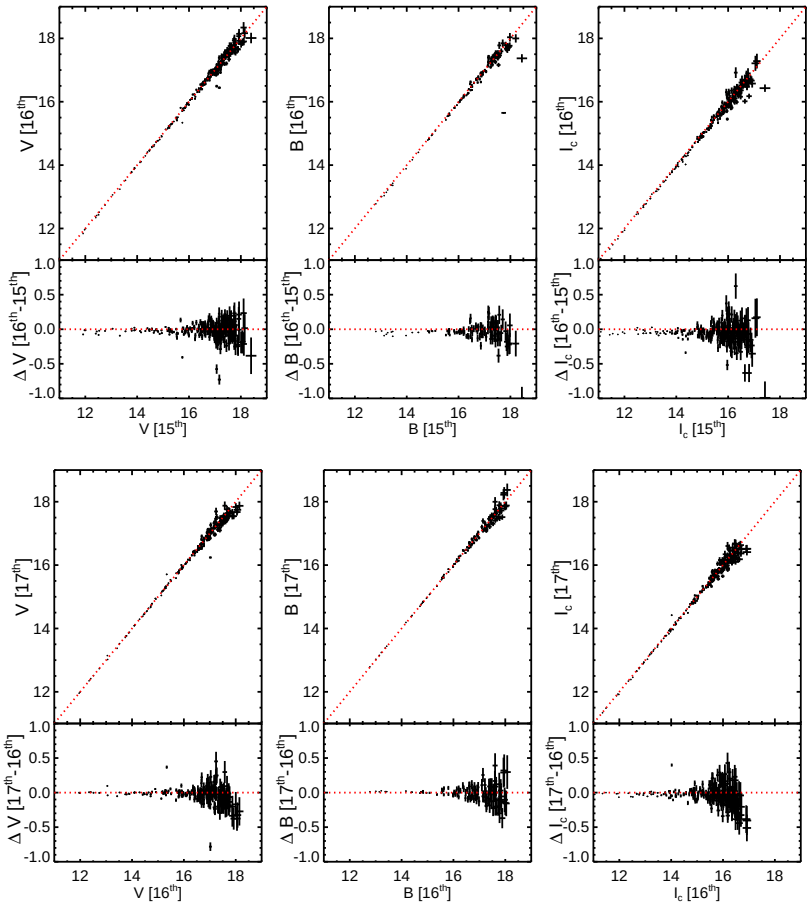


Figure 3.1: Comparison of CTIO BVI$_c$ photometry for control fields in IC 4665, based on observing nights 15, 16, and 17 Sept. 2005. Upper panels show direct comparison, while their residuals are plotted in each lower one. Data are plotted with their associated photometric error. Red dotted lines are loci of equality and not fits to the data.

B-band observations do however show an offset at the ∼5-6% level. Naturally, for the dimmer objects (V, B, I$_c$ > 16 magnitudes), with decreasing S/N levels, diminished precisions of order ∼9-10% are seen. An example control field comparison for SPOCS photometry of IC 4665 is displayed in Fig. 3.1.

The astrometric solutions for our SPOCS datasets were computed using two different techniques. First, we produce an astrometric solution for our images using a

6th-order polynomial fit to X,Y CCD coordinates and accurate coordinates for reference stars in the SuperCOSMOS catalog (Hambly et al., 2001). The 6th-order polynomial accounts for six different types of possible image distortions: horizontal offset, vertical offset, rotation, horizontal skew, vertical skew, and pincushion. More recently, we have used the automated "astrometric engine" produced by *Astrometry.net*[2] (Lang et al., 2009). Briefly, the Astrometry.net software takes as input an astronomical image (or X,Y positions from an image) and returns as output the astrometric solution (pointing, scale, and orientation) for that image. It does this by identifying sets of four or five stars in a quadrilateral shape, then comparing this to a catalog of indices built from the USNO-B database. So far, we have had a 100% recovery rate for our SPOCS images, with most astrometric solutions being found within 1 minute using a typical desktop CPU.

To judge which of the two techniques produces the most accurate astrometry, we compared the 2MASS positions (astrometric accuracy of $\sim 0\farcs1$; Skrutskie et al. 2006) for our SPOCS IC 4665 dataset (see Section 3.3) to the positions derived using the 6th-order polynomial fit and the *Astrometry.net* software. In Fig. 3.2, we have plotted the resulting positional offset histograms. We see that the *Astrometry.net* software produces positions (centroid at $\sim$0.2 arcseconds) that agree by a factor of $\sim$2 better with 2MASS astrometry compared to the 6th-order polynomial fit (centroid at $\sim$0.35 arcseconds). This suggests that the Y4KCam CCD contains high-order image distortions that

[2] *Astrometry.net* astrometric solver is available in a *beta*-version online at http://astrometry.net.

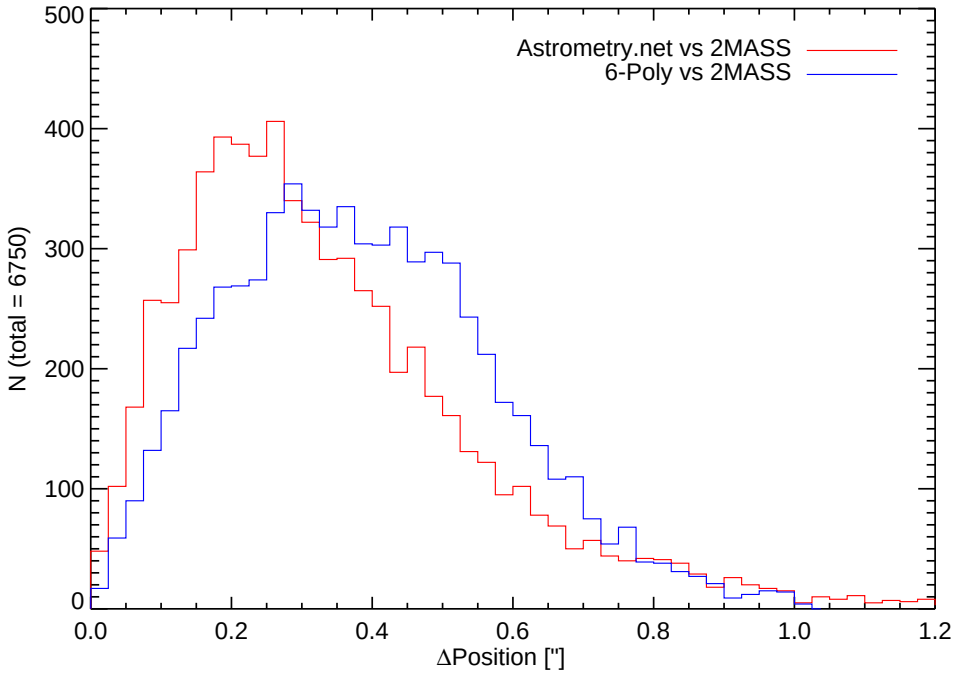


Figure 3.2: Distribution of positional offset between objects in the SPOCS IC 4665 survey and their 2MASS IR counterparts. Red line is the distribution for object's positions determined using *Astrometry.net* software, and blue line is for positional offsets for object coordinates derived using a 6th-order polynomial fit.

are not taken into account using the 6th-order polynomial technique. We therefore preferentially use the astrometric coordinates from *Astrometry.net* when available.

## 3.2 $\tau^2$ Color-Magnitude Isochrone Modeling

Typically, finding a best-fit isochrone for a cluster is performed using a "by-eye" comparison of the predicted properties from stellar evolution models and a cluster's CMD. This technique can be burdened by uncertainties due to field-star contamination and/or photometric error, as well as an apparent spread in the cluster sequence due to binarity. In addition, the use of this technique does not allow for formal calcu-

lations of correlated uncertainties in derived ages and distances. In order to address some of these issues hampering this technique, the Tau-squared ($\tau^2$) maximum likelihood statistic has recently been developed for modeling CMDs with two-dimensional theoretical isochrones (Naylor & Jeffries, 2006; Naylor, 2009). Examples of its application can be found in Jeffries et al. (2007); Joshi et al. (2008); Mayne & Naylor (2008); Jeffries et al. (2009b). In short, $\tau^2$ is a generalized $\chi^2$ statistic that takes into account correlated uncertainties in two dimensions. Thus, we can use this statistical tool to effectively constrain a two-dimensional distribution by minimizing $\tau^2$; in this case we find a best-fit CMD age- and distance-dependent isochrone.

Following closely the technique described in Naylor & Jeffries (2006) and Naylor (2009), we first produce a grid of stellar-model isochrones spanning a range of ages and distances. For modeling lower-mass stars, we use the solar-metallicity stellar evolution models from D'Antona & Mazzitelli (1997), Baraffe et al. (1998), and Siess et al. (2000), and employ a *Pleiades tuning* method to translate model luminosities and effective temperatures ($T_{eff}$) into magnitudes and colors (for a full description of the *Pleiades tuning* method, see Jeffries et al., 2001; Naylor et al., 2002). For higher-mass stars, we use upper-main-sequence models from Lejeune & Schaerer (2001) and Girardi et al. (2002), coupled with solar-metallicity bolometric corrections and effective temperature to color conversions, and color dependent reddening vectors from Bessell et al. (1998)

The $\tau^2$ software[3] uses Monte Carlo methods to produce a probability, based on $\tau^2$, of finding a star drawn from the full photometric catalog (including photometric binaries) represented by each age-distance pixel on the grid. These probabilities are calculated for all stars in the CMD, and summed to derive the overall $\tau^2$ for the given age and distance isochrone. By repeating this process for a range of ages and distances, a $\tau^2$ grid is produced, and the minimum value is the best-fit isochrone for the modeled CMD. To ensure that our best-fit isochrones are not influenced by obvious outliers, we added an additional *soft-clipping* rejection step (Naylor & Jeffries, 2006), where points having colors/magnitudes lying significantly away ($\tau^2$ probability $< \exp -0.5 \times 20$ as recommended by Naylor & Jeffries) from the range of model isochrones are *ab initio* removed from the modeling process. Specifically, we apply an initial *soft-clipping* step for those data points having derived $\tau^2$ values 20 above the minimium $\tau^2$.

Once a best-fit isochrone for a CMD is found, we derive its probability based on the minimum $\tau^2$ values. In many cases, we include an additional magnitude-independent systematic uncertainty to the colors and magnitudes in our CMDs to increase their probabilities to an acceptable value (*i.e.,* $\gtrsim 30\%$). This is analogous to the traditional method of increasing error bars to arrive at a $\chi^2_\nu \sim 1$, and ensures that the uncertainties on our ages and distances are appropriate relative to the scatter observed in our CMDs. Typically, we found that an additional $\sim 0.01 - 0.03$ increase is required for

[3] $\tau^2$ software is publicly distributed at http://www.astro.ex.ac.uk/people/timn/tau-squared.

our V, B, and $I_c$ magnitudes to achieve sufficiently high best-fit probabilities. This magnitude of systematic uncertainty can be easily explained by systematics in the standardization procedure (Naylor et al., 2002) or natural variability in such young, solar-type stars (*e.g.,* spotted stars in IC 4665 have reported optical variability amplitudes of $\sim 0.03 - 0.1$ mag, Allain et al., 1996).

### 3.3 Pre-Main-Sequence Cluster: IC4665

IC 4665 is a relatively young (< 100 Myr), nearby (∼350 pc) open cluster in the constellation Ophiuchus (R.A.(2000): $17^h46^m$, Dec.(2000):$+05°43'$). The cluster is at a high Galactic latitude ($b = +17°$), and has a reddening of $E(B-V) = 0.174$ (WEBDA Open Cluster Database[4]). The youth and close proximity of this cluster has made it a popular target for studying young stars, while the majority of its low-mass members are still in the PMS phase.

Determining a precise and accurate age for IC 4665 is fundamental to its use as a constraint for theoretical models describing early stellar evolution. Its age, however, continues to be a matter of uncertainty. Ages for IC 4665 found in the literature range from 28 to greater than 100 Myr (Mermilliod, 1981b; Prosser, 1993; Prosser & Giampapa, 1994; Giampapa et al., 1998), although one of the age determinations is derived using the lithium depletion boundary method (Manzi et al., 2008), which so far has only been applied to a small handful of open clusters. With such a large

[4]The WEBDA database, developed by J.-C. Mermilliod, can be found at http://www.univie.ac.at/webda/

range of possible ages cited for IC 4665, its applicability for constraining theoretical stellar evolution models remains suspect. Here, we use SPOCS photometric data for cluster members of IC 4665 to take a new look at its discrepant age determinations to verify whether there exists a true, observational-dependent age spread in IC 4665, or whether this spread in ages is due to uncertainty in the extant studies of the cluster.

### 3.3.1 Extant Observations of IC 4665

Previously, the most extensive optical survey of IC 4665 was performed by Prosser (1993, hereafter P93), which combined astrometric, photometric, and spectroscopic programs to identify members of the cluster. P93 acquired BVRI$_k$ CCD photometry for 4100 stars down to a limiting magnitude of $V \sim 18.5$. Proper motions were measured from archival photographic plates, and membership probabilities were derived for stars brighter than V$\simeq$14.5. Their analysis found 173 stars with non-zero proper motion membership probability, of which 22 were identified as previously known cluster members, 57 were classified as photometric candidates (*i.e.,* stars lying near a 36 Myr isochrone), 72 were photometric nonmembers, and 22 stars had undecided membership. They also obtained low-dispersion spectra for 41 faint candidate stars, of which 25 showed definite H$\alpha$ emission, while 5 showed possible weak H$\alpha$ emission. P93 include these 30 stars as probable members of IC 4665.

IC 4665 is currently one of just five open clusters with a published detection of a lithium depletion boundary (hereafter LDB). Manzi et al. (2008) measured an age

of $28 \pm 5$ Myr for the cluster based on the absolute magnitude of stars found at the LDB. Moreover, the global lithium abundance distribution in IC 4665 stars was first studied by Martin & Montes (1997), where they measure the Li abundance of 14 early-G through early-M spectral type stars. Interestingly, they found that the Li distribution of IC 4665 is similar to the older Pleiades open cluster ($\sim$125 Myr), although they had a limited sample size of measured Li abundances. More recently, Jeffries et al. (2009a) determined the Li abundance of 20 late-F to early-M spectral type stars, and confirmed that the Li distribution of IC 4665 appears more like the Pleiades than other younger open clusters.

The stellar rotation distribution of IC 4665 is commonly used to empirically constrain theories of early angular momentum evolution (e.g. Barnes, 2003, 2007). Using rotation period measurements for nine solar-type stars (F9 to K0 spectral type), Allain et al. (1996) found a dearth of slow rotators (periods $\geq 4$ days) in IC 4665, indicative of a young cluster where the stars have not had time to spin down. However, Jeffries et al. (2009a) measure projected rotation velocity ($\mathrm{Vsin}\, i$) for IC 4665 cluster members, and find that there is a lack of fast rotators ($\mathrm{Vsin}\, i > 20$ km s$^{-1}$) with $1 < (V - I_c) < 2$ ($\sim$ K-type stars). Comparing this $\mathrm{Vsin}\, i$ distribution to the older IC 2391, IC 2602, and Pleiades, they find that the K-type stars in IC 4665 appear to rotate more slowly than one would expect at $\sim$30 Myr. Finally, a recent survey reported rotation periods for 20 IC 4665 members with masses $< 0.5 M_{\odot}$ (Scholz et al., 2009). They show that all of these low-mass stars are rotating rapidly (period $\leq 1$

day), a finding similar to studies of other PMS clusters (e.g. Irwin et al., 2008).

### 3.3.2 New SPOCS $BVI_c$ Observations

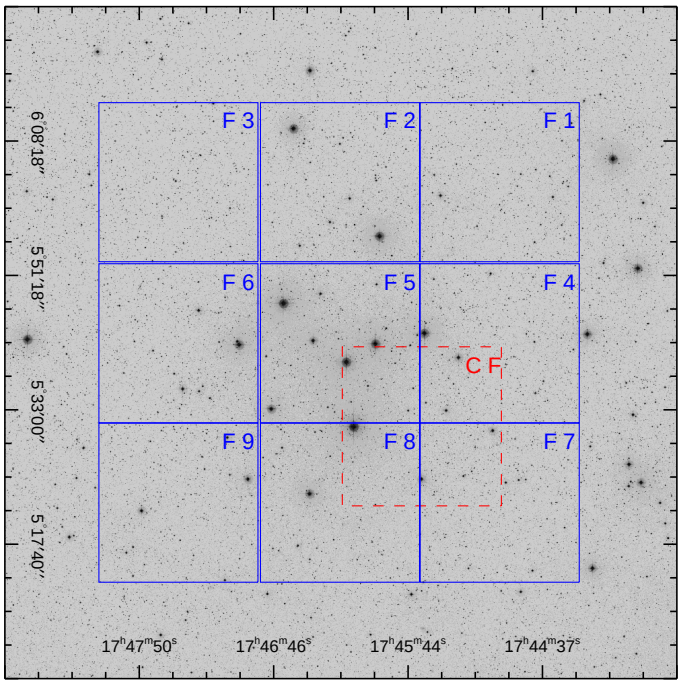


Figure 3.3: Digital Sky Survey image of the areal region covered by our SMARTS IC 4665 survey. Each square represents an observed field (coordinates given in Table III.1). Also plotted is the overlapping control field (CF) identified by the red dashed box. The image was obtained using the CADC DSS online server.

We observed IC 4665 as part of the SPOCS survey during the nights of 15, 16 & 17 of September, 2005. Nine fields were observed covering a uniform $3 \times 3$ mosaic grid of CCD fields covering approximately one square degree, centered on R.A.(J2000):$17^h46^m13.5^s$ and Dec(J2000):$+05°41'52''$. We employed exposure times of 100, 50, and 25 seconds for the B-, V-, and $I_c$-band observations, respectively. The

Table III.1. Summary of SMARTS 1.0 m Observations of IC 4665

| IC 4665 Field[b] | R.A.[a] [HH:MM:SS] | Dec[a] [DD:MM:SS] | Date of Observation |
|---|---|---|---|
| F1 | 17:47:29.8 | +06:01:00.0 | 16/Sept/2005 |
| F2 | 17:46:13.5 | +06:01:00.0 | 16/Sept/2005 |
| F3 | 17:44:56.3 | +06:01:00.0 | 17/Sept/2005 |
| F4 | 17:47:29.8 | +05:41:52.0 | 15/Sept/2005 |
| F5 | 17:46:13.5 | +05:41:52.0 | 15/Sept/2005 |
| F6 | 17:44:56.3 | +05:41:52.0 | 17/Sept/2005 |
| F7 | 17:47:29.8 | +05:22:56.0 | 15/Sept/2005 |
| F8 | 17:46:13.5 | +05:22:56.0 | 16/Sept/2005 |
| F9 | 17:44:56.3 | +05:22:56.0 | 16/Sept/2005 |
| CF | 17:46:52.6 | +05:32:00.0 | 15/Sept/2005 |
| CF | 17:46:52.6 | +05:32:00.0 | 17/Sept/2005 |

[a]Coordinates are Y4KCam field centers. All coordinates are J2000.0 epoch.

[b]F'n'-fields represent the main survey area of the cluster in a $3 \times 3$ mosaic covering about one square degree centered close to the cluster's WEBDA coordinates. Photometric data for a control field (CF) were also procured to allow us to assess the photometric integrity of the dataset.

central coordinates of each IC 4665 field for which BVI$_c$ photometry was obtained are shown in Fig. 3.3 and summarized in Table III.1. All photometric data were reduced using the procedure outlined in Section 3.1. We identified 7359 point sources in the SPOCS images, with all but 452 objects having matches within 3 arcseconds of a known object in the 2MASS database (Skrutskie et al., 2006). A visual presentation of our full BVI$_c$ photometric catalog is shown in Fig. 3.4, in which we plot V versus $B-V$ and $V-I_c$ CMDs along with D'Antona & Mazzitelli (1997) fiducial isochrones.

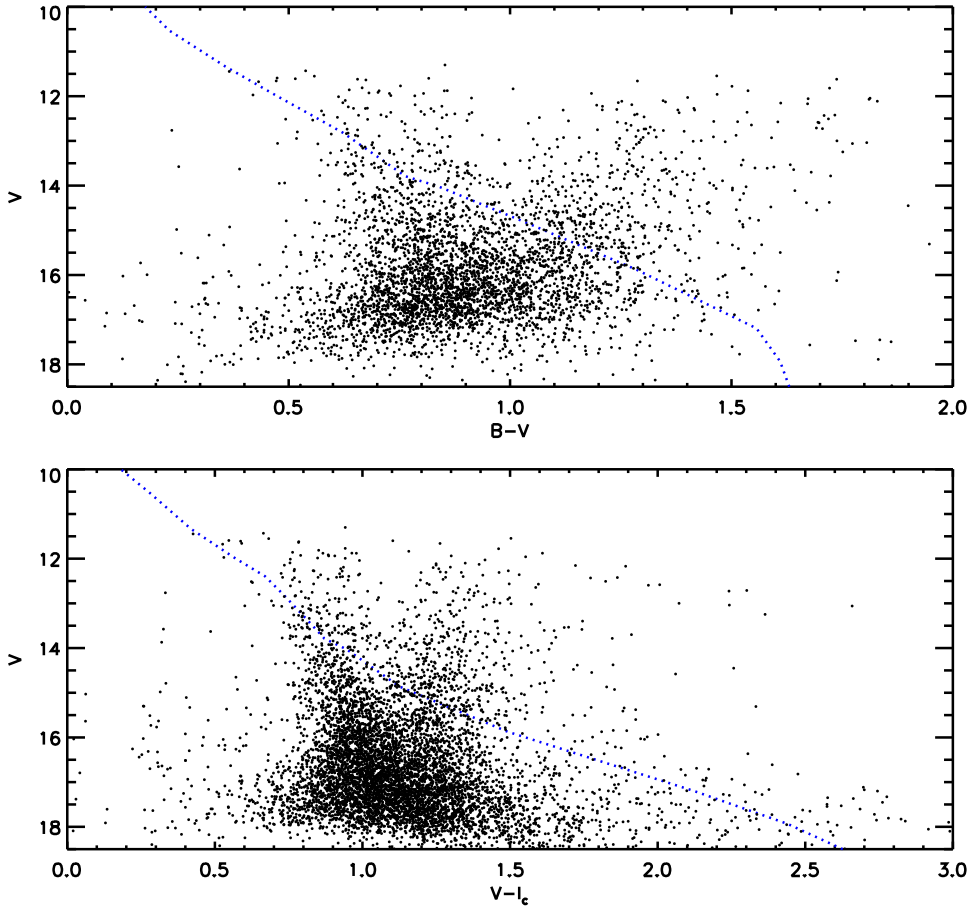


Figure 3.4: Color-magnitude diagrams for our full photometric catalog for the region of IC 4665 is plotted (black dots). Also provided are D'Antona & Mazzitelli (1997) isochrones (blue dotted line) for the cluster's lithium depletion boundary age (27.8 Myr; Manzi et al., 2008) and HIPPARCOS distance (355 parsecs; van Leeuwen, 2009).

### 3.3.3 Comparison of SPOCS Photometry to Prosser (1993)

Existing studies of IC 4665 solar-type stars rely on the photometry from the P93 study, and it is therefore imperative that we determine the reliability of their photometric system as compared to our SPOCS data. A detailed examination of the standardization procedure of P93 shows that, although nightly standard stars were used to derive extinction coefficients and color-transformation equations, the zero-points of their $BVI_k$ photometric system are tied to a solitary blue, high-mass B9e star. This star, HD 161261, has subsequently been found to have V-band variability on the order of 0.1 magnitudes (Kazarovets & Samus, 1997), which might be due to a binary component (Pourbaix et al., 2004), as well as an infrared excess typical of rapidly rotating Be stars (Yudin, 2001). Not surprisingly, we observe systematic offsets between the P93 photometry and our own that are likely a result of this extrapolation of standardized photometry derived from such a single, blue, possibly variable and binary standard star.

For stars in common to both catalogs, we plot in Fig. 3.5 comparisons between the P93 study and our own $V$, $B-V$, and $V-I_c$ photometric datasets. We translated the P93 Kron $V-I$ colors to the Cousins system using the formalism given in Bessell & Weis (1987). We see a significant amount of scatter in the P93 photometry ($\sim$0.1 mag in V; $\sim$0.2 in $B-V/V-I_c$) compared to our optical catalog. In addition, there appears to be a systematic offset of $\sim$0.05 mag in V, $B-V$, and $V-I_c$ for the faintest/reddest P93 objects. Such a magnitude of photometric scatter and systematic offset may cause

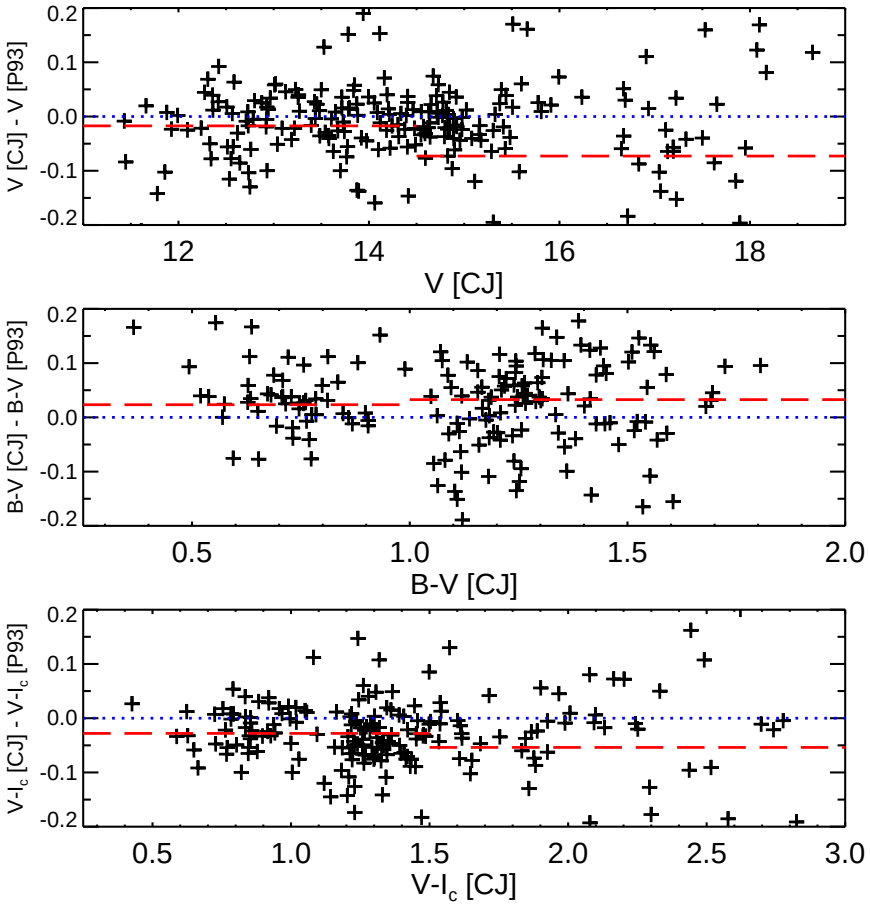


Figure 3.5: $V$, $B-V$, and $V-I_c$ residual comparison plots for the P93 catalog and our optical catalog (CJ). Our translation from P93 $V-I_k$ to $V-I_c$ is described in the text. The blue dotted lines indicate equality between the systems, whereas the red dashed lines are calculated means for V $< 14.5$ & $\geq 14.5$; $B-V < 1$ & $\geq 1$; $V-I_c < 1.5$ & $\geq 1.5$, respectively.

significant problems when trying to calibrate both color and magnitude relationships for stars in IC 4665; therefore, for the purpose of this chapter, we will preferentially employ our, new precisely standardized BVI$_c$ photometry in all subsequent analysis.

### 3.3.4 Pre-Main-Sequence Age

In the P93 study, the authors reported that they were unable to determine the age of IC 4665 from the location of the low-mass pre-main-sequence, due to the lack of a

defined low-mass sequence in their CMD. This may have been the result of systematic scatter in their photometry and/or their cluster membership determination being based on unreliable proper motion data. More recently, the infrared study of IC 4665 by de Wit et al. (2006) suggests that the cluster has an age of 50 to 100 Myr based on the location of its low-mass cluster sequence. However, de Wit et al. note that an accurate age for the cluster is difficult to measure due to the large amount of field star contamination present in their survey.

A quick examination of the full IC 4665 CMD reveals that we too confirm that an accurate fit of the cluster sequence is particularly difficult to achieve due to field star contamination in our color-magnitude diagram (see Fig. 3.4). While IC 4665 lies relatively far from the Galactic plane ($b$= +17°) the level of contamination along the CMD suggests that there is a high stellar density in the cluster's line of sight through the Galaxy. To account for the field star contamination in the IC 4665 CMDs, we further constrain our analysis to those stars having ancillary membership indicators from a disparate range of extant photometric and spectroscopic observing campaigns. In the first instance, we positionally matched our photometric catalog with data from the following sources: three catalogs of stars with common kinematic properties (proper motions — P93; radial velocities — Prosser & Giampapa 1994; Jeffries et al. 2009a), stars with X-ray emission Giampapa et al. 1998, two catalogs of stars with significant lithium absorption (Martin & Montes, 1997; Jeffries et al., 2009a), three catalogs of stars exhibiting strong H$\alpha$ emission (EW$_{H\alpha} > 0$ Å— P93;

Martin & Montes 1997; Jeffries et al. 2009a), and finally, two catalogs of stars with short rotation periods in the region of IC 4665 (Allain et al., 1996; Scholz et al., 2009). X-ray and H$\alpha$ emission (coronal and chromospheric), the presence of lithium in stellar photospheres, and rapid rotation are all indicators of youth for low-mass stars, and therefore we can exploit such surveys in order to segregate young cluster members from the typically much older field star populations. In Fig. 3.6, we plot the CMDs with stars identified from the various membership catalogs. We will subsequently exclude proper-motion-selected members from our cluster catalog due to the lack of a clear (pre-) main-sequence in its CMD (see Fig. 3.6; top panels), *viz*, proper motion must be an extremely poor membership criterion for this cluster. This can be explained by the similarity of the cluster's systemic proper motion to that of the general field population, justifying the exclusion of the cluster's proper motion catalog from all subsequent analysis of IC 4665 (see Jeffries et al., 2009a).

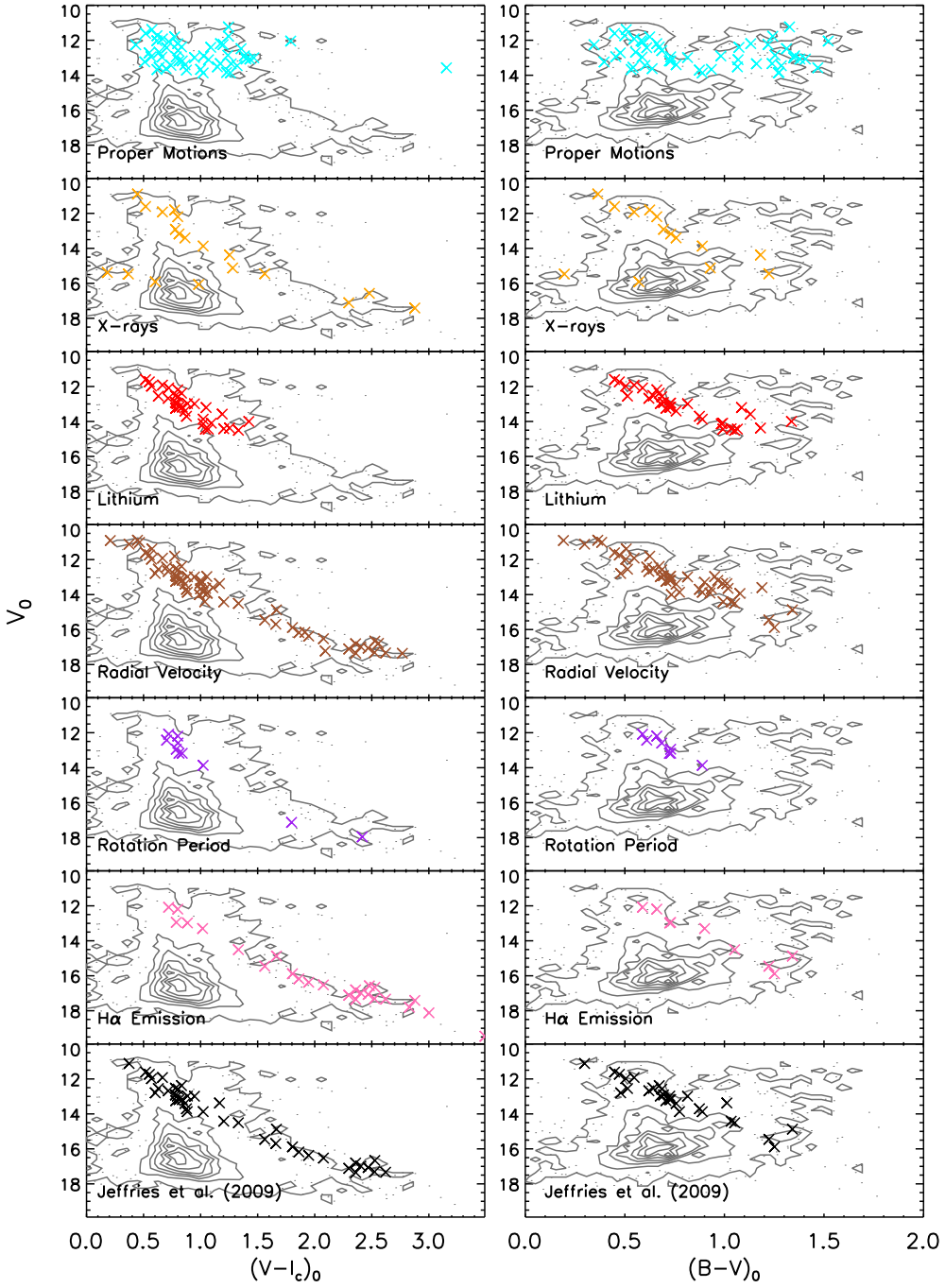


Figure 3.6: Intrinsic $V - I_c$ and $B - V$ color-magnitude diagrams for IC 4665 are presented (object density given by gray contours) with cluster candidate members identified (crosses) using a secondary membership criterion, labeled in the lower-left corner of each panel (see text for source references). We use a cluster reddening of $E(B - V) = 0.174$ (WEBDA), an $E(V - I) = 1.25 \times E(B - V)$, and an $A_v = 3.12 \times E(B - V)$ relation, in order to derive intrinsic colors and magnitudes. Colors in each panel correspond to the associated data points in Figure 3.8.

We recognize that the membership catalogs cited above contain varying levels of field contamination, as well as biases based on their color and/or magnitude ranges. For instance, although our catalog of radial velocity members contains the largest number of stars spread over the largest range of colors, it also has a high probability of field star contamination due to the similarity of the kinematic distribution of the cluster compared to the field (Jeffries et al., 2009a). On the other hand, the catalog of stars showing X-ray emission has a much lower probability of contamination due to the ubiquitous nature of high magnetic activity in young stars compared to old field stars. However, the relatively low number of stars identified can be attributed to the fairly narrow field-of-view of the ROSAT X-ray satellite compared to the on-sky distribution of apparent cluster members. In an attempt to account for the relative power of using multiple membership criteria, Jeffries et al. (2009a) produced a catalog of highly probable members of IC 4665 using a combination of kinematic motions, lithium content, optical and 2MASS photometry, and spectral-indices indicators as filters to remove foreground and background field star interlopers in the cluster catalog. We include this list of high-fidelity cluster members in our analysis, and note that it is most current, up-to-date compilation of *bona fide* IC 4665 members.

To find an initial estimate for the age of IC 4665 using its low-mass population, we plot in Fig. 3.7 the $V$ versus $V - I_c$ color-magnitude diagram for confirmed members of three open clusters; for IC 4665, the membership catalog from Jeffries et al. (2009a) is used, whereas for the 35 Myr old NGC 2547 cluster, we employ the pho-

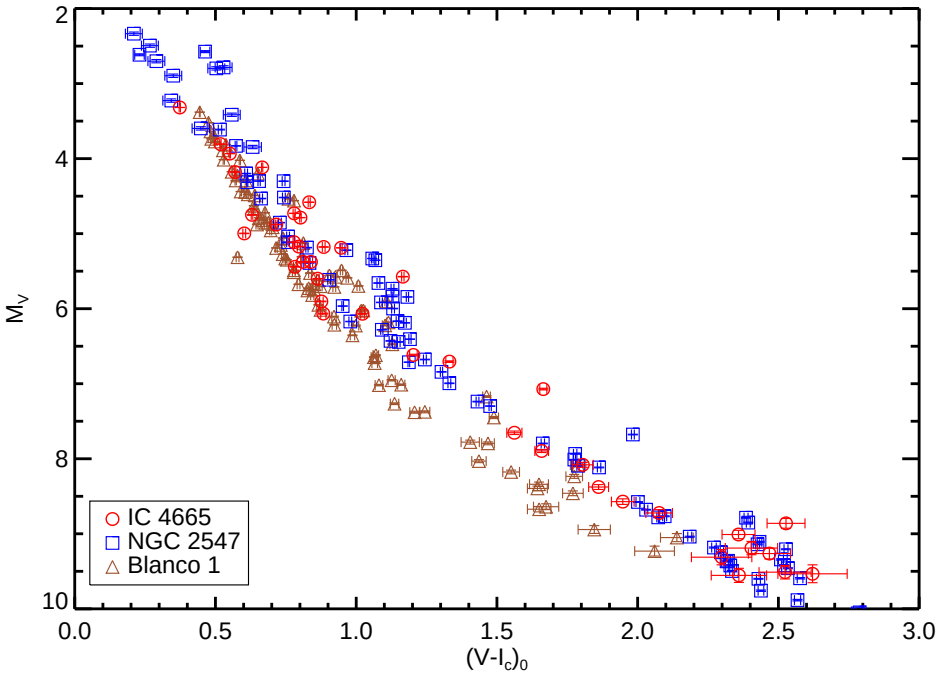


Figure 3.7: Absolute $V$ versus intrinsic $V - I_c$ magnitudes are plotted for the open clusters IC 4665, NGC 2547 (35 Myr), and Blanco 1 (80 Myr). Intrinsic colors and magnitudes were calculated using cluster's $E(B-V)$ data (WEBDA), an $A_v = 3.12 \times E(B-V)$ and an $E(V-I_c) = 1.25 \times E(B-V)$ relation. The apparent-to-absolute magnitude conversion was achieved using the appropriate HIPPARCOS distances reported in van Leeuwen (2009). See text for data sources.

tometric membership catalog from Naylor et al. (2002). Finally, for the ∼100 Myr old Blanco 1 cluster, our SPOCS data (see Section 3.4 and James et al. (2010) provides a photometric catalog of kinematic members. While some photometric scatter is apparent, probably due to binarity and a small number of cluster non-members, these CMDs evidently show that the lower-mass stars in IC 4665 [$(V - I_c)_o > 1.00$] lie systematically above the Blanco 1 main-sequence. In fact, in this color range IC 4665 stars have colors and magnitudes closely matching the corresponding stars in NGC 2547, suggesting that at least photometrically, IC 4665 is of a comparable

age to NGC 2547, *i.e.,* $\sim 30 - 40$ Myr. Although this age estimate is insightful, we now establish a more robust determination of the cluster's age using the $\tau^2$ isochrone fitting technique described in Section 3.2.

In Fig. 3.8 we show the best-fit ages and distance moduli (hereafter DM), derived from our $\tau^2$ fitting procedure, for each of our seven IC 4665 membership catalogs (5 individual catalogs described previously, the catalog from Jeffries et al. (2009a), and a combined catalog that includes any object with some type of membership criterion), and three stellar evolution models representing two different colors ($B-V$ and $V-I_c$). We note that we were unable to find a best-fit age and distance solution for every membership catalog using each model and/or color; the rotation period and H$\alpha$ catalogs were particularly problematic. The failure of these model to converge is primarily due to the specifics of each membership catalog (*e.g.,* large amounts of contamination, not having a wide color-magnitude range in data points, *etc.*).

In the following analysis we choose to use the membership catalog from Jeffries et al. (2009a) as the exemplar best-fit age and DM for the different models and colors, as it has the lowest probability of contamination by field stars. Nevertheless, modeling multiple membership catalogs allows us to identify the possible range of ages and DM one should expect when using specific membership criteria to identify cluster members. In Table III.2, we list the median of the ages and distances, derived for all membership criterion catalogs, together with the observed range of values from our best-fit isochrone for each color and stellar model. We also include the best-fit

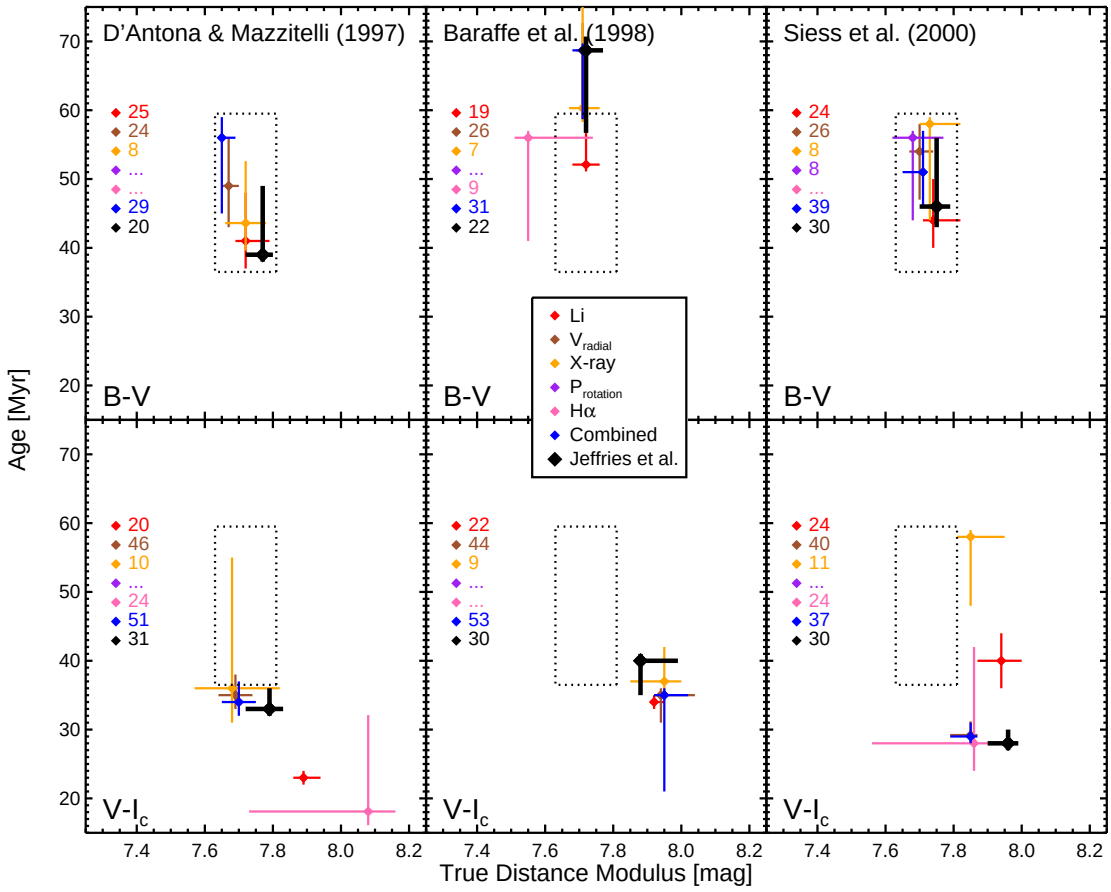


Figure 3.8: Best-fit ages and intrinsic distance moduli resulting from our $\tau^2$ isochrone modeling of the low-mass members of IC 4665. Upper panels represent results for $B-V$ CMDs, while the lower panels represent the $V-I_c$ ones. Each data point's color is described by the legend in the center of the plot (see text for source references). Along the left of each plot, the final number of data points are provided that were used in the CMD modeling after having applied a soft clipping process. Data sets for which we were unable to find a best-fit age and DM, due to the $\tau^2$ model isochrone not converging, are identified by '...' instead of the number of data points used given on the left. For comparison purposes, we plot a black dashed-line box in each box, which represents the approximate range of ages and DM that result from the modeling of the $B-V$ CMD using the D'Antona & Mazzitelli isochrones (upper left panel).

Table III.2. Isochrone Ages and Distances for IC 4665

| Model | Parameter[a] | Median[b] | | Jeffries et al. | |
|---|---|---|---|---|---|
| | | $B-V$ | $V-I_c$ | $B-V$ | $V-I_c$ |
| DAM97[c] | Age [Myr] | 48.0±11.0 | 38.5±16.5 | $39.0^{+10}_{-1}$ | $32.8^{+3}_{-1}$ |
| | D.M. [mag] | 7.72±0.08 | 7.76±0.19 | $7.77^{+0.03}_{-0.05}$ | $7.79^{+0.04}_{-0.07}$ |
| | Dist. [pc] | 350±13 | $370^{+19}_{-43}$ | $358^{+5}_{-8}$ | $361^{+7}_{-11}$ |
| BCAH98[c] | Age [Myr] | 65.2±14.1 | 31.5±10.5 | $68.7^{+2}_{-12}$ | $39.6^{+1}_{-5}$ |
| | D.M. [mag] | 7.72±0.05 | 7.94± 0.10 | $7.72^{+0.05}_{-0.01}$ | $7.88^{+0.11}_{-0.01}$ |
| | Dist. [pc] | 350±8 | $387^{+18}_{-17}$ | $350^{+8}_{-2}$ | $377^{+19}_{-2}$ |
| SDF00[c] | Age [Myr] | 49.5±9.5 | 43.0±16.0 | $46.4^{+10}_{-3}$ | $27.5^{+2}_{-1}$ |
| | D.M. [mag] | 7.72±0.10 | 7.86±0.11 | $7.75^{+0.04}_{-0.05}$ | $7.96^{+0.03}_{-0.06}$ |
| | Dist. [pc] | 350±16 | $373^{+19}_{-18}$ | $355^{+6}_{-8}$ | $391^{+6}_{-11}$ |

[a]Intrinsic distance moduli were measured using an extinction of $A_V = 0.54$ mag.

[b]Median of values from all membership catalogs for a given model and color. Uncertainties quoted are the range of possible values given the errors on the individual best-fit isochrone models. We did not include H$\alpha$ isochrone measurement in median and range calculation due to their large uncertainties.

[c]DAM97 – D'Antona & Mazzitelli (1997) ; BCAH98 – Baraffe et al. (1998) ; SDF00 – Siess et al. (2000)

solution for the Jeffries et al. (2009a) membership list.

For the most part, the best-fit ages and DM found for all three PMS models are typically within their individual errors of each other, suggesting that statistically they all three are in agreement of IC 4665's age and distance. However, we do find that some points lie beyond $1\sigma$ from the other derived ages and DM (*e.g.*, the best-fit parameters found for the $V - I_c$ Li catalog using the D'Antona & Mazzitelli models), and are most likely the result of a poor fit due to limited or discrepant data. This is evidence for the strength of modeling multiple membership catalogs, that we are able to clearly adjudge whether an individual catalog's measured age and DM is discrepant due to a poor isochrone fit or otherwise.

Here, we would like to highlight some results of our PMS isochrone modeling of IC 4665. First, if we focus solely on the $B - V$ isochrones, we find good agreement in the measured DM for all three models, whereas only the ages for the D'Antona & Mazzitelli and Siess et al. models are in agreement with the best-fit values for Baraffe et al. model isochrones yielding systematically older ages (although they are within $1\sigma$ of the other PMS models). For $V - I_c$, the derived ages for the three models are in close agreement, however, the Baraffe et al. models again yield slightly older ages. Furthermore, Baraffe et al. and Siess et al. models yield derived DM that are larger than the D'Antona & Mazzitelli $V - I_c$ models.

Our results also show that all three models give systematically older ages for the $B - V$ CMDs compared to the $V - I_c$ ones. The color-dependent age discrepancies

seen are of order ∼10 Myr, and are on the same order of offsets seen in other young open clusters when comparing isochrone fits using two different colors (see Naylor et al., 2002). We also note that for the Baraffe et al. and Siess et al. models, there is a color-dependent offset of ∼0.2 magnitudes seen in the measured DM from the $V - I_c$ CMDs. We find the D'Antona & Mazzitelli models provide the most consistent age and DM between the IC 4665 $B - V$ and $V - I_c$ CMDs.

At this point, we caution the reader that the observed model- and color-dependent discrepancies in ages and DM are likely due to many different influences, and may not necessarily represent problems with low-mass stellar evolution models. Indeed, these three models include different physics (*e.g.,* treatment of convection) that almost certainly must lead to different predicted luminosities and effective temperatures at given ages (for detailed discussion, see Siess et al., 2000; Hillenbrand & White, 2004); however, the observed offsets may also be the result of systematics in the modeling process. For example, the ages derived from the $B - V$ CMDs may be older due to the $B - V$ color of late-type stars becoming nearly insensitive to changes in effective temperature, which consequentially makes it difficult to assign a PMS isochrone to such low-mass stars. In addition, the *Pleiades tuning* method may also introduce systematic errors into our analysis. For instance, Stauffer et al. (2007) find that low-mass stellar evolution models have trouble fitting the optical and infrared colors of low-mass members of the Pleiades. Because we calibrate our IC 4665 colors and magnitudes using an empirical fit to the Pleiades main-sequence, any such systematics

in the Pleiades tuning method are included in our isochrone modeling procedure. More generally however, by employing the *Pleiades tuning* method we are assuming that the colors and magnitudes of the Pleiades main-sequence stars are representative of the younger stars in IC 4665. Unfortunately, our IC4665 dataset is relatively small compared to other well studied open clusters and does not include a complete, contaminant-free PMS, which therefore may not allow us to disentangle *all* of the different color- and model-dependent systematics affecting PMS isochrones modeling.

Keeping this in mind, we would nevertheless still like to derive a single PMS age and distance for IC 4665 for comparison purposes. Since the Jeffries et al. catalog is most likely to contain the highest number of *bona fide* IC 4665 members, we use the best-fit isochrone ages and DM from this catalog as representative of the cluster. First, we calculate the error-weighted mean age and DM between models for the $B-V$ and $V-I_c$ colors, separately. The errors on these values are asymmetric, so the weights for our means are based on whether the age/DM lies above or below the straight average, *e.g.,* if an age lies below the straight average, we then weight that data point using its upper error value. Using this approach, we find color-dependent ages of 30.6±3.5 and 49.3±9.0 Myr, as well as intrinsic DM of 7.88±0.05 and 7.75±0.01 mag (377±9 and 355±3 pc), for our $B-V$ and $V-I_c$ CMDs, respectively. Taking the weighted mean of these color-dependent values, we get a final PMS age and distance modulus for IC 4665 of 35.8±9.3 Myr and 7.78±0.07 mag (360±12 pc), for which the quoted errors are uncertainties in the mean.

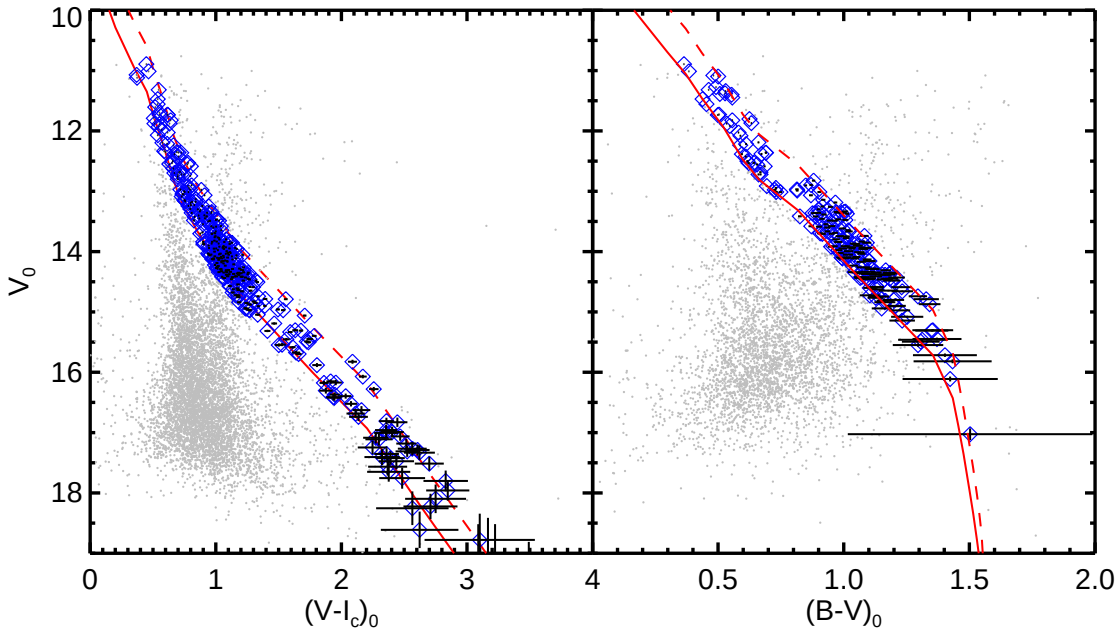


Figure 3.9: Intrinsic $V - I_c$ and $B - V$ color-magnitude diagrams for IC 4665 are plotted for our entire photometric catalog. Stellar objects having colors and magnitudes consistent, within their photometric errors, of a 36 Myr and 360 pc D'Antona & Mazzitelli model isochrone (red solid line) are highlighted (blue diamonds), together with the locus of its associated equal-mass binary sequence (red dotted line). Photometric data have been dereddened using an $A_V = 0.543$, an $E(B - V) = 0.174$ and an $E(V - I_c) = 0.2175$.

The entire photometric catalog of IC 4665 is plotted in Fig. 3.9 in the form of $V/V-I_c$ and $V/B-V$ CMDs; stars with photometric data consistent (within error) of the 36 Myr and 360 pc D'Antona & Mazzitelli isochrones are highlighted. For each of these candidate photometric members of IC 4665, we list their photometric properties in Appendix A. This photometric membership selection is based upon D'Antona & Mazzitelli, because our model- and color-averaged age and DM are most closely matched to the values we get from the individual modeling of the $V - I_c$ and $B - V$ CMDs compared to the theoretical PMS models generated by other authors (*e.g.*,

Baraffe et al. & Siess et al.). However, because the different best-fit isochrones have similar morphology irrespective of their different best-fit ages and distances, we do not expect this membership catalog to significatly change when using the other PMS models. Although this membership list most likely contains a high number of cluster members, its exclusive use in identifying members of IC 4665 is not recommended due to the non-zero probability of field star contamination in the catalog, especially where the Galactic field star distribution intersects the cluster main-sequence close to $(V - I_c)_0 \sim 1.00$ and $(B - V)_0 \sim 1.25$.

Previously, we have shown that the CMDs of IC 4665 members appear very similar to those of the ∼35 Myr old NGC 2547 cluster (see Fig. 3.7), which is now empirically supported by our PMS age determination for IC 4665. Moreover, the best-fit distance modulus that we derive for the cluster is in excellent agreement with the trigonometric parallax distance resulting from the recent re-reduction of the HIPPARCOS astrometric dataset by van Leeuwen (2009), which yields an intrinsic distance modulus of 7.75±0.21 mag (355±35 parsecs).

### 3.3.5 Upper-Main-Sequence Turn-Off Age

Comparing the positions of open cluster upper-main-sequences in color-magnitude space, Mermilliod (1981a) determines that IC 4665 had a nuclear turn-off age of 36 Myr. However, P93 suggest that the upper main-sequence for IC 4665 is best comparable to that of the ∼70 Myr open cluster $\alpha$ Persei, and if effects due to rapid

rotation are taken into account, the upper main-sequence is most like the Pleiades CMD, suggestive of a cluster age near to ∼100 Myr.

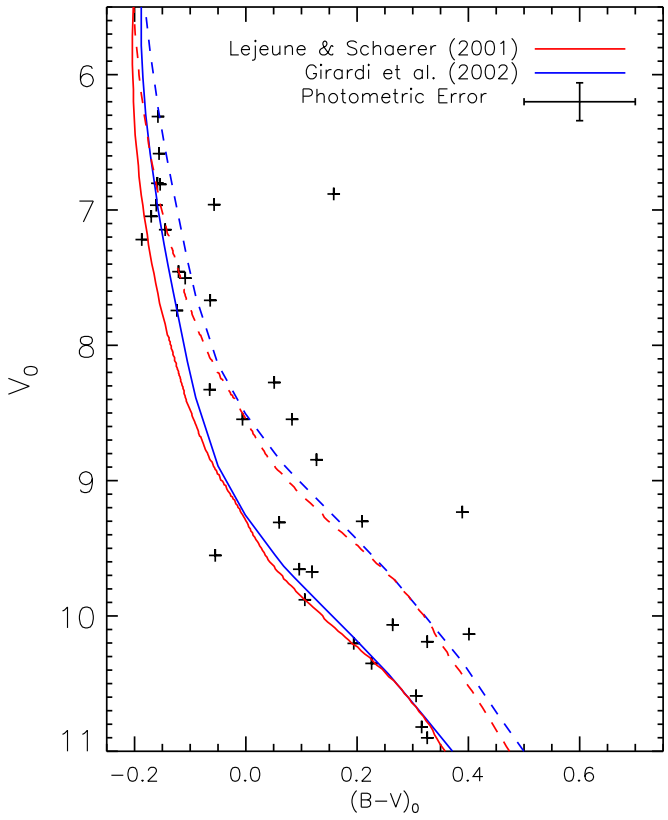


Figure 3.10: High-mass (V<11 mag) color-magnitude diagram using photometric data from the optical catalogs of Prosser (1993) and Menzies & Marang (1996). Also plotted are the best-fit isochrones (solid lines) from our upper-main-sequence $\tau^2$-modeling using the two high-mass stellar models detailed in the legend, as well as their associated equal-mass binary sequences (dotted lines). The adopted uncertainty for the optical data is shown.

In light of this disagreement in nuclear turn-off age for IC 4665, we now use the $\tau^2$ technique, outlined in Section 3.3.4, to measure an age and distance for only the high-mass cluster members. Because the main-sequence turn-off for IC 4665 is located at

a V magnitude brighter than our CTIO photometric survey saturation limit, we use the bright ($V < 11$ magnitude) optical data from P93 and Menzies & Marang (1996). Unfortunately, neither catalog contained published individual uncertainties on their photometric data; therefore, we set the error in the $B$ and $V$ magnitudes to the level of observed scatter in P93 data for stars with $V < 14$ mag found in our catalog comparison ($\Delta V = 0.07$ mag and $\Delta B-V = 0.1$ mag, see Section 3.3.3). Interestingly, this magnitude of uncertainty is similar to the photometric variability observed in the star used for P93's zeropoint calibration, perhaps providing an explaination for the observed scatter between the P93 and our photometric systems.

Following Naylor (2009), we use upper-main-sequence models from Lejeune & Schaerer (2001) and Girardi et al. (2002), coupled with solar-metallicity bolometric corrections and effective temperature to color conversions, as well as color dependent reddening vectors from Bessell et al. (1998). We find upper-main-sequence ages for IC 4665 of 41±12 and 42±12 Myr and intrinsic DM of 7.76±0.04 and 7.77±0.04 mag (356±10 and 358±15 parsecs) for the aforementioned high-mass stellar evolution models, respectively. We plot in Fig. 3.10 the photometric data used in our high-mass CMD modeling, as well as our two best-fit isochrones. We note that these age measurements are not thoroughly constrained due to the lack of high-mass cluster members tracing out IC 4665's upper-main-sequence; nevertheless, we find that the nuclear turn-off age for IC 4665 we have calculated is within the error range of the previous estimate from Mermilliod (1981a), though it is significantly younger

than the $\alpha$ Persei-like or Pleiades-like age estimations from P93. Also, if our error estimates for the upper-main-sequence photomtery are over or underestimated, then the uncertainties derived for the best-fit ages and distances will likewise be over or underestimated, respectively.

Naylor (2009) recently investigated the differences observed in isochronal ages measured from upper- and lower-main-sequences of young ($< 100$ Myr) open clusters. They find a trend of PMS isochrone ages being $\sim$1.5 times smaller than nuclear turn-off ages for a selection of young open clusters. Interestingly, our current study on IC 4665 shows the upper-main-sequence isochrone models have best-fit ages that are similar (within $\sim$6 Myr) to the PMS isochrone age while using the $B-V$ low-mass CMD. However, if we use the PMS isochrone age from the $V-I_c$ CMDs (30.6$\pm$3.5 Myr) or our inter-model $V-I_c$ mean PMS age (35.8$\pm$9 Myr), we find $\sim$1.5 times these PMS ages are formally within the error budget of the nuclear turn-off age (*i.e.*, $1.5\times30.6\pm3.5$ Myr $= 45.9\pm3.5$ Myr and $1.5\times35.8\pm9$ Myr $= 53.7\pm9$ Myr, compared to our turn-off age of $42 \pm 12$ Myr), corroborating the Naylor (2009) findings.

### 3.4 Zero-Age-Main-Sequence Cluster: Blanco 1

Blanco 1 is a relatively nearby, open cluster (250 pc, $<$ 150 Myr; WEBDA open clusters database) that is of considerable scientific interest due to its high Galactic latitude ($b = -79^{\circ}$) and comparable age to the well-studied Pleiades open cluster ($\sim 80-120$ Myr; Meynet et al. 1993, $[Fe/H] = -0.034 \pm 0.024$; Boesgaard & Friel

1990). Considerable interest in the cluster has been driven by its reported metal-rich nature ($[Fe/H] = +0.23$; Edvardsson et al. 1995), although a more recent, self consistent determination now makes the cluster of near-solar composition ($[Fe/H] = +0.04 \pm 0.04$; Ford et al. 2005). The combination of the cluster's systemic velocity ($RV_{sys}$=+5.5 km $s^{-1}$; Mermilliod et al. 2008), its Galactic latitude, and distance below the Galactic plane (∼250 pc) suggests that, if Blanco 1 has an age of >50 Myr, it should have formed in or near the Galactic plane. The unusual location of Blanco 1 makes it unique among the well-studied, young (≪1 Gyr) open clusters.

Similar to IC 4665, the age of Blanco 1 has continued to be a matter of debate. Published ages for this open cluster range from ∼50 – 150 Myr, including an approximate age of 130 Myr as determined from its lithium depletion boundary (see Chapter V). This uncertainty in the cluster's age is primarily a direct result of an insufficient and poorly defined membership catalog, mostly due to inadequately calibrated photographic photometry (see Section 3.4.1). This has subsequently hampered Blanco 1 from becoming a benchmark zero-age-main-sequence cluster. In this Section, we use SPOCS photometric data for Blanco 1 proper-motion cluster members and the $\tau^2$ technique outlined in Section 3.3 to calculate new isochronal ages based on the cluster's upper- and lower-main-sequences.

### 3.4.1 Extant Optical Photometry of Blanco 1

de Epstein & Epstein (1985) performed a large-scale survey of the central 1.5

deg$^2$ of the cluster, utilizing archival photographic plates, obtained at the El Leoncito Observatory in San Juan, Argentina. They identified ∼1500 stellar objects down to a limiting magnitude of V≃ 16.5, which corresponds to a late-K spectral type for the reddening and distance of Blanco 1. These authors claim cluster membership for ≃ 10% of their sample although, as they themselves note, classification of stars fainter than V= 12.6 must be considered tentative. This is because they produced a photometric dataset based on a calibration between their photographic magnitude system and the then-existing photoelectric dataset for Blanco 1 stars, which unfortunately must be extrapolated for stars fainter than V≃12.6. This photometry, being the only optical data available for ∼20 years, has been relied upon by many studies of Blanco 1, including those characterizing stars with V>12.6 (see ROSAT and XMM-Newton X-ray surveys of Blanco 1 Micela et al., 1999a; Pillitteri et al., 2004).

### 3.4.2 New SPOCS UBVI$_c$ Photometry and Proper Motions

In light of the paucity of precise and accurate photometric data for Blanco 1, especially for fainter cluster members, a recent SPOCS study produced a standardized UBVI$_c$ CCD photometric dataset for the central 1.6×1.3 deg$^2$ of Blanco 1, centered on RA(2000): $00^h05^m$; Dec(2000): $-30°02'.4$. All photometric data were reduced using the procedure outline in Section 3.1. Our photometric catalog contains 1,963 stellar objects with a limiting magnitude of V≃17. Fig. 3.11 shows the V versus $B-V$ and $V-I_c$ CMDs based on this photometry along with the fiducial DAM97 isochrone for

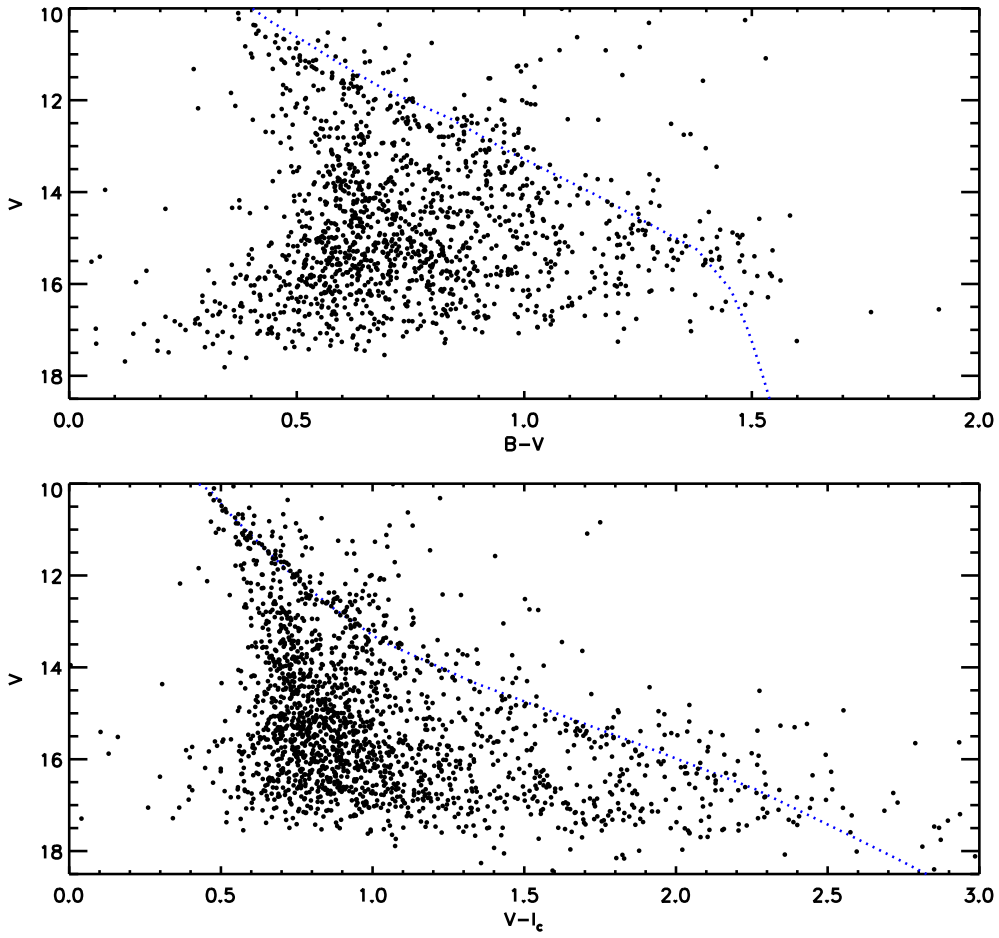


Figure 3.11: Color-magnitude diagrams for our full photometric catalog for the region of Blanco 1 is plotted (black dots). Also provided are D'Antona & Mazzitelli (1997) isochrones (blue dotted line) for the cluster's lithium depletion boundary age (130 Myr; see Chapter V) and HIPPARCOS distance (207 parsecs; van Leeuwen, 2009).

Blanco 1.

### 3.4.3 Comparison of SPOCS Photometry to de Epstein & Epstein (1985)

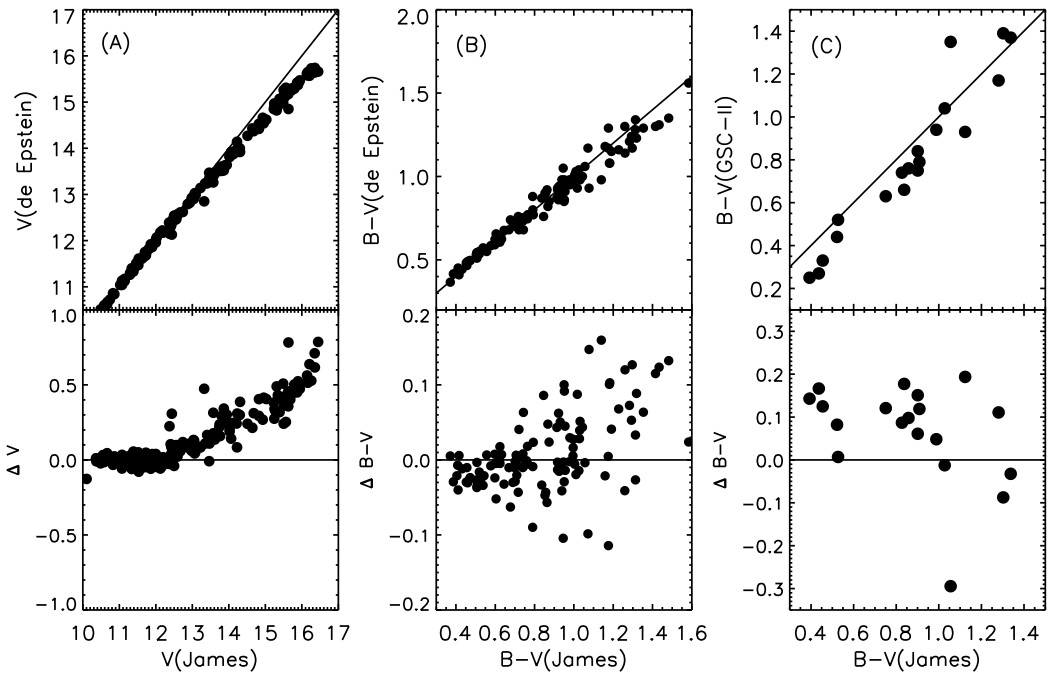


Figure 3.12: $V$ and $B-V$ comparison plots for the de Epstein & Epstein (1985) (A, B) and GSC-II (C) photometric catalogs with our new SPOCS photometry are presented. The solid lines indicate equality between the systems, and are not fits to the data.

In Fig. 3.12 A & B, a comparison between the photometry of de Epstein & Epstein (1985) and the SPOCS survey is plotted. Clearly, for magnitudes greater than V$\sim$ 12.5, there is an increasingly large offset between the two catalogs, as well as an increase in the $B-V$ scatter for stars redder than $\sim 0.7$. This scatter is at a $1\sigma$ level of 0.05

for $B-V > 0.7$. These effects are most likely due to the limitations in photographic-to-photoelectric calibration of the de Epstein & Epstein catalog. We also include a comparison between our new SPOCS photometry and the $B-V$ colors used in the X-ray study of Pillitteri et al. (2004), where they use GSC-II $B$ and $R$ magnitudes transformed onto a version of the standard $B-V$ color system. Plotted in the third panel of Fig. 3.12 are the results of such a comparison, where a clear systematic offset between the two color systems is apparent.

### 3.4.4 New Proper Motions for Blanco 1

Along with our new photometry, we have calculated proper motions for the stars in our SPOCS survey. Proper motions were deduced from a total of 32 sets of photographic and CCD observations with a time base-line of 40 years, ending with our most recent SPOCS data in September 2007. Proper motions and positions were calculated using a variant of the central plate-overlap method (*e.g.,Herbig & Jones, 1981)* and the UCAC2 catalog (Zacharias et al., 2004) as a reference frame. The precision of the proper motions, for stars with optimal image properties, is 0.3 mas yr$^{-1}$.

We used these proper motions to derive membership probabilities for stars in our SPOCS Blanco 1 fields. The formal proper-motion membership probabilities, $P_\mu$, were calculated using the probability definition formulated by Vasilevskis et al. (1958): $P_\mu = \Phi_c/\Phi_c + \Phi_f$, where $\Phi_c$ is the number distribution of cluster stars and $\Phi_f$ is the number distribution of field star proper motions. The distributions of field and

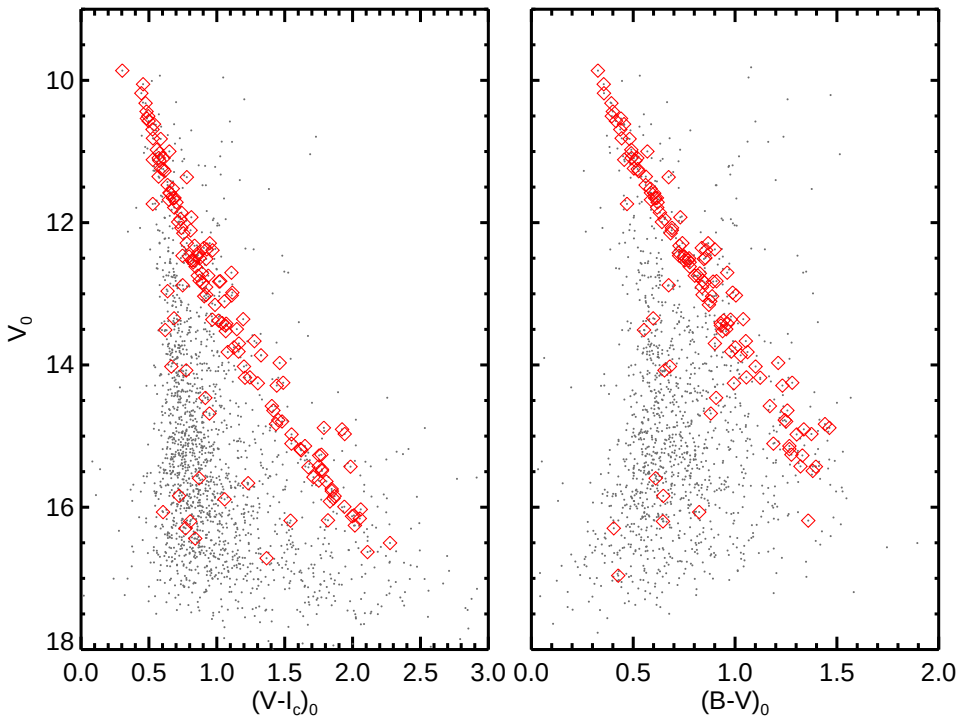


Figure 3.13: Intrinsic $V - I_c$ and $B - V$ color-magnitude diagrams for Blanco 1 are plotted (black points) for our entire photometric catalog. Stellar objects having proper motions consistent with cluster membership are identified with red symbols. Photometric data have been dereddened using an $A_V = 0.05$, an $E(B - V) = 0.016$ and an $E(V - I_c) = 0.02$.

cluster stars in the area of Blanco 1 are derived using the so-called local sample method (Platais et al., 2007). The separation between the cluster and field is convincing for the entire magnitude range. A full description of the reduction and analysis of these new astrometric data will be given in James et al. (2010). In Fig. 3.13, we indicated the 150 stars with membership probabilities $\geq 1\%$, clearly showing that the majority of these stars trace out the cluster sequence for V$\sim$10.5-17.

### 3.4.5 Pre-Main-Sequence Age

Compared to other well-studied open clusters, the low-mass cluster sequence of Blanco 1 has been relatively unexplored. The only survey that has attempted to identify the cluster's PMS is Moraux et al. (2007), where they use near-infrared photometry to establish low-mass members of the cluster. Due to the unavailability of ancillary membership constraints (*e.g.,* proper motions), Moraux et al. was only able to produce a catalog of possible cluster members. Subsequently, the lack of a clear sequence in their data made it impossible to fit a PMS isochrone and derive a cluster age.

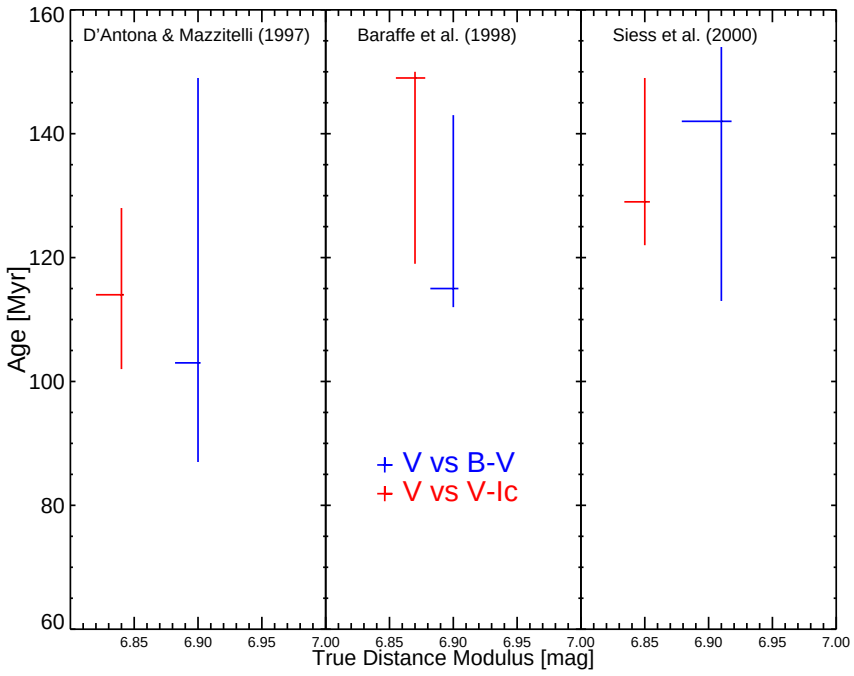


Figure 3.14: Best-fit ages and intrinsic distance moduli resulting from our $\tau^2$ isochrone modeling of the low-mass members of Blanco 1. Blue symbols represent results for $B-V$ CMDs, while the red symbols represent the $V-I_c$ ones. The model used is given at the top of each panel.

In light of this, we employ our new SPOCS photometry and new proper motions in an attempt to clearly define the low-mass sequence of Blanco 1. As we showed in Fig. 3.13, we identified proper motion members for Blanco 1 from V = 10.5 to 17. Using the $\tau^2$ technique outlined in Section 3.2, we use the colors and magnitudes of these proper motion members to derive best-fit isochrones from current stellar evolutionary models. Our grid of theoretical isochrones were computed from the solar-metallicity Baraffe et al. (1998), D'Antona & Mazzitelli (1997), and Siess et al. (2000) PMS models. Currently, we only defined membership to Blanco 1 from proper motions; therefore, we are unable to perform as thorough of a $\tau^2$ analysis as we did for IC 4665 at this time. However, because proper motions do an acceptable job of segregating Blanco 1 members from cluster non-members in the SPOCS CMD (see Fig. 3.13), our $\tau^2$ results for this one catalog is sufficient for determine reliable best-fit CMD isochrones. Plotted in Fig. 3.14 are the results from this analysis of the Blanco 1 proper motion members. In general, the Blanco 1 CMD is best modeled by an isochrone of ∼100-140 Myr with a DM of ∼6.8-6.9. Taking the weighted mean for each color separately, we derive an error-weighted average age and DM of 129±18 Myr and 6.85±0.02 mag (234±2 pc) for the V, $V-I_C$ CMD, and an age and distance of 121±20 Myr and 6.90±0.01 mag (240±1 pc) using the V, $B-V$ CMD. The quoted errors for these ages and DM are the uncertainties in the mean, and do not take into account likely systmeatic uncertaintes. This is particullarly true for the calculated distances, where the actual uncertainties are ∼10 parsecs (see below).

Here, we would like to highlight some of our results from our PMS modeling of Blanco 1. First, formally we do not see any model- or color-dependent, statistically significant offsets in the derived isochronal ages; although, the D'Antona & Mazzitelli models seem to preferentially predict younger ages for both $B-V$ and $V-I_c$ CMDs. We note that in the optical, the difference between between the location of a 100 Myr and 130 Myr isochrone is negligible for stars in the color ranges of our $V-I_c$ and $B-V$ CMDs, thus with typical photometric uncertainties ($\sim$0.05-0.1 mag) it is very difficult to find a precise age from an older cluster sequence, like Blanco 1. We see the effect of this in our relatively large age absolute uncertainties for our Blanco 1 age ($\pm$20 Myr) compared to our results for the younger IC 4665 ($\pm$10 Myr), even though our percent uncertainties are similar. Nevertheless, any offsets we see in the ages predicted by the different models and/or colors should be used with caution. Secondly, all three models predict approximately the same distance moduli for $V-I_c$ and $B-V$ CMDs, separately. There does appear to be a strong color-dependence in the distance moduli, where the best-fit isochrones for the $V-I_c$ CMD predict a systematically closer ($\sim$6 parsecs) distance for Blanco 1. This offset is formally beyond $3\sigma$ of the measured weighted mean distance modulus; however, the bolometric corrections, used to transform the models' effective temperatures, and luminosities into absolute magnitudes, are known to have systematic errors on the order of $\sim$0.1 magnitudes due to intrinsic scatter in their calibration (Flower, 1996). This magnitude of uncertainty can account for the color discrepancy seen in DM.

### 3.4.6 Upper-Main-Sequence turn-off Age

In order to further explore the age of Blanco 1, we also use $\tau^2$ modeling to derive an isochrone age and distance to the cluster's upper-main-sequence turn-off. Our SPOCS data have a brightness limit of V$\sim$10.5, we therefore supplement our membership catalog with proper motion members from the Westerlund et al. (1988) high-mass study of Blanco 1. This extends our catalog to V$\sim$7 for the brightest cluster member, or an early-B spectral-type at the approximate distance of Blanco 1. This gives a larger population of high-mass stars that are evolving off the main-sequence, thus providing a more precise $\tau^2$ age estimate.

Following Naylor (2009), we use upper-main-sequence models from Lejeune & Schaerer (2001) and Girardi et al. (2002), coupled with solar-metallicity bolometric corrections and effective temperature to color conversions, and color dependent reddening vectors from Bessell et al. (1998). For the two sets of models used, we find the best-fit upper-main-sequence ages and intrinsic distance moduli to be $115^{+5}_{-26}$ Myr, 7.07$\pm$0.01 mag (259$\pm$1 pc) and $115^{+6}_{-15}$ Myr, 7.12$\pm$0.02 mag (265$\pm$3 pc), respectively. In Fig. 3.15, we plot the best-fitting isochrones for the upper-main-sequence of Blanco 1. Note that the very small uncertainties in the distances are an internal error budget. In addition, these values also have an external error due to the systematic uncertainty in the bolometric correction resulting in errors of $\sim \pm 10$ parsecs, most likely representative of our actual measurement accuracy.

Comparing the upper-main-sequence ages of Blanco 1 to our measured PMS

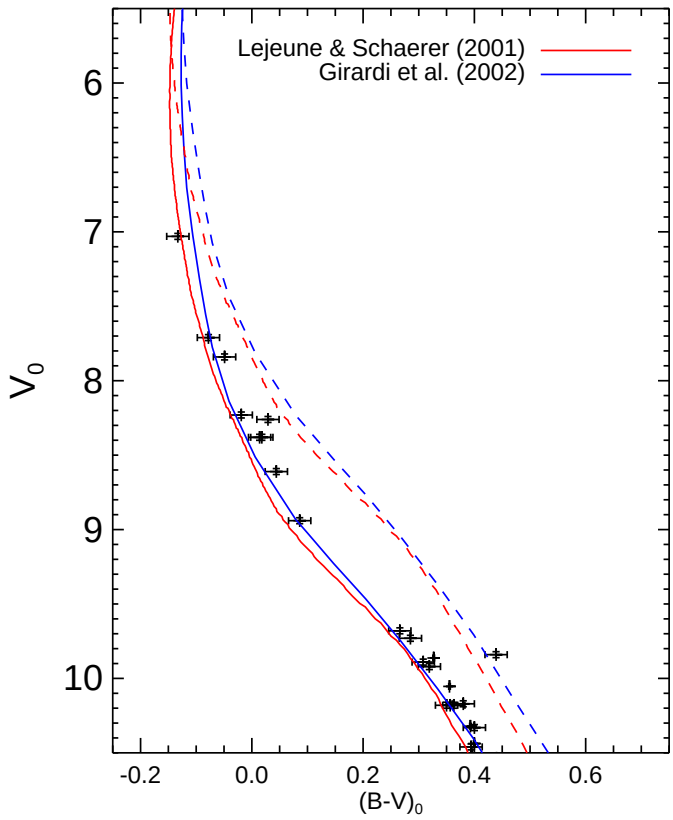


Figure 3.15: High-mass (V<11 mag) color-magnitude diagram for members of Blanco 1 using photometric data from Westerlund et al. (1988). Also plotted are the best-fit isochrones (solid lines) from our upper-main-sequence $\tau^2$-modeling using the two high-mass stellar models detailed in the legend, and their associated equal-mass binary sequences (dotted lines).

isochrone ages, we find that the two sets of ages are formally in agreement within $1\sigma$. However, the large uncertainties in the PMS ages hinders any detailed comparison between the two different age measurements. We therefore cannot confirm or rule out offsets predicted to be in these isochrone ages (*e.g.,* see Naylor, 2009).

We also compared our upper-main-sequence turn-off age of Blanco 1 to the typically assumed coeval Pleiades open clusters. Recently, Naylor (2009), using a similar

$\tau^2$ modeling technique, found an upper-main-sequence age of $115^{+2}_{-11}$ Myr for the Pleiades. The Blanco 1 upper-main-sequence age is strikingly similar, although with slightly larger error bars, thus providing further evidence that these two clusters are very similar in age.

# Chapter IV

## MAGNETIC ACTIVITY AND AGE OF YOUNG STARS

(Published as: Cargile et al. 2009 ; Cargile & James 2010 *submitted*)

Starting with the ground-braking magnetohydrodynamic work by E. N. Parker in 1950-1970 (see Chapter I), over the last half-century a general theoretical picture for the physical mechanism behind the causal relationship between magnetic activity and rotation has developed – the activity-rotation-age paradigm (ARAP). With the advent of space-based X-ray telescopes, particularly with the deployment of the Einstein Observatory in the early 1980s, we began to place empirical constraints on the evolution of magnetic activity based on measurements of X-ray flux from stellar coronae. Achievements include observations showing that young solar-analogs have X-ray emission several orders of magnitude higher than the Sun, and that X-ray activity declines with age as stars are magnetically braked and lose their initial angular momentum. More recently, modern X-ray telescopes, *i.e.,* ROSAT , Chandra, and XMM-Newton Observatories, have provided observational data confirming much of the ARAP; however, there remains various unresolved details of X-ray emission evolution in stars, such as the origin of the X-ray saturation phenomenon (see Chapter I).

In this chapter, we investigate the ARAP employing empirical data for the open

cluster Blanco 1. First, we present our new analysis of the X-ray properties of Blanco 1 (Cargile et al., 2009). This part of the chapter is a reproduction of our published manuscript in the *Astronomical Journal*, excluding a discussion on the SPOCS photometry that we extensively covered in Chapter III.

We then include an Epilogue to our published work, reporting more recent analysis on the X-ray properties of Blanco 1 stars. That is to say, employing new measurements for rotation rates of Blanco 1 stars, we revisit the morphology of X-ray emission seen in Blanco 1 in the broader context of the ARAP; we perform a comparative analysis of our Blanco 1 results to a new analysis of the young open cluster IC 4665; and finally, briefly suggest possible avenues to empirically calibrate the activity-age relationship in order to provide a relative estimate of open clusters ages directly from their X-ray emission distributions. This epilogue includes work that is not yet published but has been submitted for publication (Cargile & James; submitted).

## 4.1 X-ray Properties of Blanco 1

(Published as Cargile et al. 2009)

Blanco 1 (see Chapter 3.4 for full description of cluster) contains more than 200 known members spread over $\simeq 3 \times 3$ degrees$^2$ on the sky (Jeffries & James, 1999; James et al., 2010; Mermilliod et al., 2008; Moraux et al., 2007). Such a wide areal on-sky distribution is challenging for deep and complete photometric surveys. The existing X-ray studies of Blanco 1 (Micela et al., 1999a; Pillitteri et al., 2004) have relied on

older, photographic photometry (de Epstein & Epstein, 1985) to segregate cluster members from Galactic field stars and background galaxies. Due to the inherent scatter in this photographic photometry, especially in the photometric precision of fainter objects (see Chapter III), definitive membership status and characteristics of optical counterparts to X-ray sources remain poorly established.

### 4.1.1 X-ray Observations: ROSAT

Micela et al. (1999a, hereafter M99) report the results of two deep exposure ($\sim$70 ksec) ROSAT HRI pointings, bore-sighted on the central region of Blanco 1. The two adjacent $40' \times 40'$ pointings were centered at R.A.(2000): $00^h02\overset{m}{.}8$; Dec.(2000): $-30°00'$ (field 1) and R.A.(2000): $00^h05\overset{m}{.}6$; Dec.(2000): $-30°06'$ (field 2). Identification of X-ray sources detected in these pointings were based upon a point spread function (PSF) detection algorithm, with a source acceptance threshold chosen such that there is no more than one predicted false source detection per HRI image. This procedure yielded a total of 132 X-ray sources from both fields in the 0.1 to 2.4 keV energy band. M99 utilize an X-ray error circle of $20''$ for significantly-detected sources. In order to derive fluxes for their HRI X-ray sources, M99 derives a count rate to flux conversion factor of $3.2 \times 10^{-11}$ erg cm$^{-2}$ cnt$^{-1}$ assuming a single temperature Raymond-Smith model for an optically-thin plasma with a temperature of 1 keV and a hydrogen column density of $\log(N_H) = 20$.

In order to verify that their identified X-ray sources are correlated with Blanco 1

cluster members, M99 employed the de Epstein & Epstein (1985) photometric membership list. They find 42 X-ray sources with optical counterparts, lying in X-ray positional errors circles, as well as having de Epstein & Epstein (1985) optical photometry consistent with being associated with the apparent Blanco 1 cluster main sequence. They additionally determine 41 X-ray flux upper limits for other likely cluster members, adjudged from de Epstein & Epstein photometry. However, the fidelity of the de Epstein & Epstein photographic photometry is questionable (see Chapter 3.4). The systematic scatter in their suspect photometry *must* act to introduce uncertainties into a photometric membership criterion, and thus, such optical/X-ray associations might include several spurious/suspect assignments of X-ray activity to stars whose cluster membership is uncertain.

### 4.1.2 X-ray Observations: XMM-Newton

Pillitteri et al. (2004, hereafter P04) report the results arising from a deep exposure (50 ksec) XMM-Newton pointing of Blanco 1, centered on the coordinates of the field 1 pointing detailed in the M99 study. The observations were obtained with the EPIC camera system, which has a field-of-view of $30' \times 30'$. P04 used a PSF detection algorithm for source searching, which yielded a total of 190 X-ray sources detected in the 0.3 to 5.0 keV band. For XMM-Newton , Jansen et al. (2001) states that the absolute location accuracy for the EPIC instrument XMM-Newton is uncertain up to $4''$. Furthermore, P04 finds the internal precision for the EPIC camera to be $2\farcs3$ for

the Blanco 1 field, thus giving a total positional uncertainty of 6.″3. Mirroring the M99 study, P04 set a source detection threshold such that no more than one spurious detection was predicted, with a key difference being that a positional error radius of 13″ for X-ray sources was used. P04 computed count rate to flux conversion factors for the 23 brightest X-ray sources from a detailed low-resolution spectral analysis using a grid of 2-temperature component models with photoelectric absorption values taken from the APEC abundance database. The spectra were found to be best modeled by a lower temperature component of 0.33 keV, an upper temperature component that varied typically from 0.8 to 1.5 keV, and a hydrogen column density of $\log(N_H) = 20.5$. The count rate to flux conversions factors for these 23 stars were then averaged to get an overall conversion factor of $5.69 \times 10^{-12}$ erg cm$^{-2}$ cnt$^{-1}$ for the full XMM-Newton X-ray dataset.

P04 establishes cluster membership for Blanco 1 based on a Pillitteri et al. (2003) photometric and proper motion study. This earlier study uses a photometric selection based upon an $R$ vs. $B - R$ CMD, obtained from the second generation of the Guide Star Catalog (GSC-II) photometric data. Their analysis used a somewhat *ad-hoc* by-eye selection, based on a region a few magnitudes wide around an assumed main sequence locus. They further refine their selection process by excluding photometric members with USNO-B1 proper motion membership probabilities $p \leq 0.8$. This methodology miss targets because proper motion membership probabilities can be highly dependent upon stellar magnitudes.

Armed with these membership constraints, P04 selected 93 stars as likely members of Blanco 1. Approximately 40% of these stars (36/93) are optical counterparts to XMM-Newton X-ray sources, including 8 previously noted as non-members by the M99 study. Of the remaining 154 X-ray sources that were not determined as being Blanco 1 cluster members, 90 sources were found to have optical counterparts detailed in either the USNO-B1, GSC-II, or 2MASS catalogs. The remaining 64 (*i.e.,* 154 total - 90 matched sources) X-ray source detections could not be matched with optical counterparts. They are thus likely to be extra-Galactic background objects, which is hardly surprising given that Blanco 1 lies at high Galactic latitude ($b = -79°$). In investigating the optical/X-ray relationships for Blanco 1, P04 used de Epstein & Epstein $B - V$ for stars also found in the M99 study. As for the rest of the X-ray sources, they used the $B - V$ colors converted from the GSC-II $B - R$ colors. Using these calculated $B-V$ colors, which contain significant systematic photometric error, introduces uncertainty in the optical/X-ray correlated data analyzed in the P04 paper.

### 4.1.3 Revised X-ray Cluster Membership

In order to refine the membership selection of the X-ray sources, we incorporate the X-ray data from M99 and P04 with our new $BVI_c$ photometry and proper motions. We employ the method outlined in Jeffries et al. (1997) to determine the proper search radius for identifying optical counterparts in our SPOCS dataset (see Chapter 3.4) optical catalog to the M99 ROSAT and P04 XMM-Newton datasets. The procedure

estimates the number of real versus spurious matches one should expect in a cross-correlation of an X-ray and optical catalog. This involves modeling the cumulative distribution of the closest match separations for the X-ray sources as the sum of two terms; the cumulative distribution of true correlations and the cumulative number of spurious sources, which will increase with separation. For the ROSAT dataset, we determine that a search radius of 16″, which statistically should have ∼2/52 false counterpart matches, optimizes the number of counterpart matches while minimizing the expected spurious matches. The standard deviation of offsets for matched sources and optical counterparts for a 16″ search radius is 4.″04. In a similar fashion, we analyze the XMM-Newton X-ray source matched with the SPOCS optical catalog. Our analysis showed that a search radius of 6″ would maximize the number of matches while decreasing the expected spurious matches to ∼1/35. We find that the standard deviation of offsets for our XMM-Newton matches is 1.″38.

Using the search radii listed above (16″ for ROSAT and 6″ for XMM-Newton ), we matched optical counterparts in the SPOCS catalog to the X-ray sources published in the surveys of M99 and P04. The results of this matching are given in Appendix B. To summarize our findings, in Fig. 4.1(a) we plot the SPOCS optical catalog with the 52 ROSAT and 35 XMM-Newton X-ray sources with optical counterparts identified. Considering only those objects with proper motions consistent with the Blanco 1 membership, we find 41 X-ray sources that were previously identified as members of Blanco 1 by M99 and/or P04, including 24 stars observed by both telescopes.

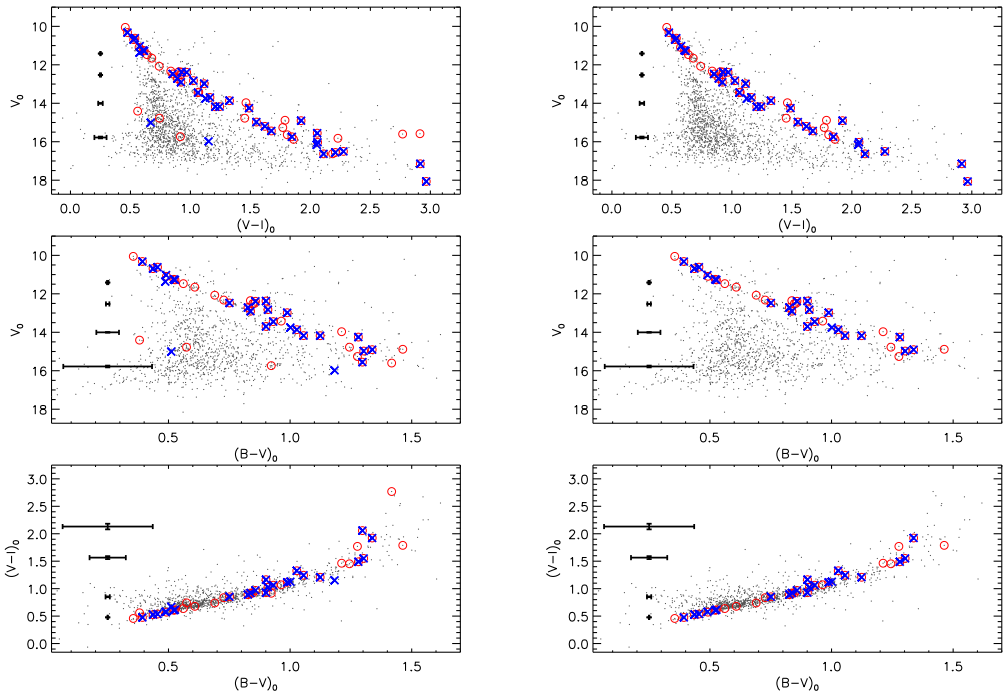


(a) X-ray Members

(b) X-ray and Proper Motion Members

Figure 4.1: Intrinsic color-magnitude and color-color diagrams for the full SPOCS photometric catalog are plotted. An $E(B-V) = 0.016$ and $E(V-I_c) = 0.02$ have been used. We identify the optical counterparts to X-ray sources from ROSAT (*red open circles*) and XMM-Newton (*blue crosses*). For Fig. 4.1(b), only those objects are included that have proper motions consistent with the systemic proper motion of the cluster.

Interestingly, our new CCD photometry and proper motion surveys have allowed us to identify an additional 6 X-ray sources that were incorrectly classified as non-members in the preceding X-ray surveys. Furthermore, based on the new proper motions, we reject 3 X-ray sources that M99 and P04 previously had identified as cluster members. These objects are likely active field stars or background active galaxies. The fact that these sources might be active galaxies is further supported by Richards et al. (2002)

Table IV.1. Multiple X-ray Detection to Single Optical Counterparts in Blanco 1

| ROSAT | | | XMM-Newton | | | Optical Counterpart | |
|---|---|---|---|---|---|---|---|
| ID | R.A. | Dec. | ID | R.A. | Dec. | R.A. | Dec. |
| ZS44 | 0:02:14.5 | -29:48:58.6 | PMS04-182 | 00:02:14.6 | -29:49:03.5 | 00:02:14.65 | -29:49:04.41 |
| ZS60 | 0:02:41.8 | -29:58:53.7 | PMS04-97 | 00:02:41.7 | -29:58:55.8 | 00:02:41.73 | -29:58:53.19 |
| BLX-12 | 0:02:07.2 | -30:04:41.8 | PMS04-48 | 00:02:07.6 | -30:04:44.4 | 00:02:07.65 | -30:04:42.90 |
| BLX-15 | 0:02:22.3 | -30:02:52.0 | PMS04-66 | 00:02:22.7 | -30:02:52.3 | 00:02:22.87 | -30:02:52.88 |
| BLX-16 | 0:02:23.1 | -29:50:34.5 | PMS04-169 | 00:02:23.4 | -29:50:40.4 | 00:02:23.58 | -29:50:39.99 |
| BLX-42 | 0:03:22.3 | -29:53:49.4 | PMS04-150 | 00:03:22.6 | -29:53:52.2 | 00:03:22.73 | -29:53:50.89 |

Note. — Coordinates are J2000.0 Equinox.

who find that AGN in the SDSS database, with a wide range of red shifts, are clearly found with approximate colors $0.0 < B-V < 1.25$ and $0.0 < V-I_c < 1.5$ (using SDSS filter to UBVI$_c$ conversions of Smith et al. 2002). The unidentified sources in our X-ray dataset have optical counterparts with colors that fall directly within these AGN color ranges. In Fig. 4.1(b), we plot a CMD marking only those X-ray sources that we have determined through proper motions to be cluster members. This demonstrates the power of precision photometric and proper motion data in defining a high fidelity cluster membership catalog.

Of the total 47 X-ray sources we identify as being associated with cluster members, 26 have optical counterparts that are included in spectroscopic surveys of Blanco 1 (Jeffries & James, 1999; Mermilliod et al., 2008). These surveys identified all 26 stars as having radial velocities consistent with cluster membership, thus verifying the fidelity of our proper motion membership selection.

Moreover, we note that six optical counterparts in the SPOCS catalog are associated

with two separate X-ray sources in M99 and P04. It appears that the XMM-Newton sources that P04 identified as Blanco 1 non-members were not matched with the M99 ROSAT X-ray dataset. Using the new proper motions, we subsequently find that three of these six stars are, in fact, cluster members (ZS44, BLX-16, BLX-42), while two (BLX-12 and BLX-15) fell below our proper motion survey's faintness limit. In Table IV.1, we list all six sources from M99 and P04 along with the single optical counterparts from the SPOCS catalog. To be clear, each pair of XMM-Newton and ROSAT X-ray detections listed in Table IV.1 is associated with a single optical counterpart. M99 and P04, however, have identified the XMM-Newton and ROSAT sources as two separate X-ray sources. Apparently this is not the case.

### 4.1.4 X-ray Luminosity and $L_x/L_{bol}$ Ratio for Blanco 1 Members

For cluster members that are optical counterparts to X-ray sources in Blanco 1, we derive their X-ray fluxes and luminosities using the published ROSAT and XMM-Newton X-ray count rates listed in M99 and P04. We convert count rates to fluxes applying the available conversion factors, $3.2 \times 10^{-11}$ erg cm$^{-2}$ cnt$^{-1}$ for ROSAT and $5.69 \times 10^{-12}$ erg cm$^{-2}$ cnt$^{-1}$ for XMM-Newton, and derived luminosities using a distance derived in Chapter III from our best-fitting $B - V$ PMS isochrones, 240 pc. We propagate the uncertainties in flux from the published errors in the count rates. In the conversion from flux uncertainties to errors in X-ray luminosities, we use the distance error given in Chapter III. For a selection of ROSAT X-ray sources that did

not have published uncertainties (see Table 2 in M99), we calculate their count rate errors using a linear interpolation of stars having both count rates and uncertainties in the M99 ROSAT survey.

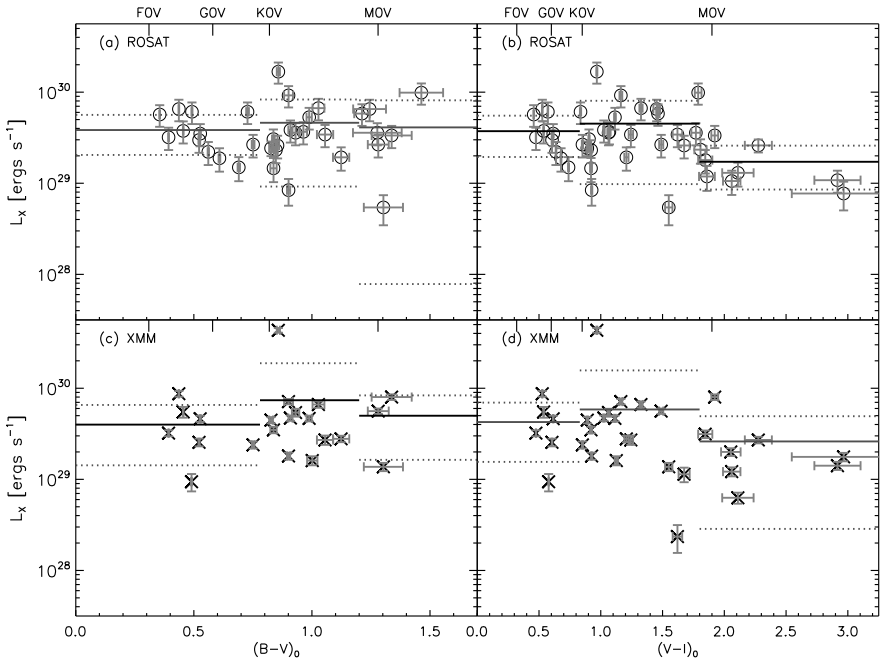


Figure 4.2: X-ray luminosity from ROSAT (*open circles*) and XMM-Newton (*crosses*) as a function of intrinsic $B-V$ and $V-I$ for Blanco 1 cluster members. The solid lines indicate the mean $L_X$ for F & G, K, and M stars, where dotted lines represent $1\sigma$ values about these means for each given spectral types.

In Fig. 4.2, we show X-ray luminosity versus intrinsic $B-V$ and $V-I_c$ colors for both ROSAT and XMM-Newton Blanco 1 X-ray sources. We calculate intrinsic colors using $E(B-V) = 0.016$ and $E(V-I) = 0.02$ (see Chapter III). Also plotted, and included in Table IV.2, are the mean X-ray luminosity and their $1\sigma$ dispersions found for different spectral type bins. These spectral bins are determined from color

Table IV.2. Mean values of $L_x$ for Blanco 1 Members

| Spectral Range[a] | Mean $Log(L_x)$ [erg s$^{-1}$] | $1\sigma$ [erg s$^{-1}$] |
|---|---|---|
| ROSAT – $B-V$ | | |
| G and Earlier | 29.52 | 0.21 |
| K | 29.66 | 0.30 |
| M and Later | 29.61 | 0.52 |
| ROSAT – $V-I_c$ | | |
| G and Earlier | 29.57 | 0.22 |
| K | 29.65 | 0.33 |
| M and Later | 29.23 | 0.21 |
| XMM-Newton – $B-V$ | | |
| G and Earlier | 29.60 | 0.31 |
| K | 29.86 | 0.37 |
| M and Later | 29.69 | 0.40 |
| XMM-Newton – $V-I_c$ | | |
| G and Earlier | 29.62 | 0.33 |
| K | 29.76 | 0.47 |
| M and Later | 29.41 | 0.33 |

[a]Spectral ranges are defined by Kenyon & Hartmann (1995): G-type and Earlier $B-V_0 < 0.8$, K-type $0.8 < B-V_0 < 1.3$, M-type and later $B-V_0 > 1.3$

Note. — X-ray luminosities were measured over the energy ranges of 0.1-2.4 keV and 0.3-5.0 keV for ROSAT and XMM-Newton, respectively.

to spectral type conversions defined in Kenyon & Hartmann (1995). Within the observed dispersion levels, the mean $L_x$ as a function of spectral type in the late F to early M star regime is constant. However, there is some evidence for a drop in X-ray luminosity, particularly for XMM-Newton sources and in the $V - I_c$ domain where lower mass stars are better represented over a wider color range. Empirically, observations of several open clusters support this conclusion (for instance, see Section 4.2.2 and references therein).

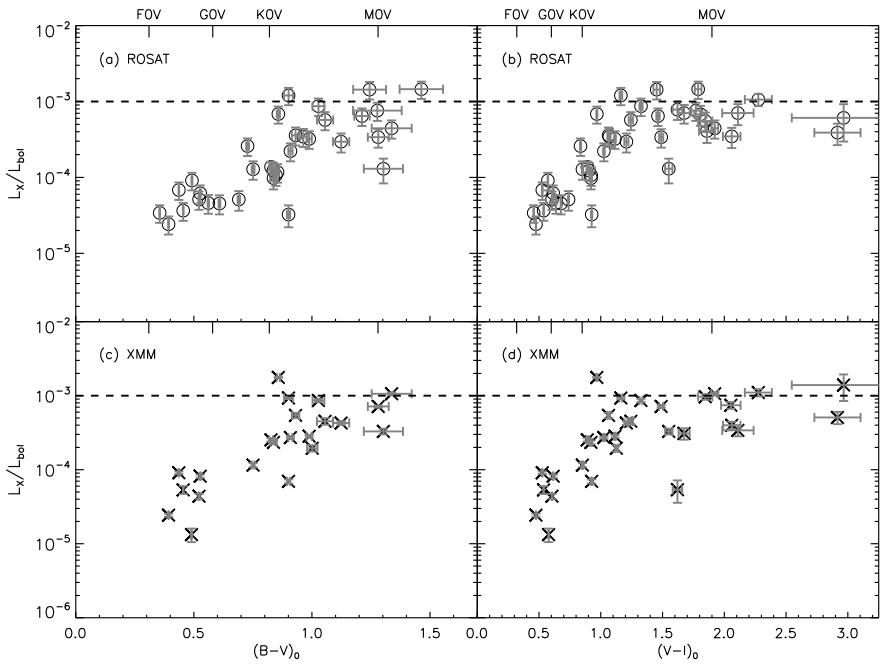


Figure 4.3: Ratio of X-ray to bolometric luminosity plotted as a function of intrinsic color for ROSAT (*open circles*) and XMM-Newton (*crosses*) sources in Blanco 1. The dashed line marks the level at which X-ray luminosity reaches 0.1 % of the bolometric luminosity, which is canonically known as X-ray saturation (*e.g.,* Stauffer et al., 1994).

We plot in Fig. 4.3 the distance-independent ratio of X-ray to bolometric luminosity as a function of intrinsic $B-V$ and $V-I_c$ colors for Blanco 1 stars having X-ray detections. We note that in Fig. 4.3, as well as in Fig. 4.2, the $V-I_c$ color should be preferred for the reddest stars because for values greater than $\sim$1.4, $B-V$ becomes almost insensitive to changes in stellar mass. In our calculation of the bolometric luminosities, we use the bolometric corrections listed in Johnson (1966) for stars with $V-I<1.6$ and the formalism given in Monet et al. (1992) for stars with $V-I>1.6$. A clear increase in $L_x/L_{bol}$ is observed as one goes from F–G to mid-K spectral types in Blanco 1. For spectral types later than K5, at $V-I\approx1.25$ there is a saturation limit at a $L_x/L_{bol}$ of $10^{-3}$, where the X-ray production becomes insensitive to changes in spectral type. The exact cause of this limit has yet to be determined; however, several theories have been put forth, including limitations on the field generation capacity of the stellar dynamo (Gilman, 1983; Vilhu & Walter, 1987) and/or due to centrifugal forces on magnetic loops in rapidly rotating stars (Jardine & Unruh, 1999; James et al., 2000).

### 4.1.5 Short-Term X-ray Variability: Flaring and Saturation

Previous X-ray studies, M99 and Pillitteri et al. (2005), have provided in depth investigations of short-term X-ray variability in Blanco 1, therefore here we merely provide a summary of those findings. M99 identified 4 variable X-ray sources in their ROSAT dataset (ZS38, ZS61, ZS75, ZS76). We identify all 4 of these objects

as proper motion members of Blanco 1. In a follow up variability study of the P04 XMM-Newton dataset, Pillitteri et al. (2005) found 22 variable X-ray sources. For 9 of these 22 sources, we find optical counterparts in the SPOCS optical catalog, and we identify them as proper motion members of Blanco 1 (ZS45, ZS46, ZS61, ZS75, ZS76, ZS94, ZS95, and BLX-42).

It has been suggested that X-ray flaring in stellar coronae has a causal relationship to X-ray emission saturation. We find 3 of the 4 ROSAT sources and 4 of 9 XMM-Newton sources characterized as having short-term variability in M99 or Pillitteri et al. (2005) have saturated levels of X-ray emission, where saturation is arbitrarily defined as $L_x/L_{bol}$ above $10^{-3.25}$. We also identify 9 ROSAT and/or XMM-Newton sources that have saturated X-ray emission levels (ZS35, ZS37, ZS40, ZS42, ZS43, ZS53, ZS71, ZS88 and, ZS115) but were not identified by M99 and/or Pillitteri et al. (2005) as having significant X-ray variability. Assuming that the X-ray variability observed is evidence for flaring events, these statistics – the large number of non-variable saturated sources compared to the small number of variable saturated sources – do not suggest that there is an intrinsic correlation between X-ray flaring and saturated X-ray emission levels.

#### 4.1.6 Long-Term X-ray Variability: Comparison of ROSAT and XMM-Newton Data

We cross-correlated the source positions listed in both surveys with a match radius of up to 16″, as derived by the positional uncertainties in the ROSAT data. This search

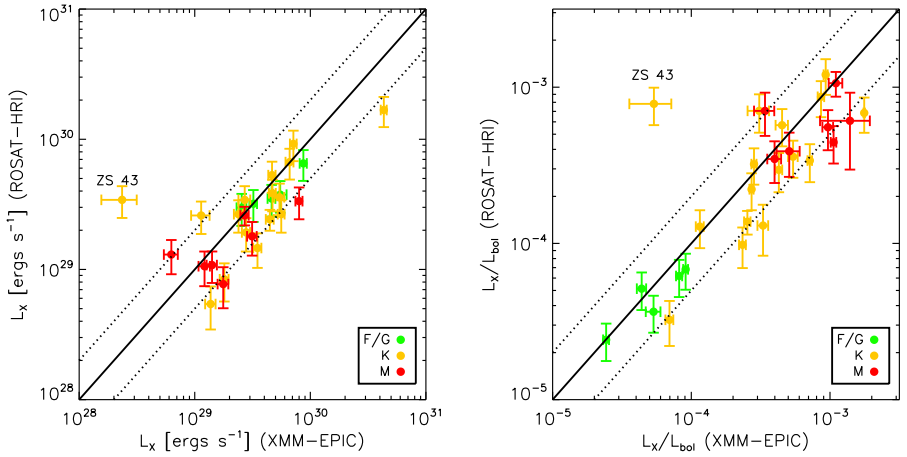


Figure 4.4: Comparison of X-ray luminosity (*left*) and X-ray to bolometric luminosity (*right*) for the 28 cluster members observed with both ROSAT and XMM-Newton , separated by ∼6 yr. The *solid* lines marks equality between measurements, whereas variations by factors of 0.5 and 2.0 (*dotted lines*) are also shown. We also color-code these stars according to the different spectral ranges as defined by the colors given in Kenyon & Hartmann (1995). One star (ZS43), that shows significant discordancy between the measurement systems, is identified.

yields 28 matches for photometrically determined cluster members. For matched sources, we plot in Figs. 4.4 the X-ray luminosity and the $L_x/L_{bol}$ values for both surveys along with lines representing equality and variations by factors of 0.5 and 2.

First, we note that the lack of any statistically significant systematic offset between the ROSAT and XMM-Newton X-ray luminosities and $L_x/L_{bol}$ values suggest that, even though the two datasets were observed over different energy bands, the conversion factors used to convert counts to X-ray fluxes were modeled correctly by M99 and P04. The reason for this agreement in X-ray flux over the two different energy bands is primarily due to the fact that the peak intensity of X-rays from Sun-like stars is around 1 keV, so that few photons are likely to fall in non-overlapping energies (Güdel,

2004). Furthermore, this agreement provides assurance that our following analysis of X-ray emission from Blanco 1 stars does not suffer from instrumental systematics in the two X-ray datasets.

In order to investigate any possible long-term X-ray variability in Blanco 1, we look at the cluster members with X-ray sources in both ROSAT and XMM-Newton surveys. A time-span of ∼6 years separates these two surveys. These results suggest that the majority of the Blanco 1 cluster members have not undergone significant long-term X-ray variability. The source ZS43 shows a change in X-ray flux greater than a factor of 2, which is very likely due to the source confusion (see below). The apparent lack of long-term X-ray variability in Blanco 1 F-M dwarfs is in agreement with the ROSAT and XMM-Newton $L_x$ comparison made in Pillitteri et al. (2005), as well as variability studies in other open clusters (*e.g.,* the Pleiades Marino et al., 2003). We note that for ZS76, a known X-ray flaring star (Pillitteri et al., 2005), we have adopted the count-rate of the star during its quiescent state.

As stated above, the ROSAT X-ray flux measurement of ZS43 is significantly different than that of the XMM-Newton measurements. This discrepancy is clearly seen in Fig. 4.4. A close inspection of the field near ZS43 reveals that another X-ray source, ZS42, lies only 11.″6 away. The close proximity of these sources may lead to near-neighbor source confusion in the X-ray data, and therefore cause two systematic offsets in the ROSAT and XMM-Newton X-ray fluxes for ZS43. First, due to the large PSF of the ROSAT telescope (>16″), the counts for ZS43 in M99 likely includes flux

from ZS42, and therefore the ROSAT X-ray flux would be overestimated. Second, the XMM-Newton PSF is smaller than ROSAT and therefore the background level likely includes counts from ZS42 causing the XMM-Newton X-ray flux to be underestimated. A combination of these two effects could explain the observed offset to the top left of this data point in Fig. 4.4.

## 4.2 X-Ray Production in Blanco 1

### 4.2.1 X-ray Activity Along the Main Sequence

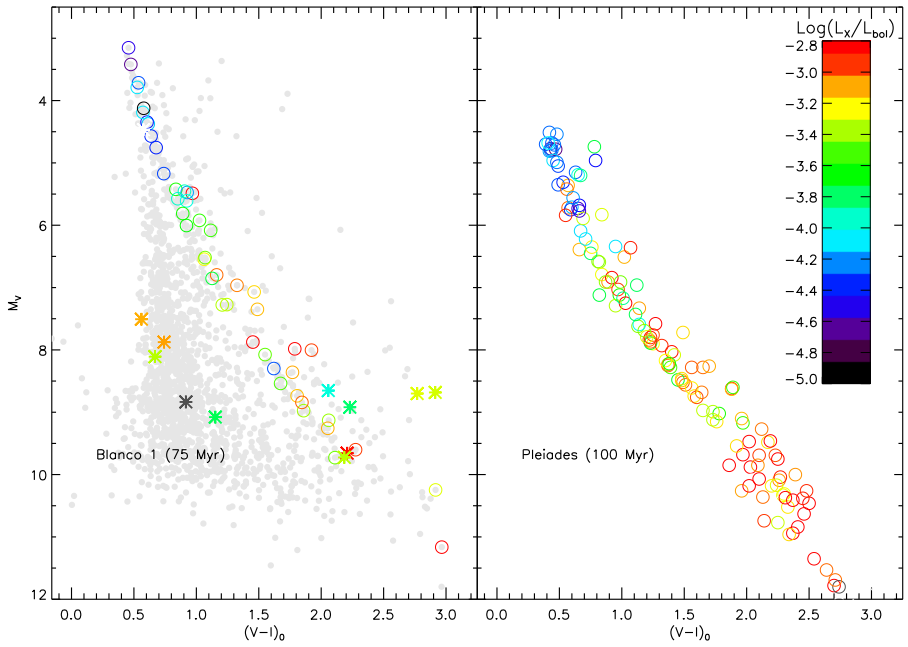


Figure 4.5: Comparison of CMD is shown for Blanco 1 *(left)* and Pleiades *(right)* open clusters, with optical counterparts to X-ray sources identified. The magnitude of the ratio of X-ray to bolometric luminosity, given by the color coding, is shown on the right-hand panel. To derive the absolute magnitude for the two clusters we use 240 (see Chapter III) and 133 (Soderblom et al., 2005) parsecs for Blanco 1 and the Pleiades, respectively. For the Blanco 1 cluster, non-members are noted with asterisks, and the full photometric catalog is shown in gray.

In the left panel of Fig. 4.5, the $M_V$, $V-I$ CMD for Blanco 1 is displayed showing the identified optical counterparts to X-ray sources and color-coded according to their magnitude of $L_x/L_{bol}$. We use the distance from Chapter III (240 parsecs) to derive the absolute magnitudes for the stars in Blanco 1. We find X-ray counterparts to 47 optically-identified cluster members extending from early-F to mid-M spectral types. In Blanco 1, a general trend of increasing $L_x/L_{bol}$ with decreasing mass is seen along the main sequence. Although the PSF of ROSAT and XMM-Newton does not allow us to resolve individual stars in known binary systems in Blanco 1, we do observe that photometric binaries (stars having colors and magnitude above the single-star main sequence) of a given mass appear to be more X-ray luminous than their single star counterparts lying on the main sequence. This phenomenon is not unique to Blanco 1, with observations showing that binaries are typically over-luminous in X-rays when compared to single stars (*e.g.,* Pye et al., 1994; Stern et al., 1995; Makarov, 2002).

### 4.2.2 Activity-Age Relationship

It is known that there exist a strong causal relationship between X-ray emission and rotation rate in solar-type stars (Pallavicini et al., 1981; Stauffer et al., 1994). The underlying cause of this phenomenon can be understood in terms of greater dynamo-induced magnetic field production with increasing rotation rate (Wilson, 1966; Kraft, 1967). There is, however, an age effect to be considered. This is because, as solar-type stars age on the main sequence, they are capable of losing angular momentum

through a magnetically channeled stellar wind (e.g. Weber & Davis, 1967; Mestel, 1968; Kawaler, 1988; Barnes, 2003). Therefore, as stars become older their surface rotation rate decreases, resulting in an associated reduction in dynamo-induced magnetic field production. This is the so-called age-rotation-activity paradigm. This generalized scenario is observed in young open clusters and field stars as decay of magnetic activity and rotation in solar-type stars proportionally to inverse square root of their age ($t$) (Skumanich, 1972).

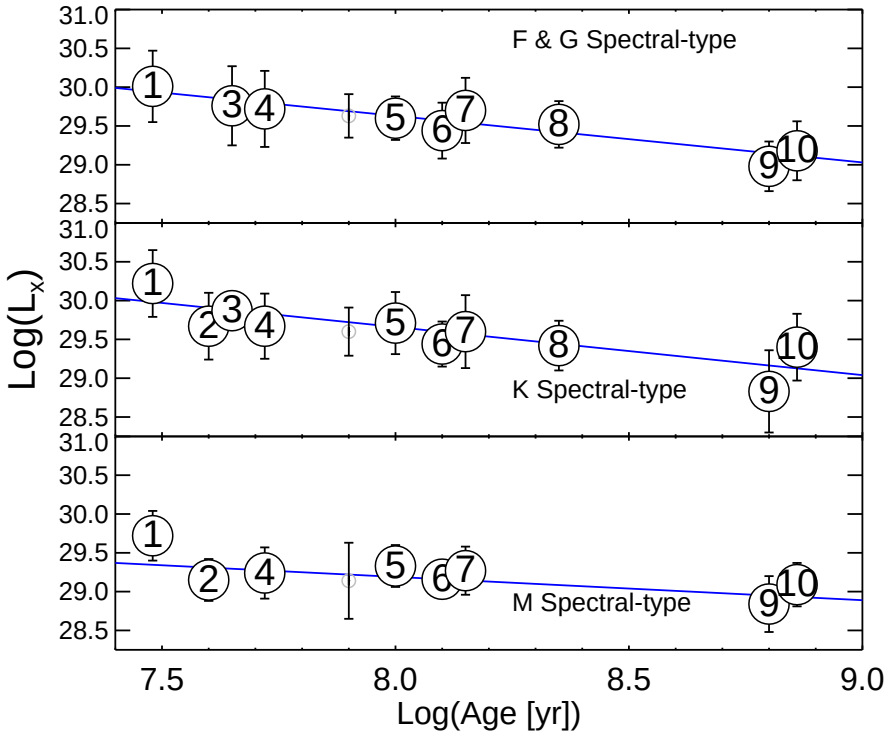


Figure 4.6: Evolution of $L_x$ as a function of age is shown for the various open clusters detailed in Table IV.3, including our new Blanco 1 measurements (*5*) as well as those derived by P04 *(light-font, open circle)*. The data from P04 is shifted to a younger age in order to compare with new results. Reference numbers (1-10) from Table IV.3 are shown for each data point. Error bars represent the $1\sigma$ scatter for the given spectral ranges for each cluster. The blue lines indicate linear, least-squares fits to the cluster data.

Table IV.3: Measured $L_x$ for Several Open Clusters

| Name | Reference Number[b] | *Log*(Age) [yr] | F & G Spectral-Type[a] # of Stars Included | F & G Spectral-Type[a] Mean $Log(L_x)$ | K Spectral-Type[a] # of Stars Included | K Spectral-Type[a] Mean $Log(L_x)$ | M Spectral-Type[a] # of Stars Included | M Spectral-Type[a] Mean $Log(L_x)$ |
|---|---|---|---|---|---|---|---|---|
| NGC 2547 | 1 | 7.48 | 22 | 29.71±0.46 | 23 | 29.92±0.37 | 52 | 29.42±0.32 |
| IC 2602 | 2 | 7.60 | 9 | ··· | 16 | 29.67±0.43 | 27 | 29.15±0.27 |
| IC 2391 | 3 | 7.65 | 20 | 29.76±0.51 | 13 | 29.87±0.22 | 4 | ··· |
| $\alpha$ Persei | 4 | 7.72 | 30 | 29.72±0.49 | 51 | 29.67±0.42 | 50 | 29.24±0.33 |
| Blanco 1 | 5 | 8.00 | 11 | 29.60±0.28 | 25 | 29.71±0.40 | 11 | 29.33±0.27 |
| Pleiades | 6 | 8.10 | 31 | 29.44±0.36 | 40 | 29.44±0.29 | 43 | 29.16±0.20 |
| NGC 2516 | 7 | 8.15 | 54 | 29.40±0.42 | 81 | 29.30±0.47 | 90 | 28.97±0.31 |
| M 7 | 8 | 8.35 | 47 | 29.52±0.30 | 56 | 29.42±0.32 | 4 | ··· |
| Hyades | 9 | 8.80 | 94 | 28.98±0.32 | 42 | 28.83±0.53 | 48 | 28.84±0.36 |
| Praesepe | 10 | 8.86 | 36 | 29.18±0.38 | 12 | 29.40±0.43 | 20 | 29.09±0.28 |

In an effort to understand the relationship between activity and age in open clusters, we explore the mean X-ray luminosities of Blanco 1 stars in relation to several well studied open clusters of various ages. The results of this analysis are displayed in Fig. 4.4 and in Table IV.3. Two trends in the data are apparent. First, the mean X-ray luminosity of the F/G, K, and M stars decrease as a function of age. Our linear, least-squares fits to the data give a time dependence on X-ray luminosity of

*Note*–For a given color/spectral-type bin, we did not included $L_x$ values in the linear-fit (see text) for clusters with <10 X-ray detections. For those cases we indicate their mean $L_x$ vales as "...".

[a] Spectral ranges are defined by Kenyon & Hartmann (1995): F & G Spectral-type $V - I_c < 0.8$, K-type $0.8 < V - I_c < 1.8$, M-type $V - I_c > 1.8$

[b] The letters that come after the following citations represent -X XMM-Newton[0.3-10 keV] and -R ROSAT[0.1-2.4 keV]. *References:***(1)** Cargile & James (*submitted*)-R, **(2)**Jeffries et al. 2006-X, **(3)**Randich et al. 1995-R, **(4)**Patten & Simon 1996-R,**(5)**Randich et al. 1996-R, **(6)**Cargile et al. 2009, **(7)**Stauffer et al. 1994; Micela et al. 1999b-R, **(8)**Pillitteri et al. 2006-X, **(9)**Prosser et al. 1995-R, **(10)**Stern et al. 1995-R.,Perryman et al. 1998, **(11)**Randich & Schmitt 1995-R (***N.B.:*** These reference numbers are also used in Fig. 4.6.)

$L_x \propto t^{-0.60\pm0.01}$, $t^{-0.62\pm0.27}$, $t^{-0.30\pm0.21}$ for spectral-type ranges of F/G, K, and M, respectively. This can be understood as stars having a less efficient dynamo with age because of stellar spin down. Second, the rate of decay is reduced in the M stars compared to the G and K stars in the surveyed clusters. This characteristic of the data is suggestive of longer spin down time scales for the lowest mass stars.

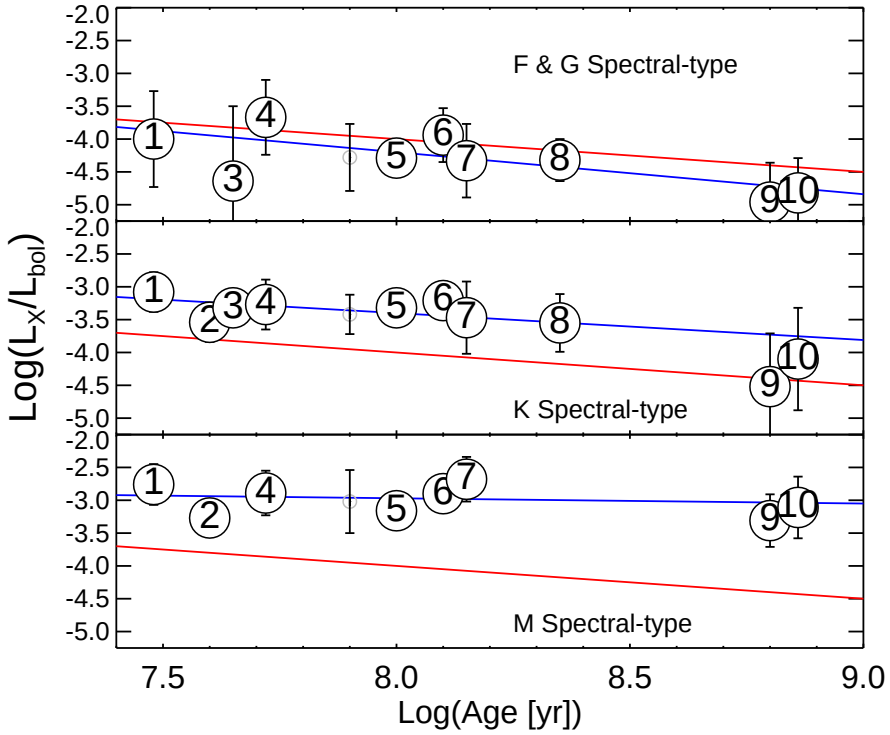


Figure 4.7: Evolution of $L_x/L_{bol}$ as a function of age is shown for the various open clusters detailed in Table IV.4, including our new Blanco 1 measurements (*5*) as well as those derived by P04 *(light-font, open circle)*. Reference numbers (1-10) from Table IV.4 are shown in the upper part of each panel. The data from P04 is shifted to a younger age in order to compare with new results. Error bars represent the $1\sigma$ scatter for the given spectral ranges for each cluster. The blue lines indicate linear, least-squares fits to the cluster data. The red lines indicate a Skumanich-like (i.e. $L_x/L_{bol} \sim Age^{-\frac{1}{2}}$) decay in X-ray emission. The initial conditions for the Skumanich functions are $L_x/L_{bol} = 10^{-3}$ at 1 Myr.

Table IV.4: Measured $L_x/L_{bol}$ Ratios for Several Open Clusters

| Name | Reference Number[b] | *Log*(Age) [yr] | F & G Spectral-Type[a] # of Stars Included | F & G Spectral-Type[a] Mean $Log(L_x/L_{bol})$ | K Spectral-Type[a] # of Stars Included | K Spectral-Type[a] Mean $Log(L_x/L_{bol})$ | M Spectral-Type[a] # of Stars Included | M Spectral-Type[a] Mean $Log(L_x/L_{bol})$ |
|---|---|---|---|---|---|---|---|---|
| NGC 2547 | 1 | 7.48 | 22 | -4.30±0.73 | 23 | -3.38±0.30 | 52 | -3.06±0.31 |
| IC 2602 | 2 | 7.55 | 9 | ··· | 16 | -3.54±0.30 | 27 | -3.27±0.29 |
| IC 2391 | 3 | 7.60 | 20 | -4.64±1.14 | 13 | -3.32±0.15 | 4 | ··· |
| $\alpha$ Persei | 4 | 7.72 | 30 | -3.67±0.57 | 51 | -3.27±0.38 | 50 | -2.89±0.34 |
| Blanco 1 | 5 | 8.00 | 11 | -4.29±0.24 | 25 | -3.32±0.24 | 11 | -3.16±0.24 |
| Pleiades | 6 | 8.10 | 31 | -3.94±0.41 | 40 | -3.21±0.29 | 43 | -2.90±0.23 |
| NGC 2516 | 7 | 8.15 | 54 | -4.63±0.56 | 81 | -3.77±0.55 | 90 | -2.98±0.34 |
| M 7 | 8 | 8.35 | 47 | -4.32±0.32 | 56 | -3.55±0.44 | 4 | ··· |
| Hyades | 9 | 8.80 | 94 | -4.96±0.60 | 42 | -4.52±0.81 | 48 | -3.31±0.40 |
| Praesepe | 10 | 8.86 | 36 | -4.82±0.53 | 12 | -4.10±0.78 | 20 | -3.11±0.47 |

Similarly, we show in Fig. 4.7, and in Table IV.4, the same cluster dataset as in Fig. 4.6, this time substituting the mean $L_x/L_{bol}$ for mean $L_x$. We also compare a linear fit of the data to Skumanich-type spin down function (i.e. $L_x/L_{bol} \propto t^{-\frac{1}{2}}$). For the Skumanich relation, we assume that on average all spectral types have a saturated X-ray level at an age of ∼1 Myr. This assumption is consistent with observations of very young open clusters (*e.g.* Feigelson et al., 2002; Stassun et al., 2004). We find

*Note*–For a given color/spectral-type bin, we did not included $L_x/L_{bol}$ values in its linear-fit (see text) for clusters with <10 X-ray detections. For those cases we indicate their mean $L_x/L_{bol}$ vales as "...".

[a] Spectral ranges are defined by Kenyon & Hartmann (1995): F & G Spectral-type $V - I_c < 0.8$, K-type $0.8 < V - I_c < 1.8$, M-type $V - I_c > 1.8$

[b] The letters that come after the following citations represent -X XMM-Newton[0.3-10 keV] and -R ROSAT[0.1-2.4 keV]. *References:***(1)** Cargile & James (*submitted*)-R, **(2)**Jeffries et al. 2006-X, **(3)**Randich et al. 1995-R, **(4)**Patten & Simon 1996-R,**(5)**Randich et al. 1996-R, **(6)**Cargile et al. 2009, **(7)**Stauffer et al. 1994; Micela et al. 1999b-R, **(8)**Pillitteri et al. 2006-X, **(9)**Prosser et al. 1995-R, **(10)**Stern et al. 1995-R.,Perryman et al. 1998, **(11)**Randich & Schmitt 1995-R (***N.B.*:** These reference numbers are also used in Fig. 4.7.)

from our best-fit, linear trends that $L_x/L_{bol}$ is proportional to $t^{-0.64\pm0.41}$, $t^{-0.41\pm0.32}$, $t^{-0.08\pm0.26}$ for spectral-type ranges of F/G, K, and M, respectively.

One can see some features in Fig. 4.7 that give insight into the activity-age relationship in solar-type stars. Formally, in all three mass regimes $L_x/L_{bol}$ decreases as a function of age. Moreover, the rate of decay of the $L_x/L_{bol}$ with age is mass dependent. The earliest spectral type stars in this sample, F- and G-type stars, appear to have $L_x/L_{bol}$ values which decay in a Skumanich-like manner. These higher mass stars are almost exclusively less X-ray active than the saturation level. K-type stars, however, follow a slower decay law of $\sim t^{-0.4}$. Looking more closely, these stars appear to have at or near saturated levels of X-ray emission for ages less than 100 Myr. In older clusters, K stars exhibit reduced magnitudes of X-ray emission due to their increased level of spin down, compared to the their younger ($<$ 100 Myr) counterparts. The M stars have an $L_x/L_{bol}$ evolution with age that is clearly non-Skumanich. In fact, their magnitudes barely decay at all over the first 1 Gyr of their lives (although, see below). We note that our new Blanco 1 results, $L_x$ and $L_x/L_{bol}$, are consistent with the X-ray/age dataset for both younger and older open clusters in the first $10^9$ years of stellar evolution.

We must caution the reader that by stating M dwarfs are only observed at or near saturated levels of X-ray emission, we are not implying that all young, low-mass stars ($<$ 1 Gyr, M spectral types) have $L_x/L_{bol}$ magnitudes of $10^{-3}$. Due to the limiting sensitivities of the ROSAT and XMM-Newton telescopes, the completeness level for

X-ray surveys of open clusters decreases with decreasing mass. Therefore, the only X-ray sources observed at the lowest masses are the brightest X-ray sources, i.e. those with saturated levels of X-ray emission. In fact, one can observe this in the Hyades where, due to its proximity to the Sun, a near complete stellar population for the cluster is known down to a very low mass (Reid, 1993; Bouvier et al., 2008). In the ROSAT study of the Hyades by Stern et al. (1995), they observed X-ray emission from only 30% of the known M dwarfs in the cluster, as compared to 90% of X-ray activity in the known Hyades G stars. Thus, with the extant X-ray datasets for M dwarfs in young, $< 1$ Gyr, open clusters, we are unable to discriminate between the two scenarios of saturated levels of X-ray emission or sample incompleteness.

Cognizant of some limitations in the existing X-ray datasets, let us continue. In Fig. 4.8, the $L_x/L_{bol}$ distributions of two other well studied open clusters, NGC 2547 (age $\sim$ 30 Myr) and NGC 2516 (age $\sim$ 140 Myr), are directly compared to that of Blanco 1. The data for NGC 2547 and NGC 2516 are taken from Jeffries et al. (2006) and Pillitteri et al. (2006), respectively. In NGC 2547, we generally see stars exhibiting saturated levels of X-ray emission at an earlier spectral type when compared to Blanco 1, in accordance with age-rotation-activity paradigm expectations. Thus, one would expect to still see rapidly rotating, higher mass stars that exhibit saturated levels of X-rays. In both clusters, almost all stars with $V - I_c \geq 1.25$ have saturated levels of X-ray emission. Therefore, in this mass regime, their ages and angular momentum as judged by X-ray emission are indistinguishable.

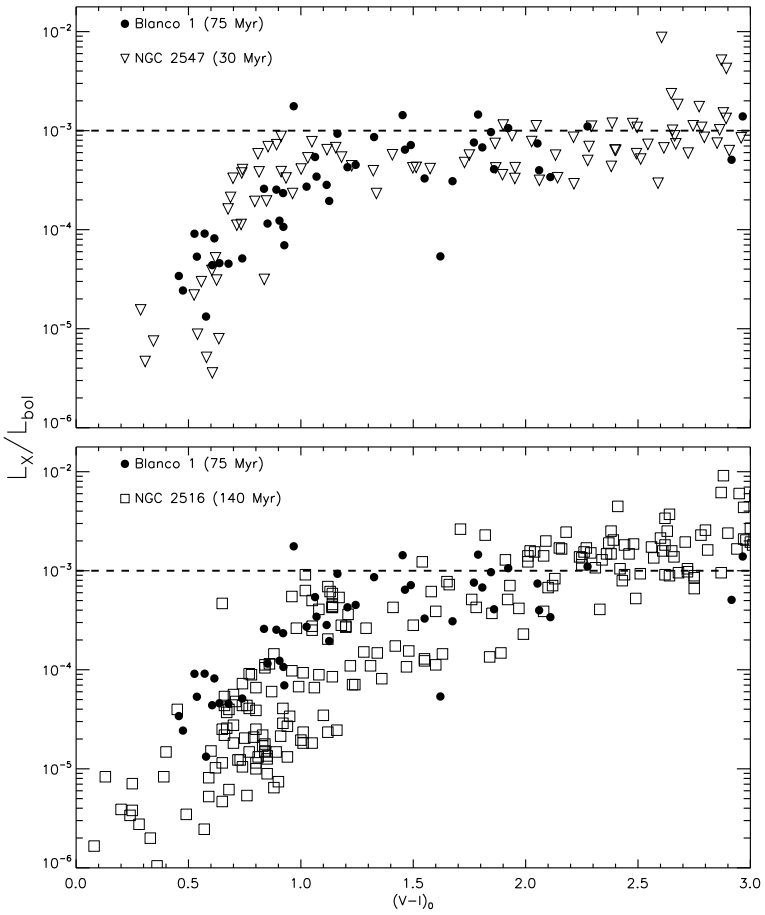


Figure 4.8: $L_x/L_{bol}$ distributions for open clusters NGC 2547 (*triangles*) and NGC 2516 (*squares*) with the Blanco 1 distribution (*solid points*) over-plotted. The dashed line denotes a $L_x/L_{bol}$ of $10^{-3}$, the canonical saturation point of X-ray emission.

A comparison of the X-ray properties in Blanco 1 and NGC 2516 is somewhat less straightforward due to the considerable scatter in the $L_x/L_{bol}$ values for NGC 2516 stars at all masses. For the non-saturated regime, the majority of Blanco 1 stars lie at or above the $L_x/L_{bol}$ distribution for NGC 2516. Moreover, while for Blanco 1

we judge by eye that saturation sets in at $V - I_c = 1.25 \pm 0.02$[1], in NGC 2516 the nexus appears at a redder intrinsic color, $V - I_c = 1.5$. This finding is in agreement with the age-rotation-activity paradigm, that is, for the older NGC 2516, we expect to observe the point where stars exhibit saturated X-ray emission levels at a redder color (i.e. lower mass) when compared to the younger Blanco 1 open cluster. Finally, for the most part stars in the saturated regime of both Blanco 1 and NGC 2516 are indistinguishable in $L_x/L_{bol}$ versus intrinsic $V - I_c$ space. As we state above, this is most probably a result of flux sensitivity limits for the X-ray studies of these clusters, although the considerable scatter in the X-ray distribution of NGC 2516 clouds the issue somewhat.

### 4.2.3 Blanco 1 Comparison to the Pleiades

Blanco 1 is oftentimes compared with the Pleiades cluster due to their similar ages and metallicities (see Chapter III). Under the umbrella of the activity-rotation-age paradigm, one would expect that the X-ray properties of these two clusters should be similar. In Fig. 4.9, we plot the $L_x/L_{bol}$ versus photometric color distributions for both clusters. The Pleiades optical and X-ray photometry is taken from the ROSAT studies of Stauffer et al. (1994); Micela et al. (1999b) and references cited therein. The optical photometry for the Pleiades used by these authors is photoelectric where such data are available, and photographic otherwise. We notice in both clusters

[1]Uncertainty determined from an average $V - I_c$ error for stars along the Blanco 1 main sequence with $V - I_c \sim 1.25$.

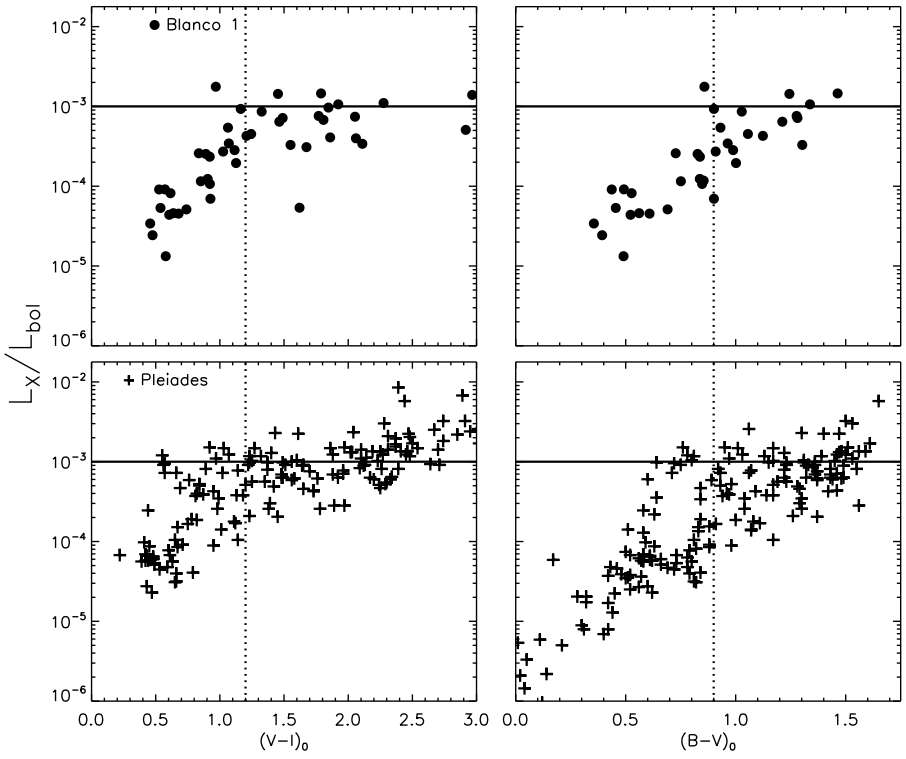


Figure 4.9: Direct comparison of the X-ray to bolometric luminosity distributions for the Blanco 1 (*top*) and Pleiades (*bottom*) open clusters is plotted in intrinsic $V - I_c$ (*left*) and $B - V$ (*right*) space, respectively. The Pleiades optical and X-ray data where taken from Stauffer et al. (1994); Micela et al. (1999b) and references therein. The solid lines represent the canonical saturated level of $L_x/L_{bol}$= $10^{-3}$. The dotted lines represent a by-eye determination of the onset of saturation in Blanco 1.

there are two clear distributions. First, there is an increasing level of $L_x/L_{bol}$ values (more active stars) as mass decreases for bluer, higher mass stars. Second, there is a plateau-like X-ray saturation for all redder, lower mass stars.

However, there does appear to be a difference between the two clusters in the photometric color (*i.e.*, mass) at which X-ray saturation sets in. This mass appears to be higher for the Pleiades, which by the age-activity relationship would indicate

that the Pleiads have not spun down as much as their Blanco 1 counterparts, and therefore would appear to be younger. This finding does not agree with previous age measurements for the two clusters, which are essentially identical. For Blanco 1, fitting of the upper-main-sequence gives ∼120 Myr (see Chapter III); for the Pleiades, upper-main-sequence fitting gives 115 Myr (Naylor, 2009) and the lithium-depletion boundary age is measured to be 125 Myr (Stauffer et al., 1998).

Looking at the CMD for the X-ray sources for Blanco 1 and the Pleiades (Fig. 4.5), we clearly see that there is significant scatter across the Pleiades main sequence when compared to Blanco 1. The X-ray selected, photometric members of Blanco 1 appear to trace a much tighter locus in $M_V/V - I_c$ space when compared to the Pleiades cluster. Assuming that each X-ray identified Pleiad is a *bona fide* member of the cluster, only three possibilities can explain this phenomenon: (1) the photometric spread on the main sequence is real; (2) the quality of the photometry is insufficient to define a tight main-sequence locus; (3) differential reddening across the cluster is artificially introducing photometric scatter in the reddening-free $M_V/(V-I_c)_0$ plane. One or all of these factors may be contribute to some of the discrepancies seen in the $L_x/L_{bol}$ versus color distributions for Blanco 1 and the Pleiades. We do note that there is a larger number of sources identified in the Pleiades studies; therefore, the probability is larger for the Pleiades than for Blanco 1 that nonmembers have been included in these datasets which coincidentally satisfy the criteria used for selection of cluster membership.

Much of the possible confusion in this discussion of age and X-ray activity at the onset of X-ray saturation in the Blanco 1 and Pleiades clusters centers upon the late F to early K stars ($0.6 < B-V < 0.9$; $0.5 < V-I_c < 1.1$). The morphology of these stars in the $L_x/L_{bol}$ versus intrinsic color plane appears unusual (see Fig. 4.9), with a clump of apparently saturated stars lying considerably above (up to an order of magnitude) the general trend of increasing $L_x/L_{bol}$ versus intrinsic color (especially in $B-V$ space). At the present time, with the available data, we cannot adequately explain this phenomenon.

## 4.3 Summary

Being young (∼120 Myr), nearby (∼240 pc), and having a high Galactic latitude ($b = -79°$), the open cluster Blanco 1 presents itself as a valuable laboratory in which to study early stellar evolution. Here, we present a new analysis of the optical/X-ray properties for stars in Blanco 1 using the two extant X-ray surveys (M99 and P04) and a standardized $BVI_c$ photometric catalog from the SPOCS survey; membership selection of this cluster is based on newly derived proper motions. We find optical counterparts to 47 X-ray sources in the cluster. We note that six of these sources were misidentified as cluster nonmembers by previous X-ray studies. In our analysis, we derive new $L_x$ and $L_x/L_{bol}$ values for cluster members and compare the distribution of these parameters to other well studied open clusters. We find that the X-ray properties of Blanco 1 stars are in general agreement with those predicted by the age-

rotation-activity paradigm. However, there is a disagreement between the distribution of $L_x/L_{bol}$ as a function of $B-V$ and $V-I_c$ color for Blanco 1 and the similar age Pleiades open cluster. This may be the result of large scatter seen in the color-magnitude diagram of the Pleiades X-ray sources, although the shift of a $L_x/L_{bol}$ saturation onset toward higher masses in the Pleiades appears to be larger than this scatter would imply. We do not find any evidence for significant long-term X-ray variability in the Blanco 1 cluster members.

Existing X-ray datasets (M99, P04) for Blanco 1, especially for objects fainter than a V$\sim$12, suffer from their reliance on photographic photometry. The analysis of the X-ray properties of Blanco 1 that we present in this manuscript supersedes these earlier analyzes because our new study is founded upon a wide-field, high-quality, homogeneous optical photometric dataset, which crucially, we demonstrate is of high internal self-consistency. This property of the accompanying $BVI_c$ photometry allows us to describe the X-ray characteristics of stars in Blanco 1 as a function of mass, without some of the ambiguities affecting the earlier studies.

As evidence of the power of this new standardized photometric dataset, the X-ray detected, proper motion members of Blanco 1 trace out a tight, low-dispersion main sequence, whereas in contrast the Pleiades cluster shows a much higher level of photometric scatter. We also observe that the absolute level of X-ray emission, as given by $L_x/L_{bol}$, changes along the Blanco 1 main sequence, thus clearly showing that X-ray production in Blanco 1 is mass dependent.

Looking more globally at the connatural relationship between stellar mass, X-ray production, and age, we observe that X-ray production from the stars in Blanco 1 follows very distinct trends seen in other open clusters. Namely, X-ray emission decays as a function of age, and this decay is mass dependent. G-type stars of all ages have X-ray emission that decays with a Skumanich-like trend. However, as one looks at lower mass stars, X-ray emission become less of a function of stellar age. In fact, for the lowest mass (M-type) stars, there is no observable evidence for the reduction of X-ray emission during the first 1 Gyr of their lives, however, due to the limiting flux sensitivities of the ROSAT and XMM-Newton datasets, we are probably not able to detect M-dwarf stars with less than saturated levels of X-ray emission.

## 4.4 Epilogue

### 4.4.1 Role of Rotation in Blanco 1's X-ray Activity Morphology

Revisiting our analysis of the X-ray data in the previous section, we would now like to investigate the role of stellar rotation in the observed X-ray emission morphology of Blanco 1. Unfortunately, rotation periods, necessary for a Rossby number analysis (*e.g.,* Pizzolato et al., 2003), have not been published for Blanco 1. Nevertheless, we have compiled projected rotational velocities (Vsin $i$) measurements from three different spectroscopic surveys of Blanco 1 in order characterize the rotation-rate distribution for the cluster. Jeffries & James (1999) determined Vsin $i$ for 33 photometrically selected G and K stars in the region of Blanco 1 using the UCLES spectrograph on

the AAT. They found 17 of their spectra had radial velocities consistent with the stars being single cluster members. Mermilliod et al. (2008) report the results of a spectroscopic survey of the central 1.5 deg$^2$ of Blanco 1, using the photoelectric scanner CORAVEL on the Danish 1.54 m telescope at ESO. They obtained Vsin $i$'s for 68 probable cluster members. Finally, James et al. (2010) report the results of an extensive WIYN multi-object spectroscopic survey, in which they derive precise radial velocities ($\pm$1 kms$^{-1}$) and Vsin $i$'s for 69 single cluster members of Blanco 1. While combining these catalogs, we sorted the duplicate measurements keeping the value from the survey with the highest resolution: Mermilliod et al. (2008), Jeffries & James (1999), and then James et al. (2010). Our catalog of Blanco 1 members with Vsin $i$ measurements contained a total of 97 stars ranging from $B - V = 0.25$-1.5.

In Fig. 4.10, we plot the rotation rate as a function of intrinsic color for Blanco 1 and the Pleiades open clusters. We see several trends in both distributions. The higher mass stars ($B - V_0 < 0.6$) have a large range of rotation rates including a large number of rapid rotators, consistent with sedate spin-down due to thin convection zones. The G-type stars ($0.6 < B - V_0 < 0.8$) exhibit a relatively narrow range of rotation rates ($< 40$ km s$^{-1}$). Whether this more narrow range of Vsin $i$ is due to initial conditions, rapid spin-down due to efficient dynamo action, or something more exotic such as internal stratification of angular momentum distributions remains debatable. Later-type stars, however, show a greater dispersion of rotation rates, consistent with longer spin-down timescales for stars of lower mass (Stauffer et al.,

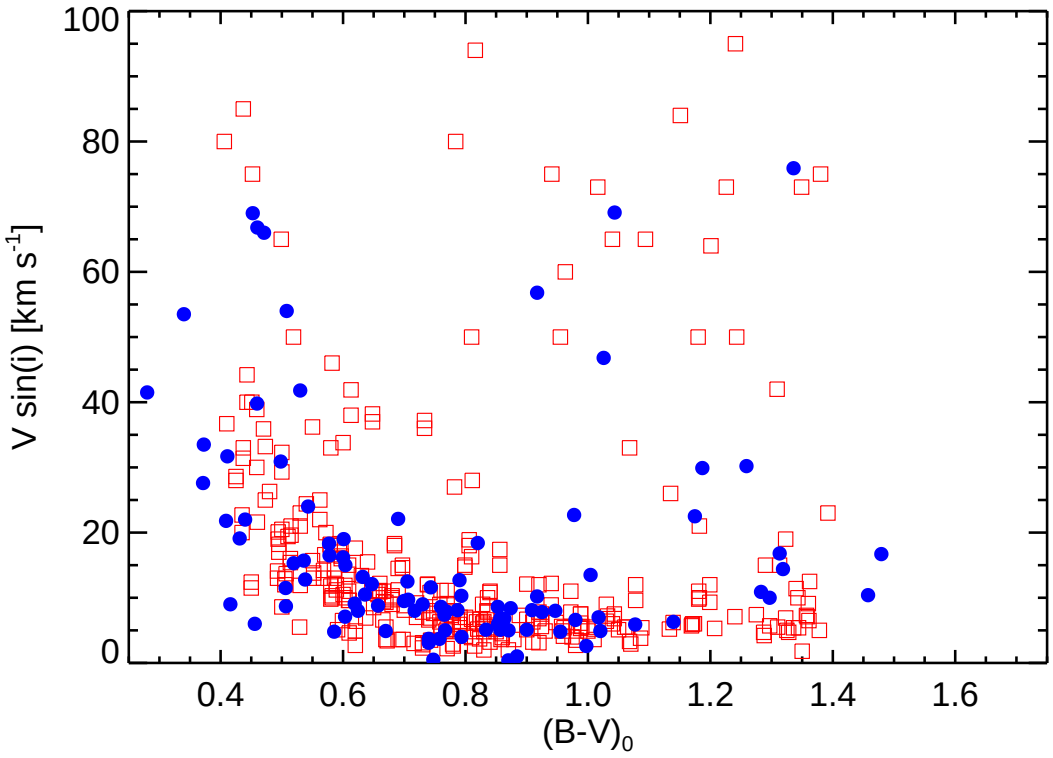


Figure 4.10: Rotation rate plotted versus intrinsic color for the Blanco 1 (blue dots) and Pleiades (red open squares) open clusters. Pleiades data are taken from Soderblom et al. (1993) and Queloz et al. (1998).

1991; Krishnamurthi et al., 1997; Barnes, 2007).

We also note the similarity of the Pleiades and Blanco 1 rotation-rate distributions. In order to quantify this similarity, we performed a two-dimensional two-sample Kolmogorov-Smirnov (K-S) test on their Vsin $i$ distributions. We calculate that the two Vsin $i$ distributions have probabilities of 51% that they were drawn from the same parent distribution. Assuming that these measured rotation rates are representative of the clusters' total angular momentum distributions, then according to the ARAP their similarity provides evidence for these two clusters to be coeval.

Of the 97 unique Blanco 1 cluster members with measured Vsin $i$'s, we have matched 34 with X-ray source detections in either the ROSAT or XMM-Newton study of the cluster. We plot in Fig. 4.11 the activity-rotation relationship for Blanco 1 and the Pleiades, segregating the data into two color bins: $B-V < 0.6$, plotted in the top panel, and $B-V > 0.6$, plotted in the bottom panel. We find that for the higher-mass stars (top panel), the magnitude of X-ray emission is not correlated with rotation, which is expected due to the lack of significant outer convection zone in these stars. For the lower mass stars however, we observe two trends: (1) stars with Vsin $i \lesssim 20$ km s$^{-1}$ exhibit various magnitudes of X-ray emission, and (2), rapid-rotating stars (Vsin $i \gtrsim 20$ km s$^{-1}$) have saturated levels of X-ray emission at $L_x/L_{bol} \sim 10^{-3}$. In this regard, Blanco 1 appears nearly identical to the coeval Pleiades cluster (compare this figure to Fig. 1.8).

We note that in our earlier comparative analysis between Blanco 1 and the Pleiades

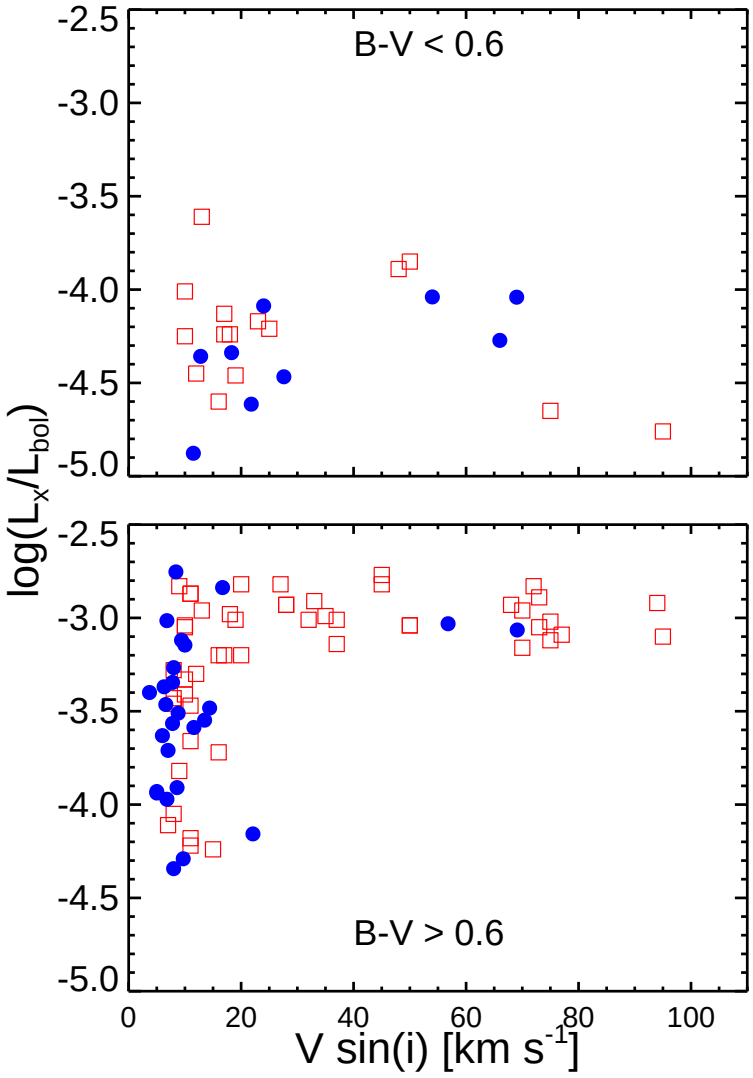


Figure 4.11: Vsin $i$ plotted as a function of X-ray to bolometric luminosity ratio for stars in Blanco 1 (blue dots) included in both the X-ray and spectroscopic surveys. Similarly, for the Pleiades open cluster (red open squares). The distribution have been divided into stars with $(B-V)_0 < 0.6$ (top) and $(B-V)_0 > 0.6$ (bottom). For the higher-mass stars (top panel), the magnitude of X-ray emission is not correlated with rotation, which is expected due to the lack of significant outer convection zone in these stars. For the lower mass stars (lower panel) however, two trends are observed: (1) stars with Vsin $i \lesssim 20$ km s$^{-1}$ exhibit various magnitudes of X-ray emission, and (2), rapid-rotating stars (Vsin $i \gtrsim 20$ km s$^{-1}$) have saturated levels of X-ray emission at $L_x/L_{bol} \sim 10^{-3}$. In this regard, Blanco 1 appears nearly identical to the coeval Pleiades cluster. Pleiades data taken from Stauffer et al. (1994).

(see Section 4.2.3), we found slight differences between the morphology of $L_x/L_{bol}$ versus color distributions for the two clusters. Here, using rotation rate instead of stellar colors, we see a much clearer trend with rapid rotation being associated with X-ray saturation. This is suggestive that for these two clusters, X-ray emission is better correlated with rotation than with stellar temperature (*i.e.,* mass). This is also discussed in the extensive Orion observations with Chandra by Feigelson et al. (2005).

### 4.4.2 Characterizing X-ray Emission in IC 4665

Due to its young age, IC 4665 is commonly used to calibrate the level of X-ray activity in PMS stars (see Chapter 3.3 for full description of cluster). Here, we would like to perform a re-analysis of extant X-ray data for IC 4665 in order to characterize the X-ray emission for cluster members. Similar to Blanco 1, we use SPOCS optical photometry for the cluster to derive new X-ray/optical distributions, then directly compare these to Blanco 1 in order to estimate a relative activity-age for IC 4665.

#### 4.4.2.1 Extant ROSAT Observation of IC 4665

Giampapa et al. (1998) reported the results of a 76.9 ksec exposure of the cluster with the HRI instrument on ROSAT , resulting in 43 detected X-ray sources. There were 253 stars listed in the Prosser (1993, P93) catalog that fall within the HRI field-of-view. They identified 28 X-ray sources with an optical counterpart within 15″. For

these, they calculated X-ray fluxes using their derived count-rate conversion factor and measured X-ray luminosities using a distance of 340 pc. Ratios of X-ray to bolometric luminosity were derived using standard bolometric corrections calculated from P93 photometry. In Chapter III, we show the P93 dataset to contain large systematic photometric uncertainties, as well as determine that their membership selection is hampered by unreliable proper motions. Unfortunately, Giampapa et al. relied on the P93 membership catalog to match X-ray sources with optical counterparts that were "probable" cluster members.

#### 4.4.2.2 Updated X-ray Properties of IC 4665 Members

For the 28 X-ray sources with optical counterparts listed in Giampapa et al., we use our new SPOCS photometry to reanalyze the X-ray distributions of IC 4665. We have assigned new $B-V$ and $V-I_c$ colors for optical counterparts, calculated new X-ray luminosities using the updated distance from the SPOCS isochrone modeling of IC 4665 (355 parsecs; see Chapter III), and derived new bolometric luminosities using corrections from Johnson (1966) for stars with intrinsic $V-I_c < 1.6$ and the formalism given in Monet et al. (1992) for stars with intrinsic $V-I_c > 1.6$. We also define which X-ray sources are probable cluster members based on its optical counterpart positions being within error of our best-fit cluster sequence from the SPOCS CMD (see Chapter III). We find optical counterparts to 20 X-ray sources listed in Giampapa et al.. Of those, we identified 15 as associated with probable IC 4665 cluster members. The

eight X-rays sources that we did not match with optical counterparts are all previously associated with stars having V-band magnitudes outside the brightness range of the SPOCS survey (V $<$ 10 or V $>$ 17). In Fig. 4.12, we show the new $L_x/L_{bol}$ values, with propagated uncertainties, as a function of intrinsic $V - I_c$ color for members of IC 4665.

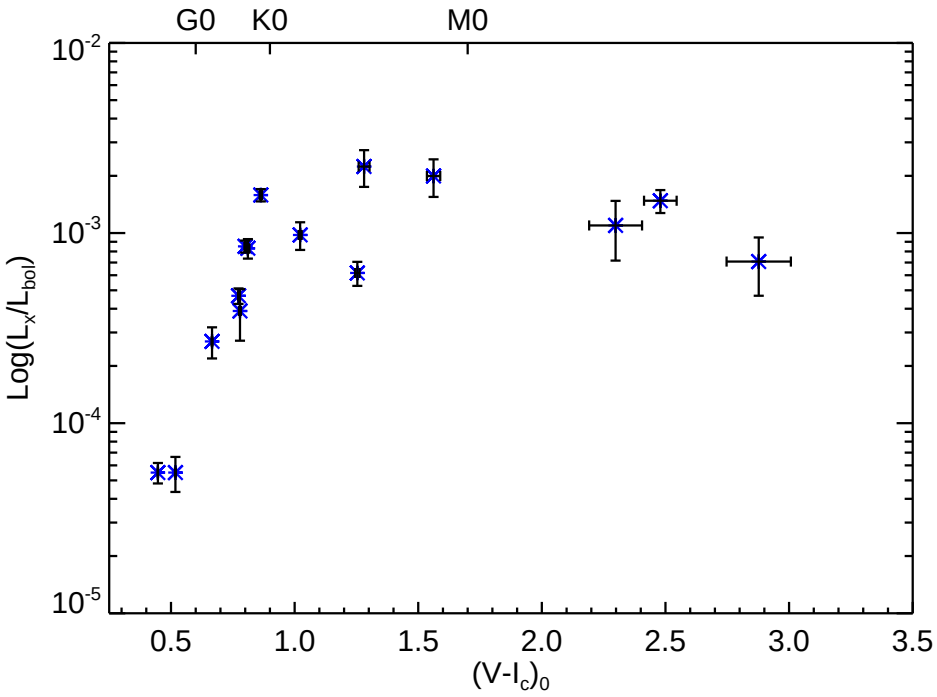


Figure 4.12: Ratio of X-ray to bolometric luminosity plotted as a function of intrinsic color for sources in IC 4665. Spectral-type ranges listed at top of figure are defined by Kenyon & Hartmann (1995).

Although IC 4665 has a limited number of cluster members detected in X-rays, primarily due to its relatively large distance compared to other well-studied clusters, it is still quite evident that its overall distribution of X-ray emission is similar to

other young open clusters. Namely, we observe a trend of increasing X-ray emission with redder colors for stars with intrinsic $V - I_c \lesssim 1$, and a saturation plateau for later-type stars. Several of the IC 4665 stars showing saturated X-ray emission lie above the canonical limit of $L_x/L_{bol} = 10^{-3}$, which is not seen in other young clusters, *e.g.,* NGC 2547. At this point, we cannot decipher the exact cause of this increased level of $L_x/L_{bol}$. Nevertheless, these stars do not appear to have discrepant optical photometry, and have bolometric luminosities derived from commonly used bolometric corrections. Therefore, this suggests that either this increased $L_x/L_{bol}$ emission is real and contrary to observed trends in other clusters, or it is a result of the modeling procedure used by Giampapa et al. to calculate the ROSAT X-ray fluxes.

Assuming that the stars with $V - I_c = 1.0$-$1.5$ are representative of the true saturation level in IC 4665, we observe that the three reddest stars exhibit slightly reduced $L_x/L_{bol}$ values, suggesting that these stars have *supersaturated* X-ray emission. In other young open clusters, there is an observed decline in the magnitude of X-ray emission from stars with Rossby number $\lesssim 0.03$, or for low-mass stars, like those with intrinsic $V - I_c > 2.0$ in IC 4665, at rotational velocities $\gtrsim 100$ km s$^{-1}$, or a rotation period $\lesssim 10$ hours (Randich, 1998; James et al., 2000). Like the observed saturation phenomenon, the physical mechanism behind *supersaturation* is still a matter of debate (see Chapter I). Scholz et al. (2009) showed that the majority of low-mass stars in IC 4665 rotate at rotation periods $< 10$ hours, thereby providing evidence that we should see *supersaturated* X-ray emission in IC 4665. However, currently the lack of

significant number of X-ray sources with $V - I_c < 2.0$, as well as not having measured rotation rates for the optical counterparts to these X-ray sources, makes the evidence tentative for observed X-ray *supersaturation* in the lowest-mass IC 4665 stars.

### 4.4.3 Comparison of Blanco 1 and IC 4665 X-ray Emission Morphology

In Giampapa et al., the authors suggest that IC 4665 has an X-ray distribution indicative of a cluster that is older than $\alpha$ Persei ($\sim$70 Myr), and very similar to the Pleiades ($\sim$120 Myr). They find that the color at which the IC 4665 X-ray distribution appears to transition to the saturated regime is redder (lower-mass) than $\alpha$ Persei, and is in agreement with the color of saturation for the Pleiades. Therefore, according to the age-activity relationship, IC 4665 should have an age of $\sim$120 Myr.

In order to evaluate the validity of this X-ray-age determination, we employ our new analysis of X-ray data for Blanco 1 and IC 4665 stars. In Fig. 4.13, we compare the distributions of $L_x/L_{bol}$ as functions of intrinsic $V - I_c$ colors for stars in IC 4665 to Blanco 1 (left panel) and NGC 2547 (right panel). We find that the morphology of X-ray emission in IC 4665 is more similar to NGC 2547 compared to Blanco 1, in particular for stars with intrinsic $V - I_c < 1.0$. In order to quantify this, we performed a two-dimensional two-sample K-S test on these distributions. We find a probability of 5% that Blanco 1 and IC 4665 have X-ray emission distributions that were taken from the same parent distribution. Preforming a similar analysis for the young open cluster NGC 2547, we find an equally small K-S probability of 5%. However, if we

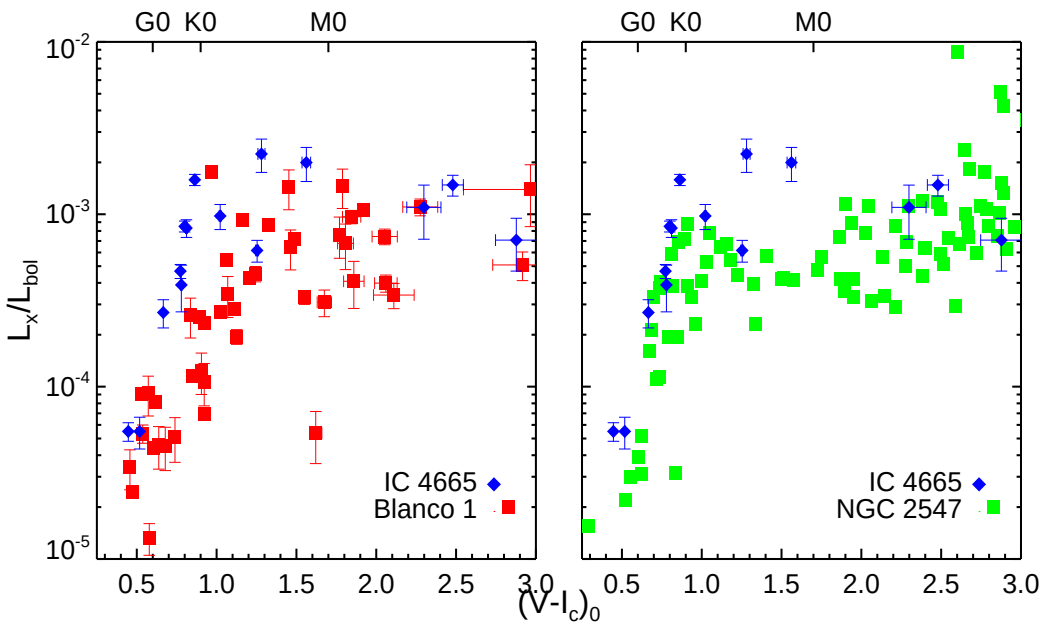


Figure 4.13: $L_x/L_{bol}$ plotted as a function of intrinsic $V - I_c$ color for sources in IC 4665. Also plotted for comparison purposes are values for Blanco 1 (left) and NGC 2547 (right). Blanco 1 measurements are adopted from Section 4.1, and NGC 2547 data are taken from Jeffries et al. (2006). Spectral-type ranges listed at top of figure are defined by Kenyon & Hartmann (1995).

limit this comparative analysis to the color region $V - I_c < 1$, we find that Blanco 1 and IC 4665 the K-S probability for the subset distributions remains small (3%), but the K-S probability for IC 4665 and NGC 2547 increases to 17%. This suggestes that, for stars with $V - I_c < 1$, the X-ray morphology of IC 4665 is more similar to the young open cluster NGC 2547 ($\sim$35 Myr) than the $\sim$100 Myr Blanco 1. Therefore, according to the ARAP, IC 4665 is expected to have an age closer to NGC 2547 than to Blanco 1, in agreement with our isochrone age results derived in Chapter III.

Looking at the wider implication of this work, one could imagine using a similar

K-S testing technique to do a comparative study for clusters with well sampled X-ray distributions. In theory, a tool of this nature would be useful in placing empirical age constraints on open clusters based solely on the morphology of their X-ray–optical photometry. However, scatter in the typical X-ray distributions for open clusters due to X-ray variability, unresolved binaries with unaccounted for X-ray active low-mass companions, and uncertainty in the optical photometry make this a difficult task.

# Chapter V

# WORK IN PROGRESS: TOWARDS RECONCILING EMPIRICAL AND MODEL-PREDICTED STELLAR AGES

## 5.1 Empirical Constraints on the Treatment of Convection in PMS Stellar Models

In Chapter II, we determined that the only PMS models that accurately predict the effective temperatures of both Par 1802 A & B are those produced by D'Antona & Mazzitelli (DAM97). This agreement is due to DAM97 models predicting initially high stellar temperatures at very-early ages (+400 K compared to other PMS models at age $< 1$ Myr), and a steep drop in surface temperature at $\sim 1$ Myr. These types of morphological differences are due to the different variety of input physics into PMS models, particularly the detailed treatment of convection (see discussion in Chapter I, and Siess et al., 2000; Hillenbrand & White, 2004).

Here, we would like investigate more closely the question:*why* do the DAM97 models produce more accurate temperatures for low-mass PMS stars? In Table V.1, we summarize the various physical ingredients included in the currently available PMS models. One particular difference in the DAM97 models compared to the other models is their treatment of convection. Summarizing our discussion from Chapter I, due to computational resources, most models use a mathematically simple mixing-length theory (MLT; Böhm-Vitense, 1958) treatment of convection. Here, a characteristic

Table V.1. Low-Mass Pre-Main-Sequence Models

| PMS[a] Model | Internal Opacities | Equation of State | Reaction Rate | Convection | Atmosphere |
|---|---|---|---|---|---|
| DAM97 | RMO[b] | MHD[c] | Fowler et al. (1975)<br>Caughlan & Fowler (1988) | FST | gray |
| BCAH98 | RMO | SCVH[d] | Chabrier & Baraffe (1997) | MLT<br>$\alpha = 1$ | non-gray<br>Hauschildt et al. (1999) |
| SDF00 | RMO | MHD | Caughlan & Fowler (1988) | MLT<br>$\alpha = 1.6$ | non-gray<br>Plez (1992); Kurucz (1991) |
| PS99 | RMO | MHD | Fowler et al. (1975) | MLT<br>$\alpha = 1.5$ | gray |

[a]DAM97 – D'Antona & Mazzitelli (1997); BCAH98 – Baraffe et al. (1998); SDF00 – Siess et al. (2000); PS99 – Palla & Stahler (1999)

[b]Rosseland mean opacity (Alexander & Ferguson, 1994)

[c]Magnetohydrodynamic equation of state defined by Mihalas et al. (1988)

[d]Equation of state defined by Saumon et al. (1995)

mixing-length, $\alpha$, is typically set to be between one and two times the pressure scale height. Alternatively, the DAM97 models use a more complex convection prescription, called full-spectrum turbulence (FST; Canuto & Mazzitelli, 1991, 1992). This method is a generalized version of MLT that uses a wide spectrum of eddy sizes for $\alpha$. Canuto & Mazzitelli (1991) claims that using a FST model of convection will result in higher predicted temperatures compared to MLT, because it includes the contribution of large groups of various sized eddies to the overall convective flux of heat in PMS stars. In addition, these eddies also have the effect of making PMS stars temporarily super-adiabatic, with the loss of heat causing a rapid short-lived decrease in stellar surface temperature at $\sim$1 Myr. It has been shown that both MLT and FST accurately predict the Sun's temperature (Montalbán et al., 2004). However, FST's more realistic

treatment of convection is expected to become exceedingly more important for low-mass PMS models of stars on the Hayashi track, like Par 1802 A & B, because convection is the primary heat transfer mechanism throughout the entire star (*i.e.,* fully convective). In fact, the largest offsets between the observed temperatures of models using the two different treatments of convection are found at low-masses and early ages (see Fig. 1.2).

Our analysis of Par 1802 supports this finding. To get temperatures predicted to be high enough for a pre-main-sequence star to match the observed temperature of Par 1802 A, we require FST treatment of convection, also yielding a rapid decrease in temperature during the first $\sim$1 Myr of evolution, which explains the temperature of Par 1802 B. However, we caution the reader that our recommendation for using FST in PMS models is based solely on our analysis of Par 1802. Empirical temperature measurements of other PMS stars, particularly for temperature domains where we see the largest discrepancies between models, *i.e.,* low-mass stars ($< 1 M_{\odot}$) at early ages ($< 1$ Myr), would further help constrain the input physics used by the available PMS models, particularly the detailed modeling of convection.

Finally, because stellar colors and magnitudes are empirical proxies for effective temperatures and luminosities, we would like to use CMD isochrone modeling of open clusters to give us further insight into the effects of using different treatments of convection. In fact, our analysis on the isochrone modeling of IC 4665 in Chapter III suggests that the derived isochronal ages and distances between $B-V$ and $V-I_c$

CMDs are most consistent for the D'Antona & Mazzitelli models. Whether this is an effect of DAM97 usage of FST convection, or some other manifestation of different input physics in the DAM97 models (*e.g.,* gray versus non-gray stellar atmospheres) is yet to be determined.

## 5.2 Reconciling Empirical and Model-Predicted Ages Via Changes in Stellar Radii?

Observations have shown that lithium depletion boundary (LDB) ages are systematically older than isochrone ages by a factor of ∼1.5 for the same cluster (see Burke et al., 2004). These systematic offsets are commonly explained by suggesting there is missing physics in stellar evolution models, such as large amounts of convective overshoot (see discussion in Chapter I). Recently, Yee & Jensen (2010) provide a further explanation for these offsets by suggesting that an increase in the radii of young PMS stars would put into agreement LDB and isochrone ages. This hypothesis is supported by observations that show PMS models under-predicting low-mass stellar radii by 10-20% (Ribas et al., 2008), which is assumed to be the effect of magnetic activity. Indeed, recent studies into the effects of magnetic fields on stellar parameters have shown promise in reproducing these larger observed radii (Chabrier et al., 2007).

Inflated stellar radii would have a two-fold effect on the isochrone and LDB ages: (1), incorporating inflated stellar radii in PMS models would result in longer contraction timescales for PMS stars. Consequently, for a given location on an H-R diagram,

these adjusted models would predict older isochrone ages; and (2), inflated radii would cause PMS stars to have lower central temperatures, thereby slowing the rate of Li depletion and pushing the LDB for a given age to a lower-mass star. Therefore, for a measured LDB mass (or luminosity) you would derive a younger age than would be predicted by PMS models that do not incorporate the inflated radii. In other words, inflating stellar radii in PMS models would result in *older* isochronal ages, as well as *younger* LDB ages.

### 5.2.1 Possible LDB Detection in Blanco 1

In order to further investigate this effect, we present preliminary results from our ongoing LDB study of Blanco 1. We obtained spectra during the fall of 2009 for Blanco 1 target stars using the Gemini Multi-Object Spectrograph (GMOS) in queue schedule mode on the Gemini-North telescope (Hook et al., 2004) with the R831 (G5302) grating blazed at 7570Å, with a blue-blocking OG515 (G0306) filter. The GMOS spectrograph can observe up to ∼40 objects simultaneously in a $5\farcm5 \times 5\farcm5$ field of view, using a custom drilled multi-object slit-mask. For our Blanco 1 targets, we selected $1''$ slitlets resulting in a resolving power of R∼4400. We observed 6 total fields containing 11 probable members from the Moraux et al. (2007) low-mass photometric catalog with an apparent magnitude range bracketing the expected LDB of Blanco 1, *i.e.,* $I_c$ =18.5-19.7. We used exposure times between 65 and 110 minutes, depending on the faintest target in each field, giving us S/N $\gtrsim$ 15-20.

Taking full advantage of the multi-object capabilities of the GMOS instrument, we also observed 1-3 additional stars in each field with $I_c$ ∼14.5-18.0 that have been identified as possible members of Blanco 1 from their location near the cluster sequence in our SPOCS color-magnitude diagrams. Most of these stars had no previously ancillary evidence for membership to Blanco 1 because their brightness falls below the faintness limit of most previous Blanco 1 studies (*e.g.,* proper motions for the SPOCS catalog and James et al.*in prep* have a faintness limit of $I_c = 14.5$). Not only does the inclusion of these stars in our program increase the total number of known Blanco 1 members, but they also help us identify the magnitude range of stars that have already depleted their lithium content, thus allowing for a more confident Blanco 1 LDB measurement.

In all, we acquired spectra for 21 objects, from which we identified 12 as being possible Blanco 1 cluster members based on three different membership criteria: (1) the object fall near the cluster sequence in an $I_c$ versus $I_c - K_s$ CMD; (2) the object had to have a radial velocity near the cluster's systemic velocity (+6 km $s^{-1}$, Mermilliod et al., 2008); and (3) using a visual inspection, the object had to have H$\alpha$ emission above its continuum level. For these 12 objects, we also visually inspected the spectral region around the 6708 Å Li absorption feature, using this line as an indicator of the presence (or absence) of lithium in the star. In Fig. 5.1, we plot a CMD of the 12 possible Blanco 1 cluster members, identifying whether we were able to detect Li absorption near 6708 Å. Based on these data, a clear trend is apparent; namely,

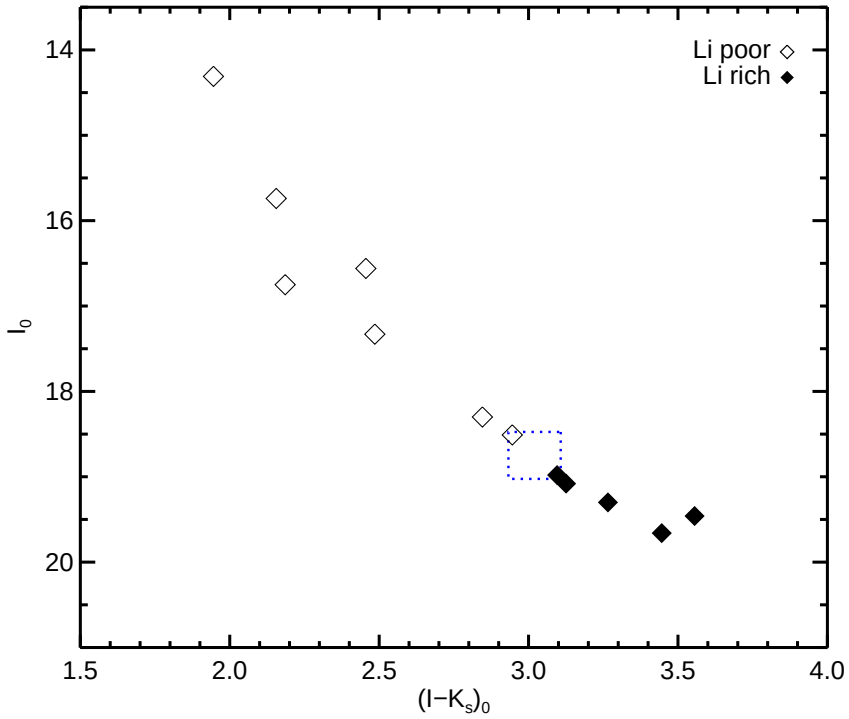


Figure 5.1: $I_c$, $I_c-K_s$ color-magnitude diagram for very-low-mass Blanco 1 members. Filled and open symbols represent those stars with and without Li absorption, respectively. We have assumed a reddening of $E(B-V) = 0.016$ and an extinction of $A_V = 0.05$. The dotted box represents our best estimate of the position and uncertainty of the LDB in Blanco 1.

stars brighter than $I_c \sim 19$ do not exhibit strong Li absorption, suggesting that they have already depleted their natal Li content, and the fainter stars all showed the presence of Li in their spectra. This would suggest that the LDB of Blanco 1 is located approximately at an $I_c = 19$.

At this point, we would like to make clear to the reader that our LDB project for Blanco 1 is ongoing and the results presented here should be considered preliminary. In order to fully characterize the Li abundance distribution for the very-low-mass members of Blanco 1, we would need to perform a more rigorous spectral analysis

on our GMOS spectra. An example of this type of analysis is presented in Jeffries & Oliveira (2005). In the future, we will perform a similar spectral analysis, and propose to observe additional spectra in order to better constrain the location of Blanco 1's LDB. Nevertheless, In the interest of investigating the effects of inflated radii on the predicted ages from PMS models, we continue our discussion assuming that the LDB of Blanco 1 is located at an $I_c = 19$; however, noting that, although the general methodology of our analysis is sound, our determination of the precise location of Blanco 1's LDB, and subsequently its LDB age, may change with future analysis.

By assuming that the LDB of Blanco 1 is located on the cluster sequence between the faintest star showing no Li and the brightest star with Li absorption, *i.e.,* intrinsic $I_c = 18.5$-$19.0$ and $I_c - K_s = 2.95$-$3.10$, we define a region in color-magnitude space, as indicated with the box in Fig. 5.1, within which lies the LDB of Blanco 1. We thereby contend that the LDB of Blanco 1 is located at intrinsic $I_c = 18.75 \pm 0.25$ and $I_c - K_s = 3.03 \pm 0.1$, where the quoted values and uncertainties are defined by the median values and range of possible LDB colors and magnitudes. We converting the apparent magnitude of Blanco 1's LDB to a luminosity using a distance modulus of 6.58 as determined from the HIPPARCOS distance to Blanco 1 (van Leeuwen, 2009), and a reddening and extinction values based on an $E(B - V) = 0.016$ (average of published values). Our derived Blanco 1 LDB luminosity can now be converted to an age with the help of theoretical evolution models that predict the depletion rate

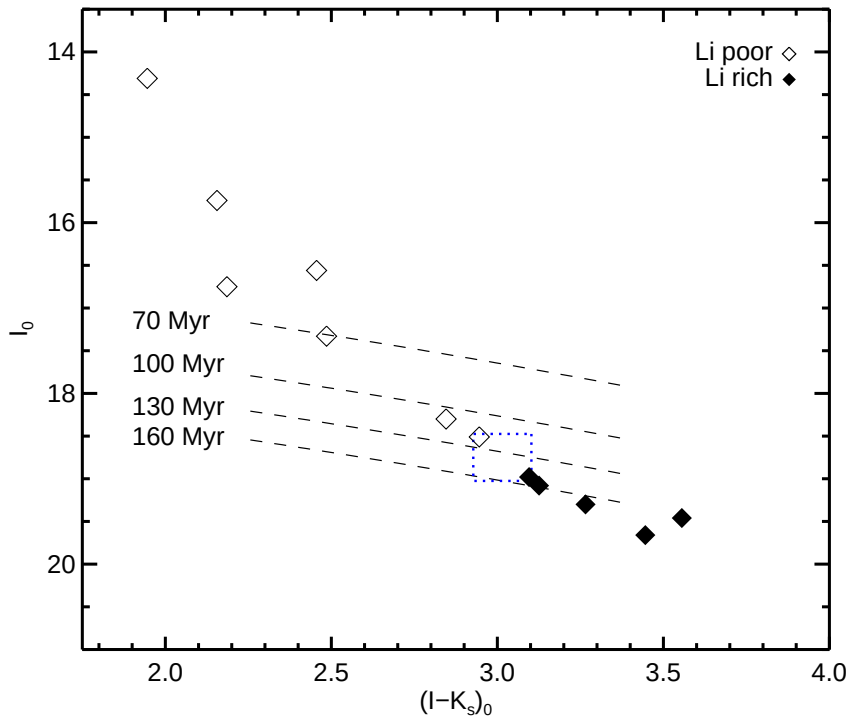


Figure 5.2: $I_c$, $I_c-K_s$ color-magnitude diagram for very-low-mass Blanco 1 members. Symbols are the same as Fig. 5.1. Constant luminosity loci (dashed lines) for the predicted LDB luminosity from the Baraffe et al. models are plotted for various ages.

of stellar Li content. These stellar models predict the luminosity of the LDB as a function of age, which we compared directly to our observed Blanco 1 LDB.

We plot in Fig. 5.2 the CMD indicating the possible location of Blanco 1's LDB, and place lines of constant bolometric luminosity for the theoretical LDB luminosity at various ages as predicted by the Baraffe et al. (1998) PMS models. To be clear, by definition, the LDB is actually just a point on the cluster sequence. The plotted luminosity loci indicate the predicted location of the LDB from where they intersect the cluster sequence. These curves are not flat since, for a given bolometric magnitude,

the bolometric correction changes with color (or effective temperature). For Blanco 1, we see that the 130 Myr LDB luminosity locus is falls near the center of our assumed LDB region, suggesting that Blanco 1 has an LDB age of ∼130 Myr according to the Baraffe et al. models.

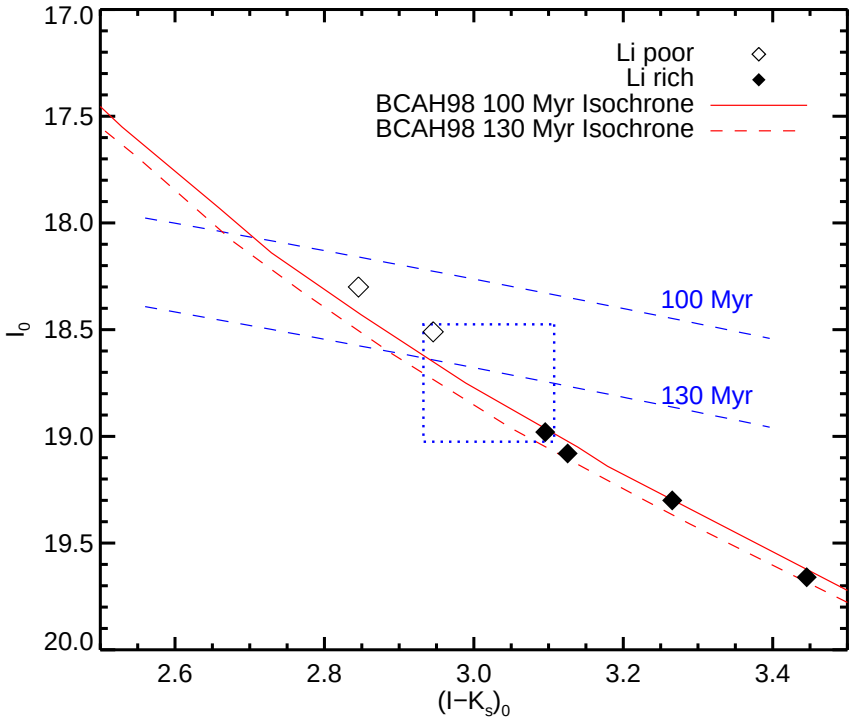


Figure 5.3: Closeup $I_c$, $I_c-K_s$ color-magnitude diagram for the region around the assumed LDB of Blanco 1. Symbols are the same as Fig. 5.1. Also plotted are the predicted PMS isochrone from the Baraffe et al. (1998) models for 100 and 130 Myr. The isochrones have been shifted to the best-fit distance for Blanco 1 from Chapter III.

In Fig. 5.3, we also plot the predicted 100 and 130 Myr LDB loci and isochrones from Baraffe et al. (1998) on Blanco 1's low-mass CMD. We find that the 100 Myr PMS isochrone model is a good match to the observed Blanco 1 cluster sequence;

although, we can not rule out the agreement with the 130 Myr isochrone due to the scatter along the cluster sequence. According to the Baraffe et al. models neither the predicted 100 nor the 130 LDB location, indicated by the point where the LDB luminosity locus cross the model isochrones for a specific age, agree with the empirical LDB for Blanco 1. Although both dating techniques – LDB and isochrones – use the same stellar evolutionary models, in this case the PMS models from Baraffe et al., we see significant differences in the predicted ages one can expected depending on if you using the location of a cluster's LDB or the best-fit isochrone from its pre-main-sequence.

As stated above, by inflating the predicted radii in the PMS models, we will derive older isochrone age and younger LDB ages. In the case of Blanco 1, we can use the premise of this hypothesis to converge Blanco 1's isochrone and LDB ages by manually adjusting PMS models to account for an increase in stellar radii, and compare the resulting isochrones/LDB locations to our empirical determinations for Blanco 1. More specifically, we manually increase the predicted radii for the Baraffe et al. models while tracking the resulting location of the predicted LDB, *i.e.,* the intersection of the adjusted isochrones and the lines of constant LDB luminosities. From this type of analysis, we find that a 5% radii inflation in the 115 Myr stellar model from Baraffe et al. places the LDB at approximately our assumed location of Blanco 1's LDB, *i.e.,* $I_c \sim 19$ (see Fig. 5.4).

Interestingly, when we compare this adjusted ∼115 Myr LDB/isochrone age for

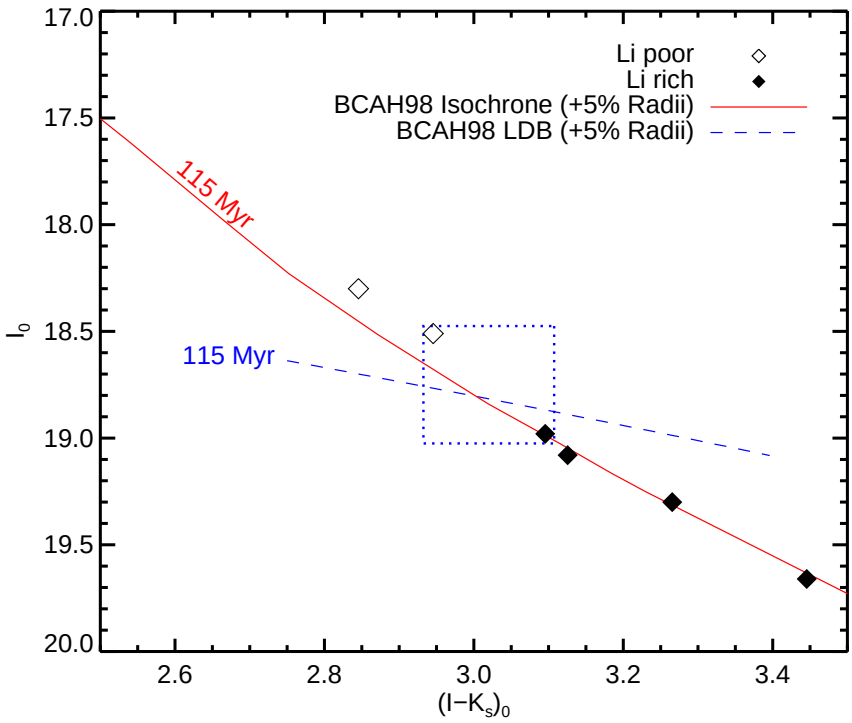


Figure 5.4: Closeup $I_c$, $I_c-K_s$ color-magnitude diagram of our assumed LDB region for Blanco 1. Symbols are the same as Fig. 5.1. Also plotted are the adjusted (+5% increase in radii) 115 Myr PMS isochrone (red line) and 115 Myr LDB luminosity line (blue dashed line) from the Baraffe et al. models.

Blanco 1 to our isochrone modeling in Chapter III, we find a high amount of agreement. We calculated a mean upper-main-sequence age of $115^{+6}_{-20}$ Myr, and a mean PMS isochrone age of 125±19 Myr as derived from higher-mass stars in the SPOCS survey. The agreement of these three ages for Blanco 1 suggests that a small increase in predicted low-mass stellar radii can be used to explain much of the chronometric offsets seen in stellar evolution models. However, this qualitative statement is as far as the current state of our Blanco 1 LDB study presently allows. Eventually, our future analysis will provide us a more quantitative measure of how much PMS models

are under-predicting stellar radii, therefore providing valuable empirical constraints for their future refinement.

# Appendix A

## CATALOG OF IC 4665 PHOTOMETRIC MEMBERS

Table A.1: Catalog of IC 4665 Photometric Members

| Mosaic Field | Object Number | V | $B-V$ | $V-I_c$ | Phot Mem[a] $[B-V]$ | Phot Mem[a] $[V-I_c]$ | Mem Key[b] |
|---|---|---|---|---|---|---|---|
| F5 | 329 | 11.431±0.001 | 0.538±0.001 | 0.664±0.001 | Y | Y | XR,RV |
| F3 | 184 | 11.551±0.001 | 0.558±0.001 | 0.682±0.001 | Y | Y | RV |
| F5 | 321 | 11.609±0.001 | 0.515±0.001 | 0.587±0.001 | N | Y | ··· |
| F7 | 417 | 11.620±0.001 | 0.655±0.001 | 0.784±0.001 | Y | N | ··· |
| F2 | 247 | 11.637±0.001 | 0.674±0.001 | 0.783±0.001 | Y | N | ··· |
| F6 | 240 | 11.658±0.001 | 0.472±0.001 | 0.591±0.002 | N | Y | RV,J |
| F9 | 529 | 11.812±0.001 | 0.666±0.001 | 0.852±0.002 | Y | N | ··· |
| F7 | 178 | 11.857±0.001 | 0.637±0.001 | 0.763±0.001 | Y | Y | ··· |
| F3 | 216 | 11.878±0.001 | 0.704±0.001 | 0.866±0.002 | Y | N | ··· |
| F8 | 236 | 11.915±0.001 | 0.702±0.001 | 0.884±0.002 | Y | N | ··· |
| F5 | 160 | 11.927±0.001 | 0.681±0.001 | 0.790±0.001 | Y | N | RV |
| F2 | 448 | 11.938±0.001 | 0.728±0.002 | 0.885±0.002 | Y | N | ··· |
| F1 | 307 | 11.985±0.001 | 0.731±0.002 | 0.848±0.002 | Y | N | ··· |
| F9 | 246 | 12.011±0.001 | 0.613±0.002 | 0.756±0.002 | Y | Y | ··· |
| F6 | 338 | 12.095±0.001 | 0.628±0.002 | 0.754±0.002 | Y | Y | ··· |
| F5 | 282 | 12.146±0.001 | 0.622±0.001 | 0.735±0.002 | N | Y | XR,Li,RV,J |
| F3 | 177 | 12.239±0.001 | 0.635±0.002 | 0.770±0.002 | N | Y | ··· |
| F3 | 317 | 12.268±0.001 | 0.678±0.002 | 0.833±0.002 | Y | Y | ··· |
| F2 | 145 | 12.272±0.001 | 0.646±0.002 | 0.768±0.002 | N | Y | Li,RV,J |
| F4 | 178 | 12.274±0.001 | 0.673±0.002 | 0.836±0.002 | Y | Y | ··· |
| F9 | 580 | 12.330±0.001 | 0.574±0.002 | 0.725±0.002 | N | Y | ··· |
| F8 | 38 | 12.342±0.001 | 0.799±0.002 | 0.991±0.002 | Y | N | XR,RV |

Continued on Next Page...

Table A.1 – Continued

| Mosaic Field | Object Number | V | $B-V$ | $V-I_c$ | Phot Mem[a] $[B-V]$ | Phot Mem[a] $[V-I_c]$ | Mem Key[b] |
|---|---|---|---|---|---|---|---|
| F7 | 162 | 12.362±0.001 | 0.731±0.002 | 0.858±0.002 | Y | Y | ··· |
| F8 | 92 | 12.409±0.001 | 0.807±0.002 | 0.925±0.002 | Y | N | ··· |
| F2 | 257 | 12.417±0.001 | 0.708±0.002 | 0.850±0.002 | Y | Y | ··· |
| F2 | 123 | 12.418±0.001 | 0.579±0.002 | 0.729±0.002 | N | Y | ··· |
| F2 | 209 | 12.426±0.001 | 0.658±0.002 | 0.769±0.002 | N | Y | ··· |
| F2 | 373 | 12.456±0.001 | 0.721±0.002 | 0.883±0.002 | Y | N | XR,Li,RV,J |
| F1 | 562 | 12.472±0.001 | 0.610±0.002 | 0.763±0.002 | N | Y | ··· |
| F1 | 530 | 12.518±0.002 | 0.678±0.003 | 0.787±0.003 | N | Y | Li,RV,J |
| F5 | 260 | 12.566±0.001 | 0.755±0.002 | 0.835±0.002 | Y | Y | ··· |
| F1 | 119 | 12.609±0.002 | 0.627±0.003 | 0.756±0.004 | N | Y | ··· |
| F8 | 189 | 12.620±0.002 | 0.763±0.003 | 0.938±0.003 | Y | N | HA,Li,RP |
| F6 | 347 | 12.729±0.002 | 0.835±0.004 | 1.018±0.003 | Y | N | HA,XR,Li,RP |
| F8 | 88 | 12.736±0.002 | 0.632±0.003 | 0.793±0.004 | N | Y | ··· |
| F8 | 292 | 12.754±0.002 | 0.656±0.003 | 0.830±0.004 | N | Y | ··· |
| F9 | 517 | 12.757±0.002 | 0.785±0.004 | 0.972±0.003 | Y | N | ··· |
| F7 | 394 | 12.776±0.001 | 0.762±0.002 | 0.881±0.002 | Y | Y | ··· |
| F6 | 64 | 12.874±0.002 | 0.651±0.004 | 0.807±0.004 | N | Y | ··· |
| F6 | 184 | 12.890±0.002 | 0.656±0.004 | 0.818±0.004 | N | Y | ··· |
| F9 | 118 | 12.890±0.002 | 0.704±0.004 | 0.908±0.004 | N | Y | ··· |
| F5 | 60 | 12.898±0.002 | 0.864±0.004 | 0.921±0.003 | Y | Y | ··· |
| F5 | 317 | 12.901±0.002 | 0.865±0.004 | 0.943±0.003 | Y | Y | ··· |
| F8 | 257 | 12.921±0.002 | 0.847±0.004 | 1.051±0.004 | Y | N | Li,RV,J |
| F1 | 208 | 12.924±0.002 | 0.769±0.004 | 0.888±0.004 | Y | Y | ··· |
| F5 | 26 | 12.964±0.002 | 0.784±0.004 | 0.920±0.003 | Y | Y | RP,RV |
| F1 | 172 | 13.040±0.002 | 0.791±0.004 | 0.875±0.004 | Y | Y | ··· |
| F1 | 427 | 13.069±0.002 | 0.816±0.004 | 0.997±0.004 | Y | Y | Li,RV,J |
| F3 | 207 | 13.072±0.002 | 0.796±0.004 | 0.869±0.004 | Y | Y | ··· |
| F7 | 79 | 13.088±0.002 | 0.688±0.004 | 0.847±0.003 | N | Y | Li,RV,J |
| F9 | 536 | 13.095±0.002 | 0.829±0.004 | 0.991±0.004 | Y | Y | ··· |

Continued on Next Page...

Table A.1 – Continued

| Mosaic Field | Object Number | V | $B-V$ | $V-I_c$ | Phot Mem[a] $[B-V]$ | Phot Mem[a] $[V-I_c]$ | Mem Key[b] |
|---|---|---|---|---|---|---|---|
| F7 | 21 | 13.126±0.002 | 0.859±0.004 | 1.019±0.003 | Y | Y | Li,RP,RV,J |
| F6 | 187 | 13.163±0.002 | 0.667±0.004 | 0.880±0.004 | N | Y | ··· |
| F2 | 213 | 13.218±0.002 | 0.795±0.004 | 0.933±0.004 | N | Y | Li,RV,J |
| F1 | 430 | 13.223±0.002 | 0.843±0.004 | 0.925±0.004 | Y | Y | ··· |
| F4 | 110 | 13.237±0.002 | 0.792±0.004 | 0.888±0.004 | N | Y | ··· |
| F4 | 58 | 13.260±0.002 | 0.835±0.004 | 0.965±0.004 | Y | Y | ··· |
| F4 | 329 | 13.261±0.002 | 0.843±0.004 | 0.944±0.004 | Y | Y | ··· |
| F9 | 421 | 13.264±0.002 | 0.728±0.004 | 0.917±0.004 | N | Y | ··· |
| F8 | 653 | 13.285±0.003 | 99.999±9.999 | 1.014±0.004 | N | Y | ··· |
| F8 | 274 | 13.297±0.003 | 0.738±0.005 | 0.914±0.005 | N | Y | ··· |
| F6 | 267 | 13.339±0.003 | 0.780±0.005 | 0.915±0.005 | N | Y | ··· |
| F6 | 105 | 13.364±0.003 | 1.054±0.007 | 1.141±0.004 | Y | N | ··· |
| F1 | 434 | 13.434±0.003 | 1.044±0.007 | 1.138±0.004 | Y | N | ··· |
| F8 | 222 | 13.440±0.003 | 0.850±0.006 | 1.025±0.005 | N | Y | ··· |
| F5 | 59 | 13.442±0.002 | 1.023±0.005 | 1.126±0.004 | Y | N | ··· |
| F3 | 396 | 13.453±0.002 | 0.868±0.004 | 0.997±0.004 | Y | Y | XR.Li,RV,J |
| F7 | 264 | 13.484±0.002 | 0.904±0.004 | 1.004±0.004 | Y | Y | HA,Li,RP,RV |
| F3 | 350 | 13.507±0.003 | 0.988±0.007 | 1.141±0.005 | Y | N | ··· |
| F6 | 95 | 13.511±0.003 | 0.852±0.006 | 1.013±0.005 | N | Y | Li,RV,J |
| F3 | 139 | 13.512±0.003 | 0.832±0.006 | 0.936±0.005 | N | Y | ··· |
| F3 | 357 | 13.517±0.003 | 0.900±0.007 | 1.102±0.005 | Y | Y | HA,Li,RV,J |
| F4 | 53 | 13.528±0.002 | 0.989±0.005 | 1.164±0.004 | Y | N | Li,RV,J |
| F9 | 476 | 13.538±0.003 | 0.841±0.006 | 0.965±0.005 | N | Y | ··· |
| F3 | 273 | 13.551±0.003 | 0.905±0.007 | 0.970±0.005 | Y | Y | ··· |
| F6 | 380 | 13.552±0.003 | 1.077±0.008 | 1.248±0.004 | Y | N | ··· |
| F2 | 243 | 13.553±0.003 | 0.922±0.007 | 1.000±0.005 | Y | Y | ··· |
| F6 | 351 | 13.586±0.003 | 0.882±0.007 | 0.952±0.005 | N | Y | ··· |
| F6 | 74 | 13.592±0.003 | 0.880±0.007 | 0.961±0.005 | N | Y | ··· |
| F6 | 98 | 13.606±0.003 | 1.044±0.008 | 1.128±0.005 | Y | Y | ··· |

Continued on Next Page...

Table A.1 – Continued

| Mosaic Field | Object Number | V | $B-V$ | $V-I_c$ | Phot Mem[a] $[B-V]$ | Phot Mem[a] $[V-I_c]$ | Mem Key[b] |
|---|---|---|---|---|---|---|---|
| F6 | 330 | 13.627±0.003 | 0.838±0.007 | 0.946±0.005 | N | Y | ··· |
| F9 | 543 | 13.669±0.003 | 0.903±0.008 | 1.059±0.005 | N | Y | ··· |
| F9 | 82 | 13.680±0.003 | 1.093±0.009 | 1.177±0.005 | Y | N | ··· |
| F7 | 42 | 13.685±0.003 | 0.861±0.006 | 0.967±0.004 | N | Y | ··· |
| F9 | 313 | 13.693±0.003 | 0.820±0.007 | 0.972±0.006 | N | Y | ··· |
| F4 | 20 | 13.706±0.003 | 0.881±0.006 | 0.976±0.004 | N | Y | ··· |
| F3 | 395 | 13.716±0.004 | 0.898±0.008 | 1.057±0.006 | N | Y | Li,RP,RV,J |
| F6 | 88 | 13.716±0.004 | 0.904±0.008 | 1.028±0.006 | N | Y | XR,Li,RP,RV ,J |
| F5 | 129 | 13.726±0.003 | 1.141±0.008 | 1.217±0.004 | Y | N | RV |
| F5 | 7 | 13.733±0.003 | 0.907±0.006 | 1.017±0.004 | N | Y | ··· |
| F7 | 15 | 13.768±0.003 | 0.932±0.007 | 1.046±0.005 | N | Y | ··· |
| F3 | 374 | 13.769±0.004 | 0.913±0.008 | 1.020±0.006 | N | Y | ··· |
| F4 | 226 | 13.781±0.003 | 0.881±0.006 | 1.000±0.005 | N | Y | Li,RV,J |
| F1 | 63 | 13.783±0.004 | 0.883±0.008 | 1.110±0.006 | N | Y | ··· |
| F7 | 304 | 13.792±0.003 | 1.089±0.008 | 1.162±0.004 | Y | Y | ··· |
| F6 | 306 | 13.798±0.004 | 1.121±0.010 | 1.209±0.006 | Y | N | ··· |
| F9 | 563 | 13.832±0.004 | 0.920±0.009 | 1.015±0.006 | N | Y | ··· |
| F4 | 57 | 13.838±0.003 | 1.075±0.008 | 1.235±0.004 | Y | N | HA,RV |
| F8 | 237 | 13.841±0.004 | 0.894±0.008 | 1.075±0.006 | N | Y | ··· |
| F5 | 147 | 13.845±0.003 | 0.960±0.007 | 1.097±0.005 | N | Y | ··· |
| F8 | 134 | 13.871±0.004 | 0.949±0.009 | 1.091±0.006 | N | Y | ··· |
| F2 | 366 | 13.874±0.004 | 1.181±0.011 | 1.208±0.006 | Y | N | ··· |
| F1 | 290 | 13.880±0.004 | 1.176±0.011 | 1.259±0.006 | Y | N | ··· |
| F4 | 93 | 13.883±0.003 | 1.143±0.009 | 1.185±0.004 | Y | Y | ··· |
| F7 | 37 | 13.892±0.003 | 1.147±0.009 | 1.229±0.004 | Y | N | ··· |
| F1 | 227 | 13.897±0.004 | 1.073±0.011 | 1.148±0.006 | Y | Y | ··· |
| F3 | 388 | 13.898±0.004 | 0.858±0.009 | 1.026±0.006 | N | Y | ··· |
| F8 | 128 | 13.899±0.004 | 1.062±0.010 | 1.226±0.006 | Y | N | ··· |
| F6 | 18 | 13.899±0.004 | 1.165±0.011 | 1.213±0.006 | Y | N | RV |

Continued on Next Page...

Table A.1 – Continued

| Mosaic Field | Object Number | V | $B-V$ | $V-I_c$ | Phot Mem[a] $[B-V]$ | Phot Mem[a] $[V-I_c]$ | Mem Key[b] |
|---|---|---|---|---|---|---|---|
| F5 | 355 | 13.902±0.002 | 1.050±0.006 | 1.180±0.004 | Y | Y | ··· |
| F4 | 337 | 13.913±0.003 | 1.187±0.009 | 1.383±0.004 | Y | N | RV,J |
| F1 | 303 | 13.924±0.004 | 1.096±0.011 | 1.219±0.006 | Y | N | ··· |
| F8 | 264 | 13.938±0.004 | 0.972±0.010 | 1.127±0.006 | N | Y | RV |
| F5 | 296 | 13.940±0.003 | 0.932±0.007 | 1.081±0.005 | N | Y | XR,Li,RV,J |
| F5 | 163 | 13.955±0.003 | 1.000±0.008 | 1.148±0.005 | Y | Y | ··· |
| F1 | 54 | 13.957±0.004 | 1.062±0.011 | 1.143±0.006 | Y | Y | ··· |
| F7 | 422 | 13.963±0.004 | 0.911±0.008 | 1.050±0.006 | N | Y | ··· |
| F9 | 521 | 13.989±0.004 | 0.954±0.010 | 1.087±0.006 | N | Y | ··· |
| F1 | 187 | 13.989±0.004 | 0.994±0.010 | 1.131±0.006 | N | Y | ··· |
| F6 | 159 | 13.996±0.004 | 1.088±0.011 | 1.293±0.006 | Y | N | ··· |
| F6 | 219 | 14.005±0.004 | 1.153±0.012 | 1.227±0.006 | Y | Y | ··· |
| F1 | 339 | 14.016±0.004 | 1.180±0.012 | 1.218±0.006 | Y | Y | ··· |
| F3 | 24 | 14.022±0.005 | 0.978±0.011 | 1.044±0.008 | N | Y | ··· |
| F1 | 261 | 14.026±0.004 | 1.118±0.012 | 1.294±0.006 | Y | N | ··· |
| F3 | 346 | 14.027±0.004 | 1.138±0.012 | 1.244±0.006 | Y | Y | ··· |
| F1 | 228 | 14.029±0.004 | 0.876±0.010 | 1.168±0.006 | N | Y | ··· |
| F1 | 230 | 14.030±0.004 | 0.876±0.010 | 1.172±0.006 | N | Y | ··· |
| F8 | 112 | 14.038±0.004 | 0.993±0.008 | 1.157±0.005 | N | Y | ··· |
| F7 | 38 | 14.085±0.004 | 1.103±0.010 | 1.115±0.006 | Y | Y | ··· |
| F9 | 582 | 14.117±0.005 | 1.126±0.015 | 1.258±0.008 | Y | Y | ··· |
| F1 | 363 | 14.119±0.005 | 1.045±0.011 | 1.182±0.007 | Y | Y | ··· |
| F9 | 286 | 14.126±0.005 | 1.075±0.012 | 1.220±0.007 | Y | Y | ··· |
| F6 | 317 | 14.141±0.005 | 1.109±0.012 | 1.198±0.007 | Y | Y | ··· |
| F9 | 301 | 14.156±0.005 | 1.169±0.014 | 1.284±0.007 | Y | N | ··· |
| F4 | 149 | 14.185±0.004 | 1.193±0.011 | 1.261±0.006 | Y | Y | RV |
| F7 | 27 | 14.204±0.004 | 1.109±0.011 | 1.218±0.006 | Y | Y | RV |
| F3 | 261 | 14.205±0.005 | 1.195±0.015 | 1.303±0.007 | Y | N | ··· |
| F3 | 50 | 14.222±0.005 | 0.908±0.011 | 1.111±0.008 | N | Y | ··· |

Continued on Next Page...

Table A.1 – Continued

| Mosaic Field | Object Number | V | $B-V$ | $V-I_c$ | Phot Mem[a] $[B-V]$ | Phot Mem[a] $[V-I_c]$ | Mem Key[b] |
|---|---|---|---|---|---|---|---|
| F5 | 89 | 14.229±0.004 | 1.140±0.011 | 1.205±0.006 | Y | Y | ··· |
| F6 | 118 | 14.236±0.005 | 1.081±0.013 | 1.212±0.008 | Y | Y | ··· |
| F5 | 280 | 14.243±0.004 | 1.049±0.010 | 1.094±0.006 | N | Y | Li,RV,J |
| F5 | 348 | 14.244±0.004 | 1.126±0.011 | 1.190±0.006 | Y | Y | ··· |
| F1 | 487 | 14.245±0.005 | 1.089±0.014 | 1.185±0.008 | Y | Y | ··· |
| F3 | 260 | 14.279±0.005 | 1.256±0.017 | 1.395±0.007 | Y | N | ··· |
| F2 | 72 | 14.284±0.006 | 1.158±0.016 | 1.214±0.009 | Y | Y | ··· |
| F9 | 460 | 14.287±0.005 | 1.183±0.015 | 1.330±0.008 | Y | N | ··· |
| F9 | 229 | 14.301±0.005 | 1.031±0.014 | 1.209±0.008 | N | Y | ··· |
| F6 | 15 | 14.305±0.005 | 1.071±0.013 | 1.233±0.008 | N | Y | ··· |
| F5 | 15 | 14.315±0.004 | 1.184±0.013 | 1.244±0.006 | Y | Y | ··· |
| F1 | 237 | 14.337±0.005 | 1.144±0.015 | 1.299±0.008 | Y | Y | ··· |
| F6 | 227 | 14.339±0.006 | 1.094±0.014 | 1.246±0.009 | N | Y | ··· |
| F2 | 376 | 14.357±0.006 | 1.049±0.014 | 1.206±0.009 | N | Y | ··· |
| F4 | 251 | 14.373±0.004 | 1.246±0.013 | 1.327±0.006 | Y | Y | ··· |
| F8 | 312 | 14.373±0.006 | 1.034±0.014 | 1.225±0.009 | N | Y | ··· |
| F9 | 192 | 14.377±0.006 | 0.975±0.014 | 1.189±0.009 | N | Y | ··· |
| F8 | 256 | 14.378±0.006 | 0.966±0.013 | 1.117±0.009 | N | Y | ··· |
| F2 | 236 | 14.380±0.006 | 1.152±0.016 | 1.286±0.009 | Y | Y | ··· |
| F8 | 17 | 14.392±0.006 | 1.266±0.018 | 1.346±0.009 | Y | Y | ··· |
| F4 | 199 | 14.406±0.004 | 1.211±0.013 | 1.185±0.006 | Y | Y | ··· |
| F5 | 179 | 14.407±0.004 | 1.063±0.011 | 1.240±0.006 | N | Y | XR,Li,RP,RV ,J |
| F8 | 196 | 14.412±0.006 | 1.221±0.017 | 1.328±0.009 | Y | Y | ··· |
| F2 | 396 | 14.413±0.006 | 0.957±0.014 | 1.119±0.009 | N | Y | ··· |
| F9 | 106 | 14.418±0.006 | 0.964±0.014 | 1.124±0.009 | N | Y | ··· |
| F7 | 136 | 14.438±0.005 | 1.036±0.012 | 1.161±0.007 | N | Y | ··· |
| F3 | 90 | 14.443±0.007 | 1.230±0.019 | 0.962±0.011 | Y | N | ··· |
| F9 | 356 | 14.449±0.006 | 1.180±0.018 | 1.410±0.009 | Y | N | ··· |
| F8 | 89 | 14.451±0.006 | 1.134±0.016 | 1.280±0.009 | Y | Y | ··· |

Continued on Next Page...

Table A.1 – Continued

| Mosaic Field | Object Number | V | $B-V$ | $V-I_c$ | Phot Mem[a] $[B-V]$ | Phot Mem[a] $[V-I_c]$ | Mem Key[b] |
|---|---|---|---|---|---|---|---|
| F8 | 61 | 14.452±0.006 | 1.102±0.016 | 1.277±0.009 | N | Y | RV |
| F5 | 11 | 14.458±0.005 | 1.124±0.013 | 1.246±0.007 | Y | Y | ··· |
| F8 | 33 | 14.468±0.006 | 1.204±0.019 | 1.297±0.009 | Y | Y | ··· |
| F6 | 59 | 14.476±0.006 | 1.252±0.019 | 1.274±0.009 | Y | Y | RV |
| F4 | 212 | 14.478±0.005 | 1.335±0.016 | 1.371±0.007 | N | Y | ··· |
| F9 | 185 | 14.478±0.006 | 1.269±0.020 | 1.483±0.009 | Y | N | ··· |
| F7 | 39 | 14.480±0.005 | 1.028±0.013 | 1.164±0.007 | N | Y | ··· |
| F3 | 70 | 14.487±0.006 | 1.171±0.018 | 1.326±0.009 | Y | Y | ··· |
| F5 | 45 | 14.488±0.005 | 1.206±0.014 | 1.221±0.007 | Y | Y | ··· |
| F9 | 482 | 14.491±0.006 | 1.060±0.017 | 1.203±0.009 | N | Y | ··· |
| F8 | 35 | 14.495±0.006 | 1.252±0.019 | 1.282±0.009 | Y | Y | ··· |
| F5 | 20 | 14.496±0.005 | 1.405±0.017 | 1.385±0.006 | N | Y | ··· |
| F7 | 395 | 14.515±0.005 | 1.153±0.014 | 1.235±0.007 | Y | Y | ··· |
| F1 | 321 | 14.533±0.006 | 1.193±0.019 | 1.304±0.009 | Y | Y | ··· |
| F9 | 406 | 14.539±0.007 | 0.908±0.016 | 1.208±0.010 | N | Y | RV |
| F9 | 47 | 14.549±0.007 | 1.236±0.020 | 1.330±0.010 | Y | Y | ··· |
| F9 | 498 | 14.562±0.007 | 1.128±0.018 | 1.314±0.010 | N | Y | ··· |
| F4 | 51 | 14.563±0.005 | 1.159±0.015 | 1.335±0.007 | Y | Y | ··· |
| F6 | 224 | 14.572±0.007 | 1.088±0.018 | 1.157±0.011 | N | Y | ··· |
| F6 | 154 | 14.573±0.007 | 1.098±0.018 | 1.254±0.010 | N | Y | ··· |
| F4 | 286 | 14.575±0.005 | 1.245±0.016 | 1.297±0.007 | Y | Y | ··· |
| F6 | 374 | 14.584±0.007 | 1.103±0.018 | 1.245±0.010 | N | Y | ··· |
| F5 | 304 | 14.589±0.005 | 1.119±0.014 | 1.182±0.008 | N | Y | ··· |
| F1 | 272 | 14.590±0.007 | 1.191±0.020 | 1.320±0.010 | Y | Y | ··· |
| F2 | 19 | 14.591±0.007 | 1.067±0.018 | 1.163±0.011 | N | Y | ··· |
| F2 | 397 | 14.593±0.007 | 1.361±0.022 | 1.431±0.009 | N | Y | ··· |
| F7 | 336 | 14.601±0.005 | 1.129±0.015 | 1.382±0.007 | N | Y | ··· |
| F1 | 58 | 14.603±0.007 | 1.109±0.019 | 1.171±0.011 | N | Y | ··· |
| F9 | 204 | 14.609±0.007 | 0.969±0.018 | 1.277±0.011 | N | Y | ··· |

Continued on Next Page...

Table A.1 – Continued

| Mosaic Field | Object Number | V | $B-V$ | $V-I_c$ | Phot Mem[a] $[B-V]$ | Phot Mem[a] $[V-I_c]$ | Mem Key[b] |
|---|---|---|---|---|---|---|---|
| F9 | 119 | 14.618±0.007 | 1.058±0.018 | 1.210±0.011 | N | Y | ··· |
| F5 | 83 | 14.619±0.005 | 1.451±0.023 | 1.346±0.007 | N | Y | ··· |
| F5 | 137 | 14.629±0.006 | 1.224±0.016 | 1.259±0.009 | Y | Y | ··· |
| F4 | 165 | 14.636±0.005 | 1.189±0.016 | 1.282±0.007 | Y | Y | ··· |
| F8 | 111 | 14.638±0.008 | 1.165±0.021 | 1.312±0.011 | Y | Y | Li |
| F4 | 68 | 14.642±0.006 | 1.081±0.015 | 1.229±0.009 | N | Y | ··· |
| F7 | 297 | 14.646±0.006 | 1.181±0.017 | 1.247±0.009 | Y | Y | ··· |
| F5 | 52 | 14.652±0.006 | 1.218±0.017 | 1.268±0.009 | Y | Y | ··· |
| F8 | 303 | 14.652±0.007 | 1.169±0.020 | 1.378±0.010 | Y | Y | ··· |
| F7 | 287 | 14.653±0.006 | 1.107±0.015 | 1.201±0.009 | N | Y | ··· |
| F1 | 209 | 14.655±0.007 | 1.015±0.018 | 1.246±0.011 | N | Y | ··· |
| F1 | 351 | 14.657±0.007 | 1.028±0.018 | 1.198±0.011 | N | Y | ··· |
| F1 | 79 | 14.664±0.007 | 1.155±0.021 | 1.189±0.011 | N | Y | ··· |
| F4 | 308 | 14.669±0.006 | 1.267±0.018 | 1.350±0.008 | Y | Y | ··· |
| F9 | 164 | 14.669±0.008 | 1.054±0.021 | 1.198±0.011 | N | Y | ··· |
| F6 | 119 | 14.674±0.007 | 1.159±0.020 | 1.240±0.011 | N | Y | Li |
| F4 | 41 | 14.686±0.006 | 1.164±0.016 | 1.292±0.009 | N | Y | ··· |
| F7 | 314 | 14.696±0.006 | 1.168±0.017 | 1.279±0.009 | N | Y | ··· |
| F9 | 244 | 14.696±0.007 | 1.276±0.025 | 1.307±0.011 | Y | Y | ··· |
| F2 | 77 | 14.699±0.007 | 1.106±0.021 | 1.264±0.011 | N | Y | ··· |
| F5 | 115 | 14.708±0.006 | 1.244±0.018 | 1.310±0.008 | Y | Y | ··· |
| F5 | 79 | 14.716±0.006 | 1.137±0.016 | 1.263±0.009 | N | Y | ··· |
| F8 | 176 | 14.729±0.008 | 1.064±0.021 | 1.227±0.012 | N | Y | ··· |
| F4 | 17 | 14.735±0.006 | 1.130±0.017 | 1.279±0.009 | N | Y | ··· |
| F8 | 286 | 14.751±0.008 | 1.137±0.021 | 1.361±0.011 | N | Y | ··· |
| F7 | 292 | 14.761±0.006 | 1.084±0.016 | 1.211±0.009 | N | Y | ··· |
| F8 | 34 | 14.772±0.008 | 1.208±0.023 | 1.293±0.011 | Y | Y | ··· |
| F9 | 409 | 14.778±0.008 | 1.036±0.021 | 1.237±0.012 | N | Y | ··· |
| F2 | 380 | 14.794±0.008 | 1.146±0.022 | 1.230±0.012 | N | Y | ··· |

Continued on Next Page...

Table A.1 – Continued

| Mosaic Field | Object Number | V | $B-V$ | $V-I_c$ | Phot Mem[a] $[B-V]$ | Phot Mem[a] $[V-I_c]$ | Mem Key[b] |
|---|---|---|---|---|---|---|---|
| F3 | 265 | 14.800±0.008 | 1.252±0.026 | 1.438±0.011 | Y | Y | ··· |
| F1 | 435 | 14.811±0.008 | 1.090±0.022 | 1.223±0.012 | N | Y | ··· |
| F8 | 248 | 14.821±0.008 | 1.282±0.025 | 1.407±0.011 | Y | Y | ··· |
| F4 | 338 | 14.825±0.005 | 1.158±0.013 | 1.232±0.007 | N | Y | ··· |
| F9 | 144 | 14.826±0.008 | 1.289±0.027 | 1.351±0.012 | Y | Y | ··· |
| F2 | 431 | 14.827±0.008 | 1.119±0.023 | 1.258±0.012 | N | Y | ··· |
| F3 | 16 | 14.836±0.008 | 1.099±0.022 | 1.259±0.012 | N | Y | ··· |
| F8 | 277 | 14.841±0.008 | 1.189±0.024 | 1.421±0.011 | N | Y | ··· |
| F9 | 206 | 14.845±0.009 | 1.114±0.025 | 1.319±0.013 | N | Y | ··· |
| F5 | 66 | 14.849±0.006 | 1.341±0.022 | 1.434±0.009 | Y | Y | ··· |
| F9 | 260 | 14.849±0.008 | 1.184±0.024 | 1.302±0.012 | N | Y | ··· |
| F7 | 386 | 14.857±0.007 | 1.183±0.020 | 1.299±0.010 | N | Y | ··· |
| F6 | 388 | 14.865±0.008 | 1.157±0.023 | 1.262±0.012 | N | Y | ··· |
| F8 | 143 | 14.874±0.009 | 1.270±0.028 | 1.334±0.013 | Y | Y | ··· |
| F6 | 316 | 14.879±0.008 | 1.116±0.023 | 1.242±0.012 | N | Y | ··· |
| F9 | 259 | 14.879±0.009 | 1.217±0.027 | 1.305±0.013 | Y | Y | ··· |
| F8 | 242 | 14.882±0.008 | 1.149±0.023 | 1.440±0.011 | N | Y | ··· |
| F5 | 82 | 14.886±0.007 | 1.304±0.022 | 1.280±0.010 | Y | Y | ··· |
| F8 | 135 | 14.889±0.008 | 1.414±0.031 | 1.477±0.011 | N | Y | ··· |
| F3 | 83 | 14.891±0.009 | 1.359±0.030 | 1.398±0.013 | Y | Y | ··· |
| F8 | 154 | 14.899±0.008 | 1.242±0.027 | 1.420±0.011 | Y | Y | ··· |
| F7 | 424 | 14.902±0.008 | 1.358±0.026 | 1.388±0.011 | Y | Y | ··· |
| F2 | 162 | 14.910±0.009 | 1.272±0.029 | 1.359±0.013 | Y | Y | ··· |
| F5 | 41 | 14.914±0.007 | 1.297±0.022 | 1.325±0.010 | Y | Y | ··· |
| F5 | 190 | 14.916±0.007 | 1.355±0.023 | 1.471±0.009 | Y | Y | XR,Li |
| F8 | 83 | 14.921±0.009 | 1.181±0.026 | 1.302±0.013 | N | Y | ··· |
| F3 | 161 | 14.921±0.009 | 1.328±0.031 | 1.399±0.013 | Y | Y | ··· |
| F7 | 175 | 14.924±0.007 | 1.339±0.024 | 1.403±0.009 | Y | Y | ··· |
| F1 | 361 | 14.948±0.010 | 1.184±0.028 | 1.312±0.013 | N | Y | ··· |

Continued on Next Page...

Table A.1 – Continued

| Mosaic Field | Object Number | V | $B-V$ | $V-I_c$ | Phot Mem[a] $[B-V]$ | Phot Mem[a] $[V-I_c]$ | Mem Key[b] |
|---|---|---|---|---|---|---|---|
| F2 | 90 | 14.950±0.010 | 0.977±0.023 | 1.381±0.014 | N | Y | ··· |
| F4 | 18 | 14.951±0.008 | 1.301±0.025 | 1.372±0.011 | Y | Y | ··· |
| F8 | 699 | 14.954±0.009 | 99.999±9.999 | 1.428±0.012 | N | Y | ··· |
| F7 | 25 | 14.956±0.007 | 1.118±0.020 | 1.268±0.010 | N | Y | ··· |
| F9 | 281 | 14.956±0.010 | 1.208±0.030 | 1.421±0.013 | N | Y | Li,RV,J |
| F6 | 368 | 14.963±0.010 | 1.245±0.030 | 1.350±0.013 | Y | Y | ··· |
| F3 | 143 | 14.969±0.009 | 1.384±0.033 | 1.453±0.012 | Y | Y | ··· |
| F7 | 66 | 14.976±0.007 | 1.239±0.023 | 1.260±0.010 | Y | N | Li |
| F3 | 155 | 14.977±0.010 | 1.149±0.029 | 1.285±0.015 | N | Y | ··· |
| F5 | 10 | 14.978±0.008 | 1.167±0.022 | 1.285±0.011 | N | Y | Li |
| F9 | 183 | 14.981±0.010 | 1.271±0.032 | 1.623±0.013 | Y | N | ··· |
| F2 | 42 | 14.988±0.010 | 1.357±0.034 | 1.476±0.013 | Y | Y | ··· |
| F9 | 67 | 14.996±0.010 | 1.266±0.033 | 1.345±0.014 | Y | Y | ··· |
| F8 | 217 | 15.000±0.009 | 1.337±0.031 | 1.486±0.012 | Y | Y | ··· |
| F8 | 304 | 15.020±0.010 | 1.365±0.034 | 1.437±0.013 | Y | Y | ··· |
| F4 | 249 | 15.022±0.008 | 1.428±0.028 | 1.538±0.010 | N | Y | ··· |
| F3 | 65 | 15.045±0.010 | 1.226±0.032 | 1.549±0.013 | N | Y | HA,Li,RV,J |
| F8 | 249 | 15.084±0.010 | 1.173±0.029 | 1.395±0.014 | N | Y | ··· |
| F6 | 401 | 15.110±0.010 | 1.187±0.031 | 1.327±0.014 | N | Y | ··· |
| F2 | 301 | 15.111±0.010 | 1.149±0.031 | 1.331±0.014 | N | Y | ··· |
| F7 | 396 | 15.126±0.008 | 1.305±0.029 | 1.489±0.011 | Y | Y | ··· |
| F3 | 383 | 15.129±0.011 | 1.404±0.041 | 1.514±0.014 | Y | Y | ··· |
| F7 | 155 | 15.142±0.008 | 1.278±0.026 | 1.307±0.011 | Y | N | ··· |
| F3 | 61 | 15.149±0.011 | 1.217±0.033 | 1.390±0.015 | N | Y | ··· |
| F5 | 191 | 15.163±0.008 | 1.304±0.027 | 1.357±0.011 | Y | Y | ··· |
| F8 | 79 | 15.176±0.011 | 1.221±0.034 | 1.397±0.015 | N | Y | ··· |
| F8 | 313 | 15.186±0.011 | 1.351±0.040 | 1.495±0.015 | Y | Y | ··· |
| F3 | 380 | 15.197±0.012 | 1.407±0.043 | 1.425±0.016 | Y | Y | ··· |
| F1 | 277 | 15.218±0.011 | 1.248±0.036 | 1.352±0.016 | N | Y | ··· |

Continued on Next Page...

Table A.1 – Continued

| Mosaic Field | Object Number | V | $B-V$ | $V-I_c$ | Phot Mem[a] $[B-V]$ | Phot Mem[a] $[V-I_c]$ | Mem Key[b] |
|---|---|---|---|---|---|---|---|
| F6 | 279 | 15.263±0.012 | 1.111±0.033 | 1.375±0.016 | N | Y | ··· |
| F3 | 115 | 15.264±0.013 | 1.278±0.040 | 1.395±0.017 | Y | Y | ··· |
| F7 | 329 | 15.280±0.010 | 1.469±0.036 | 1.554±0.012 | Y | Y | ··· |
| F8 | 95 | 15.285±0.012 | 1.313±0.042 | 1.342±0.017 | Y | N | ··· |
| F9 | 410 | 15.295±0.013 | 1.236±0.039 | 1.397±0.018 | N | Y | ··· |
| F5 | 205 | 15.304±0.009 | 1.301±0.031 | 1.363±0.013 | Y | N | ··· |
| F3 | 342 | 15.324±0.014 | 1.568±0.059 | 1.611±0.017 | N | Y | ··· |
| F2 | 79 | 15.328±0.012 | 1.502±0.050 | 1.775±0.015 | Y | Y | ··· |
| F5 | 76 | 15.340±0.012 | 1.372±0.042 | 1.887±0.014 | Y | N | ··· |
| F7 | 282 | 15.352±0.010 | 1.339±0.035 | 1.345±0.014 | Y | N | ··· |
| F8 | 290 | 15.367±0.013 | 1.252±0.040 | 1.520±0.017 | N | Y | ··· |
| F5 | 77 | 15.379±0.012 | 1.337±0.042 | 1.925±0.014 | Y | N | ··· |
| F9 | 418 | 15.380±0.013 | 1.177±0.040 | 1.404±0.018 | N | Y | ··· |
| F8 | 174 | 15.389±0.013 | 1.245±0.042 | 1.534±0.018 | N | Y | ··· |
| F8 | 278 | 15.392±0.013 | 1.268±0.042 | 1.462±0.018 | N | Y | ··· |
| F7 | 88 | 15.411±0.011 | 1.516±0.043 | 1.882±0.013 | Y | N | HA,RV,J |
| F3 | 702 | 15.417±0.014 | 99.999±9.999 | 1.486±0.018 | N | Y | ··· |
| F7 | 135 | 15.439±0.011 | 1.381±0.041 | 1.608±0.014 | Y | Y | ··· |
| F5 | 25 | 15.444±0.010 | 1.379±0.037 | 1.557±0.013 | Y | Y | ··· |
| F5 | 330 | 15.482±0.011 | 1.325±0.040 | 1.452±0.014 | Y | Y | ··· |
| F8 | 133 | 15.482±0.014 | 1.046±0.036 | 1.462±0.019 | N | Y | ··· |
| F4 | 318 | 15.498±0.013 | 1.610±0.055 | 1.712±0.015 | N | Y | ··· |
| F8 | 742 | 15.504±0.015 | 99.999±9.999 | 1.482±0.020 | N | Y | ··· |
| F2 | 381 | 15.510±0.014 | 1.552±0.061 | 1.754±0.017 | N | Y | ··· |
| F7 | 230 | 15.513±0.012 | 1.396±0.043 | 1.488±0.015 | Y | Y | ··· |
| F1 | 457 | 15.585±0.016 | 1.292±0.051 | 1.551±0.021 | N | Y | ··· |
| F4 | 686 | 15.600±0.012 | 99.999±9.999 | 1.926±0.014 | N | Y | ··· |
| F8 | 153 | 15.620±0.016 | 1.427±0.064 | 1.256±0.024 | Y | N | ··· |
| F7 | 401 | 15.682±0.013 | 1.407±0.051 | 1.457±0.017 | Y | N | ··· |

Continued on Next Page...

Table A.1 – Continued

| Mosaic Field | Object Number | V | $B-V$ | $V-I_c$ | Phot Mem[a] $[B-V]$ | Phot Mem[a] $[V-I_c]$ | Mem Key[b] |
|---|---|---|---|---|---|---|---|
| F2 | 823 | 15.731±0.018 | 99.999±9.999 | 1.683±0.023 | N | Y | ··· |
| F2 | 267 | 15.843±0.019 | 1.528±0.081 | 1.850±0.023 | Y | Y | ··· |
| F7 | 351 | 15.849±0.015 | 1.524±0.066 | 1.895±0.018 | Y | Y | ··· |
| F2 | 278 | 15.854±0.019 | 0.774±0.042 | 1.629±0.024 | N | Y | ··· |
| F7 | 620 | 15.873±0.016 | 99.999±9.999 | 1.810±0.019 | N | Y | ··· |
| F7 | 242 | 15.936±0.017 | 1.741±0.090 | 2.001±0.019 | N | Y | ··· |
| F9 | 316 | 15.988±0.022 | 1.545±0.098 | 1.965±0.026 | Y | Y | ··· |
| F6 | 111 | 15.993±0.023 | 1.398±0.084 | 1.780±0.027 | N | Y | HA,RV,J |
| F1 | 358 | 16.001±0.022 | 1.486±0.096 | 1.490±0.030 | Y | N | ··· |
| F7 | 355 | 16.030±0.018 | 1.361±0.067 | 1.942±0.021 | N | Y | ··· |
| F7 | 419 | 16.032±0.018 | 1.481±0.075 | 1.647±0.022 | Y | N | ··· |
| F7 | 739 | 16.042±0.019 | 99.999±9.999 | 1.955±0.021 | N | Y | ··· |
| F1 | 499 | 16.081±0.025 | 1.407±0.095 | 1.745±0.030 | N | Y | ··· |
| F3 | 353 | 16.088±0.026 | 1.470±0.100 | 1.719±0.031 | Y | Y | ··· |
| F7 | 392 | 16.124±0.020 | 1.416±0.077 | 1.829±0.023 | N | Y | ··· |
| F9 | 214 | 16.212±0.028 | 1.387±0.111 | 1.857±0.033 | N | Y | ··· |
| F4 | 591 | 16.236±0.021 | 99.999±9.999 | 1.877±0.024 | N | Y | RV,J |
| F1 | 317 | 16.256±0.028 | 1.577±0.127 | 1.708±0.034 | Y | N | ··· |
| F9 | 157 | 16.358±0.032 | 1.607±0.155 | 1.430±0.043 | Y | N | ··· |
| F2 | 822 | 16.365±0.033 | 99.999±9.999 | 2.306±0.036 | N | Y | ··· |
| F2 | 220 | 16.420±0.033 | 1.425±0.128 | 2.023±0.037 | N | Y | HA,RV,J |
| F4 | 461 | 16.611±0.029 | 99.999±9.999 | 2.388±0.031 | N | Y | ··· |
| F9 | 270 | 16.651±0.040 | 1.597±0.189 | 1.653±0.049 | Y | N | ··· |
| F5 | 394 | 16.690±0.031 | 99.999±9.999 | 2.132±0.034 | N | Y | RV |
| F9 | 34 | 16.710±0.044 | 1.434±0.175 | 2.173±0.048 | N | Y | ··· |
| F4 | 437 | 16.716±0.032 | 99.999±9.999 | 2.079±0.035 | N | Y | HA,RV,J |
| F4 | 613 | 16.819±0.036 | 99.999±9.999 | 2.475±0.038 | N | Y | ··· |
| F3 | 585 | 16.844±0.048 | 99.999±9.999 | 2.094±0.053 | N | Y | ··· |
| F5 | 472 | 16.910±0.037 | 99.999±9.999 | 2.165±0.040 | N | Y | HA,RV,J |

Continued on Next Page...

Table A.1 – Continued

| Mosaic Field | Object Number | V | $B-V$ | $V-I_c$ | Phot Mem[a] $[B-V]$ | Phot Mem[a] $[V-I_c]$ | Mem Key[b] |
|---|---|---|---|---|---|---|---|
| F7 | 512 | 16.935±0.042 | 99.999±9.999 | 2.252±0.045 | N | Y | ··· |
| F8 | 538 | 16.953±0.051 | 99.999±9.999 | 2.153±0.056 | N | Y | ··· |
| F1 | 882 | 16.961±0.051 | 99.999±9.999 | 2.162±0.056 | N | Y | ··· |
| F5 | 521 | 17.062±0.044 | 99.999±9.999 | 2.294±0.047 | N | Y | HA,RV,J |
| F3 | 563 | 17.166±0.066 | 99.999±9.999 | 2.377±0.071 | N | Y | ··· |
| F9 | 636 | 17.224±0.068 | 99.999±9.999 | 2.331±0.073 | N | Y | ··· |
| F2 | 780 | 17.279±0.069 | 99.999±9.999 | 2.354±0.074 | N | Y | ··· |
| F7 | 670 | 17.349±0.056 | 99.999±9.999 | 2.576±0.059 | N | Y | HA,RV,J |
| F9 | 790 | 17.367±0.077 | 99.999±9.999 | 2.663±0.080 | N | Y | ··· |
| F2 | 586 | 17.497±0.084 | 99.999±9.999 | 2.574±0.088 | N | Y | ··· |
| F8 | 364 | 17.530±0.089 | 99.999±9.999 | 2.622±0.093 | N | Y | HA,J |
| F9 | 684 | 17.545±0.091 | 99.999±9.999 | 2.574±0.096 | N | Y | ··· |
| F9 | 445 | 17.566±0.096 | 1.677±0.487 | 1.165±0.147 | Y | N | ··· |
| F3 | 770 | 17.603±0.072 | 99.999±9.999 | 2.686±0.075 | N | Y | HA,RV,J |
| F6 | 511 | 17.625±0.095 | 99.999±9.999 | 2.491±0.101 | N | Y | ··· |
| F8 | 395 | 17.651±0.102 | 99.999±9.999 | 2.516±0.107 | N | Y | HA,XR,RV,J |
| F5 | 632 | 17.721±0.077 | 99.999±9.999 | 2.734±0.080 | N | Y | ··· |
| F6 | 650 | 17.786±0.111 | 99.999±9.999 | 2.465±0.118 | N | Y | ··· |
| F2 | 568 | 17.806±0.111 | 99.999±9.999 | 2.782±0.115 | N | Y | ··· |
| F4 | 486 | 17.828±0.093 | 99.999±9.999 | 2.824±0.096 | N | Y | ··· |
| F5 | 515 | 17.851±0.090 | 99.999±9.999 | 2.741±0.093 | N | Y | HA,RV,J |
| F8 | 550 | 17.872±0.119 | 99.999±9.999 | 2.839±0.123 | N | Y | HA,RV,J |
| F4 | 459 | 17.893±0.094 | 99.999±9.999 | 2.577±0.098 | N | Y | HA,RV,J |
| F1 | 972 | 17.944±0.133 | 99.999±9.999 | 2.541±0.140 | N | Y | ··· |
| F7 | 772 | 17.962±0.110 | 99.999±9.999 | 2.608±0.114 | N | Y | ··· |
| F6 | 728 | 18.014±0.135 | 99.999±9.999 | 2.655±0.141 | N | Y | ··· |
| F7 | 809 | 18.053±0.113 | 99.999±9.999 | 2.917±0.116 | N | Y | ··· |
| F2 | 685 | 18.105±0.148 | 99.999±9.999 | 2.586±0.155 | N | Y | ··· |
| F1 | 728 | 18.189±0.164 | 99.999±9.999 | 2.594±0.172 | N | Y | ··· |

Continued on Next Page...

Table A.1 – Continued

| Mosaic Field | Object Number | V | $B-V$ | $V-I_c$ | Phot Mem[a] $[B-V]$ | Phot Mem[a] $[V-I_c]$ | Mem Key[b] |
|---|---|---|---|---|---|---|---|
| F1 | 639 | 18.294±0.175 | 99.999±9.999 | 2.701±0.183 | N | Y | ··· |
| F8 | 537 | 18.341±0.173 | 99.999±9.999 | 3.048±0.177 | N | Y | HA |
| F7 | 766 | 18.498±0.169 | 99.999±9.999 | 3.064±0.172 | N | Y | ··· |
| F3 | 615 | 18.637±0.237 | 99.999±9.999 | 2.967±0.243 | N | Y | ··· |
| F4 | 517 | 18.763±0.210 | 99.999±9.999 | 2.926±0.215 | N | Y | ··· |
| F1 | 853 | 18.794±0.279 | 99.999±9.999 | 2.782±0.288 | N | Y | ··· |
| F4 | 447 | 19.151±0.302 | 99.999±9.999 | 2.840±0.309 | N | Y | ··· |
| F6 | 506 | 19.317±0.434 | 99.999±9.999 | 3.319±0.439 | N | Y | ··· |
| F9 | 862 | 19.715±0.659 | 99.999±9.999 | 3.441±0.665 | N | Y | ··· |
| F4 | 720 | 19.998±0.648 | 99.999±9.999 | 3.709±0.651 | N | Y | HA |
| F9 | 847 | 20.460±1.403 | 99.999±9.999 | 3.307±1.420 | N | Y | ··· |
| F3 | 637 | 20.967±2.015 | 99.999±9.999 | 3.384±2.035 | N | Y | ··· |

*Note* — Only a few rows are displayed here to show the content of the table, the full table is available in electronic form. Magnitudes, colors, and uncertainties given as 99.999 or 9.999 indicate that the value is undetermined.

[a] Point lies within its photometric uncertainty of the isochrone using the specified color.

[b] Ancillary membership criterion. See text for source references. Li = Lithium absorption, XR = X-ray emission, H = H$\alpha$ emission, RV = Radial Velocity, RP = detected rapid rotation period, J = listed as member in Jeffries et al. (2009a), and '...' = photometric member only.

# Appendix B

## BLANCO 1 X-RAY SOURCE CATALOG

Table B.1: Blanco 1 X-ray Source Catalog

| ID[a] | R.A.[b] [HH:MM:SS] | Dec.[b] [DD:MM:SS] | $V_0$[c] | $(V-I_c)_0$[c] | $(B-V)_0$[c] | ROSAT $LogL_x$[d] | ROSAT $Log\ L_x/L_{bol}$ | XMM-Newton $LogL_x$[d] | XMM-Newton $Log\ L_x/L_{bol}$ | $\mu_\alpha \cos\delta$[e] | $\mu_\delta$[e] | $P_\mu$[e] | P.M.[f] Mem. |
|---|---|---|---|---|---|---|---|---|---|---|---|---|---|
| ZS35 | 00:01:39.85 | -30:04:38.4 | 14.78±0.022 | 1.45±0.027 | 1.24±0.070 | 29.81 | -2.84 | ··· | ··· | 22.0 | 1.7 | 60 | Y |
| ZS58 | 00:01:46.46 | -29:46:38.7 | 12.32±0.003 | 0.84±0.005 | 0.73±0.006 | 29.78 | -3.59 | ··· | ··· | 20.8 | 2.5 | 86 | Y |
| ZS37 | 00:01:53.42 | -30:06:12.9 | 15.74±0.052 | 1.85±0.057 | ··· | 29.25 | -3.26 | 29.49 | -3.02 | 22.3 | 3.0 | 58 | Y |
| ZS38 | 00:01:54.44 | -30:07:41.8 | 13.86±0.010 | 1.33±0.013 | 1.03±0.025 | 29.82 | -3.06 | 29.82 | -3.07 | 22.0 | 2.4 | 86 | Y |
| ZS40 | 00:01:56.92 | -30:12:07.9 | 15.44±0.039 | 1.67±0.045 | ··· | 29.41 | -3.15 | 29.05 | -3.51 | 22.7 | 2.6 | 54 | Y |
| BLX-7 | 00:02:00.80 | -29:59:17.4 | 12.71±0.004 | 0.89±0.006 | 0.83±0.008 | 29.38 | -3.86 | 29.65 | -3.60 | 21.5 | 1.9 | 80 | Y |
| ZS43 | 00:02:03.69 | -30:10:24.9 | 15.20±0.033 | 1.62±0.039 | ··· | 29.53 | -3.11 | 28.37 | -4.27 | 22.8 | 4.0 | 54 | Y |
| ZS42 | 00:02:04.21 | -30:10:34.4 | 14.17±0.013 | 1.24±0.018 | 1.06±0.035 | 29.53 | -3.24 | 29.43 | -3.35 | 21.8 | 3.1 | 89 | Y |
| BLX-12[g] | 00:02:07.66 | -30:04:42.6 | 18.06±0.414 | 2.97±0.420 | ··· | 28.88 | -3.22 | 29.24 | -2.86 | ··· | ··· | ··· | NA |
| ZS44[g] | 00:02:14.69 | -29:49:04.2 | 13.45±0.007 | 1.06±0.010 | 0.93±0.016 | 29.55 | -3.45 | 29.73 | -3.27 | 22.1 | 3.0 | 92 | Y |
| ZS45 | 00:02:18.55 | -29:51:08.5 | 12.91±0.006 | 0.92±0.008 | 0.84±0.013 | 29.16 | -4.01 | 29.54 | -3.63 | 22.1 | 2.0 | 84 | Y |
| ZS46 | 00:02:19.73 | -29:56:07.5 | 14.25±0.014 | 1.49±0.017 | 1.28±0.044 | 29.42 | -3.47 | 29.74 | -3.15 | 20.1 | 1.5 | 16 | Y |
| ZS48 | 00:02:21.63 | -30:08:21.6 | 10.69±0.001 | 0.53±0.002 | 0.44±0.001 | 29.81 | -4.17 | 29.93 | -4.04 | 20.7 | 3.3 | 90 | Y |
| BLX-15[g] | 00:02:22.90 | -30:02:53.2 | 17.15±0.184 | 2.92±0.187 | ··· | 29.03 | -3.41 | 29.15 | -3.29 | ··· | ··· | ··· | NA |
| BLX-16[g] | 00:02:23.63 | -29:50:39.8 | 16.03±0.066 | 2.06±0.071 | ··· | 29.02 | -3.46 | 29.08 | -3.40 | 19.3 | 5.6 | 03 | Y |
| ZS53 | 00:02:24.26 | -30:09:09.0 | 16.16±0.074 | 2.05±0.079 | ··· | ··· | ··· | 29.30 | -3.13 | 20.3 | -0.7 | 01 | Y |
| PMS04-94 | 00:02:25.48 | -29:59:17.6 | 15.98±0.065 | 1.15±0.087 | 1.18±0.195 | ··· | ··· | 28.37 | -3.76 | 15.0 | 20.5 | 00 | N |
| BLX-17 | 00:02:25.89 | -29:52:39.2 | 16.56±0.105 | 2.21±0.111 | ··· | 29.04 | -3.30 | 29.45 | -2.89 | 16.8 | 10.9 | 00 | N |

Continued on Next Page...

Table B.1 – Continued

| ID[a] | R.A.[b] [HH:MM:SS] | Dec.[b] [DD:MM:SS] | $V_0$[c] | $(V-I_c)_0$[c] | $(B-V)_0$[c] | ROSAT $LogL_x$[d] | ROSAT $Log\ L_x/L_{bol}$ | XMM-Newton $LogL_x$[d] | XMM-Newton $Log\ L_x/L_{bol}$ | $\mu_\alpha \cos\delta$[e] | $\mu_\delta$[e] | $P_\mu$[e] | P.M.[f] Mem. |
|---|---|---|---|---|---|---|---|---|---|---|---|---|---|
| ZS54 | 00:02:28.19 | -30:04:43.5 | 12.98±0.005 | 1.11±0.007 | 0.99±0.011 | 29.72 | -3.49 | 29.66 | -3.55 | 21.8 | 2.5 | 90 | Y |
| ZS61 | 00:02:34.83 | -30:05:25.5 | 13.70±0.008 | 1.16±0.011 | 0.90±0.019 | 29.96 | -2.92 | 29.85 | -3.03 | 21.3 | 2.1 | 80 | Y |
| ZS62[h] | 00:02:35.46 | -30:07:02.0 | 12.48±0.003 | 0.85±0.005 | 0.75±0.006 | 29.42 | -3.89 | 29.37 | -3.94 | 21.2 | 2.9 | 93 | Y |
| ZS60[g] | 00:02:41.79 | -29:58:53.2 | 15.55±0.043 | 2.06±0.046 | 1.30±0.147 | 29.10 | -3.57 | 28.70 | -3.97 | -17.8 | -12.0 | 00 | N |
| PMS04-190 | 00:02:48.22 | -29:46:34.9 | 13.75±0.009 | 1.13±0.013 | 1.00±0.022 | ··· | ··· | 29.20 | -3.71 | 20.9 | 3.2 | 86 | Y |
| BLX-26 | 00:02:51.52 | -29:54:49.4 | 16.63±0.119 | 2.11±0.127 | ··· | 29.11 | -3.15 | 28.79 | -3.47 | 18.5 | 3.1 | 04 | Y |
| ZS76 | 00:02:56.38 | -30:04:44.8 | 12.39±0.003 | 0.97±0.004 | 0.86±0.007 | 30.22 | -3.16 | 30.63 | -2.75 | 21.6 | 3.2 | 95 | Y |
| BLX-32 | 00:02:59.65 | -29:52:52.2 | 15.82±0.055 | 2.23±0.058 | ··· | 28.84 | -3.79 | ··· | ··· | 135.5 | 81.8 | 00 | N |
| ZS75 | 00:03:00.28 | -30:03:21.6 | 12.82±0.004 | 1.03±0.006 | 0.91±0.009 | 29.58 | -3.65 | 29.67 | -3.57 | 21.5 | 3.9 | 91 | Y |
| BLX-34 | 00:03:00.56 | -30:15:44.0 | 15.64±0.044 | 1.81±0.050 | ··· | 29.36 | -3.17 | ··· | ··· | 21.0 | 1.6 | 33 | Y |
| ZS71 | 00:03:02.95 | -29:47:44.1 | 14.90±0.025 | 1.92±0.028 | 1.34±0.085 | 29.52 | -3.35 | 29.90 | -2.97 | 21.2 | 3.6 | 80 | Y |
| ZS88 | 00:03:06.63 | -29:43:11.5 | 13.97±0.011 | 1.46±0.014 | 1.21±0.033 | 29.76 | -3.19 | ··· | ··· | 21.1 | 5.0 | 45 | Y |
| ZS83[j] | 00:03:07.09 | -30:15:17.1 | 12.51±0.003 | 0.92±0.005 | 0.85±0.007 | 29.36 | -3.97 | ··· | ··· | 21.9 | 2.6 | 94 | Y |
| ZS84 | 00:03:10.81 | -30:10:49.0 | 11.28±0.002 | 0.62±0.003 | 0.53±0.003 | 29.54 | -4.21 | 29.66 | -4.09 | 23.2 | 3.9 | 82 | Y |
| ZS95 | 00:03:16.49 | -29:58:47.4 | 12.38±0.003 | 0.93±0.005 | 0.90±0.007 | 28.92 | -4.49 | 29.25 | -4.16 | 20.1 | 2.7 | 60 | Y |
| ZS91 | 00:03:20.61 | -29:49:22.8 | 11.25±0.002 | 0.61±0.003 | 0.52±0.003 | 29.47 | -4.29 | 29.40 | -4.36 | 22.1 | 2.5 | 95 | Y |
| ZS96[h] | 00:03:21.85 | -30:01:10.5 | 10.32±0.001 | 0.48±0.001 | 0.39±0.001 | 29.50 | -4.62 | 29.50 | -4.61 | 20.8 | 3.5 | 92 | Y |
| BLX-42[g] | 00:03:22.73 | -29:53:50.5 | 16.50±0.104 | 2.28±0.109 | ··· | 29.41 | -2.97 | 29.43 | -2.96 | 23.0 | 7.4 | 02 | Y |
| ZS94 | 00:03:24.18 | -29:56:22.9 | 14.98±0.025 | 1.55±0.030 | 1.30±0.083 | 28.73 | -3.89 | 29.13 | -3.48 | 22.3 | 3.3 | 79 | Y |
| ZS90 | 00:03:24.39 | -29:48:49.4 | 10.62±0.001 | 0.54±0.002 | 0.45±0.001 | 29.57 | -4.44 | 29.73 | -4.27 | 20.7 | 3.5 | 90 | Y |
| ZS93 | 00:03:24.67 | -29:55:14.7 | 14.18±0.013 | 1.21±0.017 | 1.12±0.035 | 29.28 | -3.53 | 29.44 | -3.37 | 22.2 | 2.4 | 83 | Y |
| ZS104 | 00:03:31.89 | -29:43:04.8 | 10.05±0.001 | 0.46±0.001 | 0.36±0.001 | 29.75 | -4.47 | ··· | ··· | 22.8 | 3.0 | 95 | Y |
| PMS04-70 | 00:03:39.79 | -30:02:09.5 | 11.37±0.002 | 0.58±0.003 | 0.49±0.003 | ··· | ··· | 28.59 | -5.12 | -4.9 | -4.6 | 00 | N |
| ZS107[i] | 00:03:50.17 | -30:03:55.7 | 11.02±0.001 | 0.58±0.002 | 0.49±0.002 | ··· | ··· | 28.95 | -4.88 | 22.0 | 2.9 | 97 | Y |
| ZS115 | 00:04:12.57 | -29:58:02.5 | 14.88±0.024 | 1.79±0.027 | 1.46±0.092 | 29.99 | -2.84 | ··· | ··· | 21.7 | 4.3 | 70 | Y |
| ZS134 | 00:04:49.20 | -30:00:52.9 | 11.09±0.001 | 0.57±0.002 | 0.49±0.002 | 29.78 | -4.04 | ··· | ··· | 23.4 | 5.0 | 29 | Y |
| ZS138 | 00:04:58.84 | -30:09:41.6 | 11.47±0.002 | 0.64±0.003 | 0.56±0.003 | 29.34 | -4.34 | ··· | ··· | 22.4 | 2.6 | 95 | Y |
| ZS142 | 00:05:04.93 | -30:19:39.2 | 15.60±0.045 | 2.77±0.046 | 1.42±0.159 | 29.69 | -3.29 | ··· | ··· | 99.1 | 1.2 | 00 | N |

Continued on Next Page...

Table B.1 – Continued

| ID[a] | R.A.[b] [HH:MM:SS] | Dec.[b] [DD:MM:SS] | $V_0$[c] | $(V-I_c)_0$[c] | $(B-V)_0$[c] | ROSAT $LogL_x$[d] | ROSAT $Log\ L_x/L_{bol}$ | XMM-Newton $LogL_x$[d] | XMM-Newton $Log\ L_x/L_{bol}$ | $\mu_\alpha \cos\delta$[e] | $\mu_\delta$[e] | $P_\mu$[e] | P.M.[f] Mem. |
|---|---|---|---|---|---|---|---|---|---|---|---|---|---|
| BLX-62 | 00:05:07.01 | -30:04:29.3 | 14.78±0.021 | 0.74±0.034 | 0.57±0.037 | 29.26 | -3.10 | ··· | ··· | 8.7 | -6.8 | 00 | N |
| ZS144 | 00:05:07.08 | -29:59:25.7 | 15.26±0.032 | 1.77±0.037 | 1.28±0.103 | 29.55 | -3.12 | ··· | ··· | 21.8 | 5.0 | 33 | Y |
| ZS148 | 00:05:14.39 | -29:54:23.8 | 12.35±0.003 | 0.90±0.005 | 0.84±0.006 | 29.48 | -3.91 | ··· | ··· | 22.8 | 4.0 | 87 | Y |
| ZS154[j] | 00:05:31.58 | -30:20:51.6 | 13.42±0.007 | 1.07±0.010 | 0.96±0.016 | 29.56 | -3.46 | ··· | ··· | 22.0 | 2.2 | 84 | Y |
| ZS165[h] | 00:05:35.53 | -29:57:06.4 | 12.50±0.003 | ··· | 0.85±0.007 | 29.41 | -3.93 | ··· | ··· | 21.0 | 3.8 | 89 | Y |
| ZS170 | 00:05:54.72 | -30:06:25.8 | 12.07±0.003 | 0.74±0.004 | 0.69±0.005 | 29.17 | -4.29 | ··· | ··· | 22.0 | 2.5 | 94 | Y |
| BLX-79 | 00:05:58.13 | -30:11:09.0 | 16.63±0.112 | 2.19±0.119 | ··· | 28.94 | -3.36 | ··· | ··· | 27.5 | -5.8 | 00 | N |
| ZS172 | 00:06:04.29 | -30:02:11.9 | 15.88±0.058 | 1.86±0.064 | ··· | 29.07 | -3.39 | ··· | ··· | 21.3 | 3.2 | 49 | Y |
| BLX-81 | 00:06:04.73 | -29:57:06.7 | 15.74±0.051 | 0.92±0.076 | 0.92±0.117 | 29.33 | -2.74 | ··· | ··· | 0.4 | -12.8 | 00 | N |
| ZS182 | 00:06:16.35 | -30:05:57.1 | 11.66±0.002 | 0.68±0.004 | 0.61±0.004 | 29.27 | -4.34 | ··· | ··· | 21.7 | 3.0 | 96 | Y |
| ZS184 | 00:06:23.70 | -29:52:04.7 | 15.58±0.049 | 2.91±0.050 | ··· | 29.75 | -3.31 | ··· | ··· | 38.2 | -78.1 | 00 | N |

[a] Naming convention is as follows: ZS from de Epstein & Epstein (1985), BLX from M99 and, PMS04 from P04.

[b] Coordinates are taken from the optical counterpart given in our SPOCS survey and are J2000.

[c] Intrinsic vales are derived using $E(B-V) = 0.016$ and $E(V-I_c) = 0.02$.

[d] Distance used for luminosity calculation is 240 parsecs (see Chapter 3.4); unabsorbed luminosities are in erg $s^{-1}$.

[e] Proper motions and probabilities are taken from our SPOCS survey; proper motions are in mas $yr^{-1}$.

[f] Membership based on new proper motions. Y=proper motion member, N=proper motion non-member, NA=not available due to limiting magnitude of proper motion survey.

[g] Identical optical counterparts that are identified as two separate X-ray sources in M99 and P04 (see Table IV.1).

[h] Listed as single-line spectroscopic binary in Mermilliod et al. (2008).

[i] Listed as double-line spectroscopic binary in Mermilliod et al. (2008).

[j] Listed as a single-line spectroscopic binary in Jeffries & James (1999).

## References


Alexander, D. R. & J. W. Ferguson, 1994: Low-temperature Rosseland opacities. ApJ, **437**, 879–891.

Allain, S., J. Bouvier, C. Prosser, L. A. Marschall, & B. D. Laaksonen, 1996: Rotational periods and starspot activity of young solar-type dwarfs in the open cluster IC 4665. A&A, **305**, 498–+.

Bagnuolo, W. G., Jr. & D. R. Gies, 1991: Tomographic separation of composite spectra - The components of the O-star spectroscopic binary AO Cassiopeiae. ApJ, **376**, 266–271.

Baraffe, I., G. Chabrier, F. Allard, & P. H. Hauschildt, 1998: Evolutionary models for solar metallicity low-mass stars: mass-magnitude relationships and color-magnitude diagrams. A&A, **337**, 403–412.

—, 2002: Evolutionary models for low-mass stars and brown dwarfs: Uncertainties and limits at very young ages. A&A, **382**, 563–572.

Barnes, S. A., 2003: On the Rotational Evolution of Solar- and Late-Type Stars, Its Magnetic Origins, and the Possibility of Stellar Gyrochronology. ApJ, **586**, 464–479.

—, 2007: Ages for Illustrative Field Stars Using Gyrochronology: Viability, Limitations, and Errors. ApJ, **669**, 1167–1189.

Barrado y Navascués, D., J. R. Stauffer, & R. Jayawardhana, 2004: Spectroscopy of Very Low Mass Stars and Brown Dwarfs in IC 2391: Lithium Depletion and H$\alpha$ Emission. ApJ, **614**, 386–397.

Barrado y Navascués, D., J. R. Stauffer, & B. M. Patten, 1999: The Lithium-Depletion Boundary and the Age of the Young Open Cluster IC 2391. ApJ, **522**, L53–L56.

Bessell, M. S., F. Castelli, & B. Plez, 1998: Model atmospheres broad-band colors, bolometric corrections and temperature calibrations for O - M stars. A&A, **333**, 231–250.

Bessell, M. S. & E. W. Weis, 1987: The Cousins and Kron VRI systems. PASP, **99**, 642–644.

Bildsten, L., E. F. Brown, C. D. Matzner, & G. Ushomirsky, 1997: Lithium Depletion in Fully Convective Pre-Main-Sequence Stars. ApJ, **482**, 442–+.

Boesgaard, A. M. & E. D. Friel, 1990: Chemical composition of open clusters. I - Fe/H from high-resolution spectroscopy. ApJ, **351**, 467–479.

Böhm-Vitense, E., 1958: Über die Wasserstoffkonvektionszone in Sternen verschiedener Effektivtemperaturen und Leuchtkräfte. Mit 5 Textabbildungen. *Zeitschrift fur Astrophysik*, **46**, 108–+.

Bouvier, J., T. Kendall, G. Meeus, L. Testi, E. Moraux, J. R. Stauffer, D. James, J. Cuillandre, J. Irwin, M. J. McCaughrean, I. Baraffe, & E. Bertin, 2008: Brown dwarfs and very low mass stars in the Hyades cluster: a dynamically evolved mass function. A&A, **481**, 661–672.

Burke, C. J., M. H. Pinsonneault, & A. Sills, 2004: Theoretical Examination of the Lithium Depletion Boundary. ApJ, **604**, 272–283.

Canuto, V. M. & I. Mazzitelli, 1991: Stellar turbulent convection - A new model and applications. ApJ, **370**, 295–311.

—, 1992: Further improvements of a new model for turbulent convection in stars. ApJ, **389**, 724–730.

Cargile, P. A., D. J. James, & I. Platais, 2009: A New X-Ray Analysis of the Open Cluster Blanco 1 Using Wide-Field BVIc Photometric and Proper Motion Surveys. AJ, **137**, 3230–3244.

Cargile, P. A., K. G. Stassun, & R. D. Mathieu, 2008: Discovery of Par 1802 as a Low-Mass, Pre-Main-Sequence Eclipsing Binary in the Orion Star-Forming Region. ApJ, **674**, 329–335.

Carpenter, J. M., L. A. Hillenbrand, & M. F. Skrutskie, 2001: Near-Infrared Photometric Variability of Stars toward the Orion A Molecular Cloud. AJ, **121**, 3160–3190.

Caughlan, G. R. & W. A. Fowler, 1988: Thermonuclear Reaction Rates V. *Atomic Data and Nuclear Data Tables*, **40**, 283–+.

Chabrier, G. & I. Baraffe, 1997: Structure and evolution of low-mass stars. A&A, **327**, 1039–1053.

—, 2000: Theory of Low-Mass Stars and Substellar Objects. ARA&A, **38**, 337–377.

Chabrier, G., I. Baraffe, & B. Plez, 1996: Mass-Luminosity Relationship and Lithium Depletion for Very Low Mass Stars. ApJ, **459**, L91+.

Chabrier, G., J. Gallardo, & I. Baraffe, 2007: Evolution of low-mass star and brown dwarf eclipsing binaries. A&A, **472**, L17–L20.

Charbonneau, P. & K. B. MacGregor, 1992: Angular momentum transport in magnetized stellar radiative zones. I - Numerical solutions to the core spin-up model problem. ApJ, **387**, 639–661.

Chiosi, C., G. Bertelli, & A. Bressan, 1992: New developments in understanding the HR diagram. ARA&A, **30**, 235–285.

Collier Cameron, A., D. K. Bedford, S. M. Rucinski, O. Vilhu, & N. E. White, 1988: EXOSAT observations of variable coronal X-ray emission from the young K dwarf AB Doradus (= HD 36705). MNRAS, **231**, 131–147.

D'Antona, F. & I. Mazzitelli, 1994: New pre-main-sequence tracks for M less than or equal to 2.5 solar mass as tests of opacities and convection model. ApJS, **90**, 467–500.

—, 1997: Evolution of low mass stars. *Memorie della Societa Astronomica Italiana*, **68**, 807–+.

de Epstein, A. E. A. & I. Epstein, 1985: Photometric study of Zeta SCULPTORIS cluster. AJ, **90**, 1211–1223.

de Wit, W. J., J. Bouvier, F. Palla, J.-C. Cuillandre, D. J. James, T. R. Kendall, N. Lodieu, M. J. McCaughrean, E. Moraux, S. Randich, & L. Testi, 2006: Exploring the lower mass function in the young open cluster IC 4665. A&A, **448**, 189–202.

Demarque, P. R. & R. B. Larson, 1964: The Age of Galactic Cluster NGC 188. ApJ, **140**, 544–+.

Dolan, C. J. & R. D. Mathieu, 1999: A WIYN Lithium Survey for Young Stars in the $\lambda$ Orionis Star-Forming Region. AJ, **118**, 2409–2423.

Edvardsson, B., B. Pettersson, M. Kharrazi, & B. Westerlund, 1995: Abundance analysis and origin of the $\zeta$ SCULPTORIS open cluster. A&A, **293**, 75–86.

Ezer, D. & A. G. W. Cameron, 1967a: Early and main sequence evolution of stars in the range 0.5 to 100 solar masses. *Canadian Journal of Physics*, **45**, 3429–+.

—, 1967b: Evolution of stars of low mass. *Canadian Journal of Physics*, **45**, 3461–+.

Feigelson, E. D., P. Broos, J. A. Gaffney, III, G. Garmire, L. A. Hillenbrand, S. H. Pravdo, L. Townsley, & Y. Tsuboi, 2002: X-Ray-emitting Young Stars in the Orion Nebula. ApJ, **574**, 258–292.

Feigelson, E. D., K. Getman, L. Townsley, G. Garmire, T. Preibisch, N. Grosso, T. Montmerle, A. Muench, & M. McCaughrean, 2005: Global X-Ray Properties of the Orion Nebula Region. ApJS, **160**, 379–389.

Fleming, T. A., M. S. Giampapa, J. H. M. M. Schmitt, & J. A. Bookbinder, 1993: Stellar coronae at the end of the main sequence - A ROSAT survey of the late M dwarfs. ApJ, **410**, 387–392.

Flower, P. J., 1996: Transformations from Theoretical Hertzsprung-Russell Diagrams to Color-Magnitude Diagrams: Effective Temperatures, B-V Colors, and Bolometric Corrections. ApJ, **469**, 355–+.

Ford, A., R. D. Jeffries, & B. Smalley, 2005: Elemental abundances in the Blanco 1 open cluster. MNRAS, **364**, 272–282.

Forestini, M., 1994: Low-mass stars: pre-main sequence evolution and nucleosynthesis. A&A, **285**, 473–488.

Fowler, W. A., G. R. Caughlan, & B. A. Zimmerman, 1975: Thermonuclear Reaction Rates, II. ARA&A, **13**, 69–+.

Genzel, R. & J. Stutzki, 1989: The Orion Molecular Cloud and star-forming region. ARA&A, **27**, 41–85.

Giampapa, M. S., C. F. Prosser, & T. A. Fleming, 1998: X-Ray Activity in the Open Cluster IC 4665. ApJ, **501**, 624–+.

Gilman, P. A., 1983: Dynamically consistent nonlinear dynamos driven by convection in a rotating spherical shell. II - Dynamos with cycles and strong feedbacks. ApJS, **53**, 243–268.

Girardi, L., G. Bertelli, A. Bressan, C. Chiosi, M. A. T. Groenewegen, P. Marigo, B. Salasnich, & A. Weiss, 2002: Theoretical isochrones in several photometric systems. I. Johnson-Cousins-Glass, HST/WFPC2, HST/NICMOS, Washington, and ESO Imaging Survey filter sets. A&A, **391**, 195–212.

Girardi, L., A. Bressan, G. Bertelli, & C. Chiosi, 2000: Evolutionary tracks and isochrones for low- and intermediate-mass stars: From 0.15 to 7 Msun, and from Z=0.0004 to 0.03. A&AS, **141**, 371–383.

Gomez Maqueo Chew, Y., 2010: Young, Eclipsing Binary Systems. In *American Astronomical Society Meeting Abstracts*, vol. 215 of *American Astronomical Society Meeting Abstracts*, p. 335.02.

Güdel, M., 2004: X-ray astronomy of stellar coronae. A&A Rev., **12**, 71–237.

Hambly, N. C., H. T. MacGillivray, M. A. Read, S. B. Tritton, E. B. Thomson, B. D. Kelly, D. H. Morgan, R. E. Smith, S. P. Driver, J. Williamson, Q. A. Parker, M. R. S. Hawkins, P. M. Williams, & A. Lawrence, 2001: The SuperCOSMOS Sky Survey - I. Introduction and description. MNRAS, **326**, 1279–1294.

Hauschildt, P. H., F. Allard, & E. Baron, 1999: The NextGen Model Atmosphere Grid for 3000<Teff<10,000 K. ApJ, **512**, 377–385.

Hayashi, C., 1961: Stellar evolution in early phases of gravitational contraction. PASJ, **13**, 450–452.

Henry, T. J. & D. W. McCarthy, Jr., 1993: The mass-luminosity relation for stars of mass 1.0 to 0.08 solar mass. AJ, **106**, 773–789.

Henyey, L. G., R. Lelevier, & R. D. Levée, 1955: The Early Phases of Stellar Evolution. PASP, **67**, 154–+.

Herbig, G. H. & K. R. Bell, 1988: *Third Catalog of Emission-Line Stars of the Orion Population : 3 : 1988*.

Herbig, G. H. & B. F. Jones, 1981: Large proper motions of the Herbig-Haro objects HH 1 and HH 2. AJ, **86**, 1232–1244.

Hillenbrand, L. A., 1997: On the Stellar Population and Star-Forming History of the Orion Nebula Cluster. AJ, **113**, 1733–1768.

Hillenbrand, L. A. & L. W. Hartmann, 1998: A Preliminary Study of the Orion Nebula Cluster Structure and Dynamics. ApJ, **492**, 540–+.

Hillenbrand, L. A. & R. J. White, 2004: An Assessment of Dynamical Mass Constraints on Pre-Main-Sequence Evolutionary Tracks. ApJ, **604**, 741–757.

Hook, I. M., I. Jørgensen, J. R. Allington-Smith, R. L. Davies, N. Metcalfe, R. G. Murowinski, & D. Crampton, 2004: The Gemini-North Multi-Object Spectrograph: Performance in Imaging, Long-Slit, and Multi-Object Spectroscopic Modes. PASP, **116**, 425–440.

Iben, I., Jr., 1965: Stellar Evolution. I. The Approach to the Main Sequence. ApJ, **141**, 993–+.

—, 1967: Stellar Evolution Within and off the Main Sequence. ARA&A, **5**, 571–+.

Irwin, J., S. Aigrain, S. Hodgkin, K. G. Stassun, L. Hebb, M. Irwin, E. Moraux, J. Bouvier, A. Alapini, R. Alexander, D. M. Bramich, J. Holtzman, E. L. Martín, M. J. McCaughrean, F. Pont, P. E. Verrier, & M. R. Zapatero Osorio, 2007: The Monitor project: JW 380 - a 0.26-, 0.15-Msol, pre-main-sequence eclipsing binary in the Orion nebula cluster. MNRAS, **380**, 541–550.

Irwin, J., S. Hodgkin, S. Aigrain, J. Bouvier, L. Hebb, & E. Moraux, 2008: The Monitor project: rotation of low-mass stars in the open cluster NGC 2547. MNRAS, **383**, 1588–1602.

James, D. J., P. A. Cargile, J. Mermilliod, C. Deliyannis, I. Platais, & A. Steinhauer, 2010: SMARTS UBVIc Photometry of Southern Open Cluster Blanco 1. *in prep.*.

James, D. J., M. M. Jardine, R. D. Jeffries, S. Randich, A. Collier Cameron, & M. Ferreira, 2000: X-ray emission from nearby M-dwarfs: the super-saturation phenomenon. MNRAS, **318**, 1217–1226.

Jansen, F., D. Lumb, B. Altieri, J. Clavel, M. Ehle, C. Erd, C. Gabriel, M. Guainazzi, P. Gondoin, R. Much, R. Munoz, M. Santos, N. Schartel, D. Texier, & G. Vacanti, 2001: XMM-Newton observatory. I. The spacecraft and operations. A&A, **365**, L1–L6.

Jardine, M. & Y. C. Unruh, 1999: Coronal emission and dynamo saturation. A&A, **346**, 883–891.

Jeffries, R. D., P. A. Evans, J. P. Pye, & K. R. Briggs, 2006: An XMM-Newton observation of the young open cluster NGC 2547: coronal activity at 30 Myr. MNRAS, **367**, 781–800.

Jeffries, R. D., R. J. Jackson, D. J. James, & P. A. Cargile, 2009a: Low-mass members of the young cluster IC 4665 and pre-main-sequence lithium depletion. MNRAS, **400**, 317–329.

Jeffries, R. D. & D. J. James, 1999: Lithium in Blanco 1: Implications for Stellar Mixing. ApJ, **511**, 218–224.

Jeffries, R. D., T. Naylor, F. M. Walter, M. P. Pozzo, & C. R. Devey, 2009b: The stellar association around Gamma Velorum and its relationship with Vela OB2. MNRAS, **393**, 538–556.

Jeffries, R. D. & J. M. Oliveira, 2005: The lithium depletion boundary in NGC 2547 as a test of pre-main-sequence evolutionary models. MNRAS, **358**, 13–29.

Jeffries, R. D., J. M. Oliveira, T. Naylor, N. J. Mayne, & S. P. Littlefair, 2007: The Keele-Exeter young cluster survey - I. Low-mass pre-main-sequence stars in NGC 2169. MNRAS, **376**, 580–598.

Jeffries, R. D., M. R. Thurston, & N. C. Hambly, 2001: Photometry and membership for low mass stars in the young open cluster NGC 2516. A&A, **375**, 863–889.

Jeffries, R. D., M. R. Thurston, & J. P. Pye, 1997: An X-ray survey of the young open cluster NGC 2516. MNRAS, **287**, 350–380.

Johnson, H. L., 1966: Astronomical Measurements in the Infrared. ARA&A, **4**, 193–+.

Jones, B. F. & M. F. Walker, 1988: Proper motions and variabilities of stars near the Orion Nebula. AJ, **95**, 1755–1782.

Joshi, H., B. Kumar, K. P. Singh, R. Sagar, S. Sharma, & J. C. Pandey, 2008: Multiwavelength study of a young open cluster NGC7419. MNRAS, **391**, 1279–1300.

Kawaler, S. D., 1988: Angular momentum loss in low-mass stars. ApJ, **333**, 236–247.

Kazarovets, E. V. & N. N. Samus, 1997: The 73rd Name-List of Variable Stars. *Information Bulletin on Variable Stars*, **4471**, 1–+.

Kenyon, S. J. & L. Hartmann, 1995: Pre-Main-Sequence Evolution in the Taurus-Auriga Molecular Cloud. ApJS, **101**, 117–+.

Koutchmy, S., F. Baudin, K. Bocchialini, J. Daniel, J. Delaboudinière, L. Golub, P. Lamy, & A. Adjabshirizadeh, 2004: The August 11th, 1999 CME. A&A, **420**, 709–718.

Kraft, R. P., 1967: Studies of Stellar Rotation. V. The Dependence of Rotation on Age among Solar-Type Stars. ApJ, **150**, 551–+.

Krauss, L. M. & B. Chaboyer, 2003: Age Estimates of Globular Clusters in the Milky Way: Constraints on Cosmology. *Science*, **299**, 65–70.

Krishnamurthi, A., M. H. Pinsonneault, S. Barnes, & S. Sofia, 1997: Theoretical Models of the Angular Momentum Evolution of Solar-Type Stars. ApJ, **480**, 303–+.

Kurucz, R. L., 1991: New Opacity Calculations. In *NATO ASIC Proc. 341: Stellar Atmospheres - Beyond Classical Models*, pp. 441–+.

Landolt, A. U., 1983: UBVRI photometric standard stars around the celestial equator. AJ, **88**, 439–460.

—, 1992: UBVRI photometric standard stars in the magnitude range 11.5-16.0 around the celestial equator. AJ, **104**, 340–371.

—, 2009: UBVRI Photometric Standard Stars Around the Celestial Equator: Updates and Additions. AJ, **137**, 4186–4269.

Lang, D., D. W. Hogg, K. Mierle, M. Blanton, & S. Roweis, 2009: Astrometry.net: Blind astrometric calibration of arbitrary astronomical images. *ArXiv e-prints*.

Latham, D. W., B. Nordstroem, J. Andersen, G. Torres, R. P. Stefanik, M. Thaller, & M. J. Bester, 1996: Accurate mass determination for double-lined spectroscopic binaries by digital cross-correlation spectroscopy: DM Virginis revisited. A&A, **314**, 864–870.

Lejeune, T. & D. Schaerer, 2001: Database of Geneva stellar evolution tracks and isochrones for UBVRIJHKLL'M, HST-WFPC2, Geneva and Washington photometric systems. A&A, **366**, 538–546.

Maeder, A. & J. C. Mermilliod, 1981: The extent of mixing in stellar interiors - Evolutionary models and tests based on the HR diagrams of 34 open clusters. A&A, **93**, 136–149.

Makarov, V. V., 2002: The Rate of Visual Binaries among the Brightest X-Ray Stars. ApJ, **576**, L61–L64.

Mangeney, A. & F. Praderie, 1984: The influence of convection and rotation on X-ray emission in main sequence stars. A&A, **130**, 143–150.

Manzi, S., S. Randich, W. J. de Wit, & F. Palla, 2008: Detection of the lithium depletion boundary in the young open cluster IC 4665. A&A, **479**, 141–148.

Marino, A., G. Micela, G. Peres, & S. Sciortino, 2003: X-ray variability of Pleiades late-type stars as observed with the ROSAT-PSPC. A&A, **406**, 629–638.

Martin, E. L. & D. Montes, 1997: H$\alpha$ emission fluxes and lithium abundances of low-mass stars in the young open cluster IC 4665. A&A, **318**, 805–811.

Mayne, N. J. & T. Naylor, 2008: Fitting the young main-sequence: distances, ages and age spreads. MNRAS, **386**, 261–277.

Menzies, J. W. & F. Marang, 1996: UBVRIc observations of Johnson's standard sequence in IC 4665. MNRAS, **282**, 313–316.

Mermilliod, J. C., 1981a: Comparative Studies of Young Open Clusters - Part Two - an Atlas of Composite Colour-Magnitude Diagrams. A&AS, **44**, 467–+.

—, 1981b: Comparative studies of young open clusters. III - Empirical isochronous curves and the zero age main sequence. A&A, **97**, 235–244.

Mermilliod, J.-C., I. Platais, D. J. James, M. Grenon, & P. A. Cargile, 2008: Membership, binarity, and rotation of F-G-K stars in the open cluster Blanco 1. A&A, **485**, 95–105.

Mestel, L., 1968: Magnetic braking by a stellar wind-I. MNRAS, **138**, 359–+.

Meynet, G. & A. Maeder, 1997: Stellar evolution with rotation. I. The computational method and the inhibiting effect of the $\mu$-gradient. A&A, **321**, 465–476.

—, 2000: Stellar evolution with rotation. V. Changes in all the outputs of massive star models. A&A, **361**, 101–120.

Meynet, G., J.-C. Mermilliod, & A. Maeder, 1993: New dating of galactic open clusters. A&AS, **98**, 477–504.

Micela, G., S. Sciortino, F. Favata, R. Pallavicini, & J. Pye, 1999a: X-ray observations of the young open cluster Blanco 1. A&A, **344**, 83–96.

Micela, G., S. Sciortino, F. R. Harnden, Jr., V. Kashyap, R. Rosner, C. F. Prosser, F. Damiani, J. Stauffer, & J. Caillault, 1999b: Deep ROSAT HRI observations of the Pleiades. A&A, **341**, 751–767.

Mihalas, D., W. Dappen, & D. G. Hummer, 1988: The equation of state for stellar envelopes. II - Algorithm and selected results. ApJ, **331**, 815–825.

Monet, D. G., C. C. Dahn, F. J. Vrba, H. C. Harris, J. R. Pier, C. B. Luginbuhl, & H. D. Ables, 1992: U.S. Naval Observatory CCD parallaxes of faint stars. I - Program description and first results. AJ, **103**, 638–665.

Montalbán, J., F. D'Antona, F. Kupka, & U. Heiter, 2004: Convection in the atmospheres and envelopes of Pre-Main Sequence stars. A&A, **416**, 1081–1096.

Moraux, E., J. Bouvier, J. R. Stauffer, D. Barrado y Navascués, & J.-C. Cuillandre, 2007: The lower mass function of the young open cluster Blanco 1: from 30 MJup to 3 Msun. A&A, **471**, 499–513.

Naylor, T., 2009: Are pre-main-sequence stars older than we thought? MNRAS, **399**, 432–442.

Naylor, T. & R. D. Jeffries, 2006: A maximum-likelihood method for fitting colour-magnitude diagrams. MNRAS, **373**, 1251–1263.

Naylor, T., E. J. Totten, R. D. Jeffries, M. Pozzo, C. R. Devey, & S. A. Thompson, 2002: Optimal photometry for colour-magnitude diagrams and its application to NGC 2547. MNRAS, **335**, 291–310.

Noyes, R. W., L. W. Hartmann, S. L. Baliunas, D. K. Duncan, & A. H. Vaughan, 1984: Rotation, convection, and magnetic activity in lower main-sequence stars. ApJ, **279**, 763–777.

Palla, F. & S. W. Stahler, 1999: Star Formation in the Orion Nebula Cluster. ApJ, **525**, 772–783.

Pallavicini, R., L. Golub, R. Rosner, G. S. Vaiana, T. Ayres, & J. L. Linsky, 1981: Relations among stellar X-ray emission observed from Einstein, stellar rotation and bolometric luminosity. ApJ, **248**, 279–290.

Parenago, P. P., 1954: Catalogue of stars in the area of the Orion Nebula. *Trudy Gosudarstvennogo Astronomicheskogo Instituta*, **25**, 1–+.

Parker, E. N., 1960: The Hydrodynamic Theory of Solar Corpuscular Radiation and Stellar Winds. ApJ, **132**, 821–+.

Patten, B. M. & T. Simon, 1996: The Evolution of Rotation and Activity in Young Open Clusters: IC 2391. ApJS, **106**, 489–+.

Perryman, M. A. C., A. G. A. Brown, Y. Lebreton, A. Gomez, C. Turon, G. Cayrel de Strobel, J. C. Mermilliod, N. Robichon, J. Kovalevsky, & F. Crifo, 1998: The Hyades: distance, structure, dynamics, and age. A&A, **331**, 81–120.

Pillitteri, I., G. Micela, F. Damiani, & S. Sciortino, 2006: Deep X-ray survey of the young open cluster NGC 2516 with XMM-Newton. A&A, **450**, 993–1004.

Pillitteri, I., G. Micela, F. Reale, & S. Sciortino, 2005: XMM-Newton observation of the young open cluster Blanco 1. II. X-ray time variability and flares. A&A, **430**, 155–164.

Pillitteri, I., G. Micela, S. Sciortino, F. Damiani, & F. R. Harnden, Jr., 2004: XMM-Newton observations of the young open cluster Blanco 1. I. X-ray spectroscopy and photometry. A&A, **421**, 175–186.

Pillitteri, I., G. Micela, S. Sciortino, & F. Favata, 2003: The X-ray Luminosity Distributions of the high-metallicity open cluster Blanco 1. A&A, **399**, 919–929.

Pizzolato, N., A. Maggio, G. Micela, S. Sciortino, & P. Ventura, 2003: The stellar activity-rotation relationship revisited: Dependence of saturated and non-saturated X-ray emission regimes on stellar mass for late-type dwarfs. A&A, **397**, 147–157.

Platais, I., C. Melo, J. Mermilliod, V. Kozhurina-Platais, J. P. Fulbright, R. A. Méndez, M. Altmann, & J. Sperauskas, 2007: WIYN open cluster study. XXVI. Improved kinematic membership and spectroscopy of IC 2391. A&A, **461**, 509–522.

Plez, B., 1992: Spherical opacity sampling model atmospheres for M-giants and supergiants. II - A grid. A&AS, **94**, 527–552.

Pourbaix, D., A. A. Tokovinin, A. H. Batten, F. C. Fekel, W. I. Hartkopf, H. Levato, N. I. Morrell, G. Torres, & S. Udry, 2004: Sb9: The ninth catalogue of spectroscopic binary orbits. A&A, **424**, 727–732.

Prato, L., M. Simon, T. Mazeh, S. Zucker, & I. S. McLean, 2002: Component Masses of the Young Spectroscopic Binary UZ Tau E. ApJ, **579**, L99–L102.

Prosser, C. F., 1993: The open cluster IC 4665. AJ, **105**, 1441–1454.

Prosser, C. F. & M. S. Giampapa, 1994: A radial velocity survey of the open cluster IC 4665. AJ, **108**, 964–969.

Prosser, C. F., S. Randich, J. R. Stauffer, J. H. M. M. Schmitt, & T. Simon, 1996: ROSAT Pointed Observations of the Alpha Persei Cluster. AJ, **112**, 1570–+.

Prosser, C. F., J. R. Stauffer, J.-P. Caillault, S. Balachandran, R. A. Stern, & S. Randich, 1995: An X-Ray Survey of the Open Cluster NGC 6475 (M7) With ROSAT. AJ, **110**, 1229–+.

Prša, A. & T. Zwitter, 2005: A Computational Guide to Physics of Eclipsing Binaries. I. Demonstrations and Perspectives. ApJ, **628**, 426–438.

Pye, J. P., S. T. Hodgkin, R. A. Stern, & J. R. Stauffer, 1994: ROSAT X-ray luminosity functions of the Hyades dK and dM stars. MNRAS, **266**, 798–+.

Queloz, D., S. Allain, J. Mermilliod, J. Bouvier, & M. Mayor, 1998: The rotational velocity of low-mass stars in the Pleiades cluster. A&A, **335**, 183–198.

Randich, S., 1998: Supersaturation in X-ray Emission of Cluster Stars. In R. A. Donahue & J. A. Bookbinder, ed., *Cool Stars, Stellar Systems, and the Sun*, vol. 154 of *Astronomical Society of the Pacific Conference Series*, pp. 501–+.

Randich, S. & J. H. M. M. Schmitt, 1995: A ROSAT X-ray study of the Praesepe cluster. A&A, **298**, 115–+.

Randich, S., J. H. M. M. Schmitt, C. F. Prosser, & J. R. Stauffer, 1995: An X-ray study of the young open cluster IC 2602. A&A, **300**, 134–+.

—, 1996: The X-ray properties of the young open cluster around $\alpha$ Persei. A&A, **305**, 785–+.

Reid, N., 1993: Low-Mass Stars in the Hyades. MNRAS, **265**, 785–+.

Rhode, K. L., W. Herbst, & R. D. Mathieu, 2001: Rotational Velocities and Radii of Pre-Main-Sequence Stars in the Orion Nebula Cluster. AJ, **122**, 3258–3279.

Ribas, I., J. C. Morales, C. Jordi, I. Baraffe, G. Chabrier, & J. Gallardo, 2008: Fundamental properties of low-mass stars. *Memorie della Societa Astronomica Italiana*, **79**, 562–+.

Richards, G. T., X. Fan, H. J. Newberg, M. A. Strauss, D. E. Vanden Berk, D. P. Schneider, B. Yanny, A. Boucher, S. Burles, J. A. Frieman, J. E. Gunn, P. B. Hall, Ž. Ivezić, S. Kent, J. Loveday, R. H. Lupton, C. M. Rockosi, D. J. Schlegel, C. Stoughton, M. SubbaRao, & D. G. York, 2002: Spectroscopic Target Selection in the Sloan Digital Sky Survey: The Quasar Sample. AJ, **123**, 2945–2975.

Sandage, A., 1958: The Color-Magnitude Diagrams of Galactic and Globular Clusters and their Interpretation as Age Groups. *Ricerche Astronomiche*, **5**, 41–+.

Saumon, D., G. Chabrier, & H. M. van Horn, 1995: An Equation of State for Low-Mass Stars and Giant Planets. ApJS, **99**, 713–+.

Savage, B. D. & J. S. Mathis, 1979: Observed properties of interstellar dust. ARA&A, **17**, 73–111.

Schaller, G., D. Schaerer, G. Meynet, & A. Maeder, 1992: New grids of stellar models from 0.8 to 120 solar masses at Z = 0.020 and Z = 0.001. A&AS, **96**, 269–331.

Scholz, A., J. Eisloeffel, & R. Mundt, 2009: Long-term monitoring in IC4665: Fast rotation and weak variability in very low mass objects. *ArXiv e-prints*.

Schwenn, R., 2006: Space Weather: The Solar Perspective. *Living Reviews in Solar Physics*, **3**, 2–+.

Sicilia-Aguilar, A., L. W. Hartmann, A. H. Szentgyorgyi, D. G. Fabricant, G. Fűrész, J. Roll, M. A. Conroy, N. Calvet, S. Tokarz, & J. Hernández, 2005: Accretion, Kinematics, and Rotation in the Orion Nebula Cluster: Initial Results from Hectochelle. AJ, **129**, 363–381.

Siess, L., E. Dufour, & M. Forestini, 2000: An internet server for pre-main sequence tracks of low- and intermediate-mass stars. A&A, **358**, 593–599.

Siess, L., M. Forestini, & C. Dougados, 1997: Synthetic Hertzsprung-Russell diagrams of open clusters. A&A, **324**, 556–565.

Silverstone, M. D., M. R. Meyer, E. E. Mamajek, D. C. Hines, L. A. Hillenbrand, J. Najita, I. Pascucci, J. Bouwman, J. S. Kim, J. M. Carpenter, J. R. Stauffer, D. E. Backman, A. Moro-Martin, T. Henning, S. Wolf, T. Y. Brooke, & D. L. Padgett, 2006: Formation and Evolution of Planetary Systems (FEPS): Primordial Warm Dust Evolution from 3 to 30 Myr around Sun-like Stars. ApJ, **639**, 1138–1146.

Skrutskie, M. F., R. M. Cutri, R. Stiening, M. D. Weinberg, S. Schneider, J. M. Carpenter, C. Beichman, R. Capps, T. Chester, J. Elias, J. Huchra, J. Liebert, C. Lonsdale, D. G. Monet, S. Price, P. Seitzer, T. Jarrett, J. D. Kirkpatrick, J. E. Gizis, E. Howard, T. Evans, J. Fowler, L. Fullmer, R. Hurt, R. Light, E. L. Kopan, K. A. Marsh, H. L. McCallon, R. Tam, S. Van Dyk, & S. Wheelock, 2006: The Two Micron All Sky Survey (2MASS). AJ, **131**, 1163–1183.

Skumanich, A., 1972: Time Scales for CA II Emission Decay, Rotational Braking, and Lithium Depletion. ApJ, **171**, 565–+.

Smecker-Hane, T. A., A. A. Cole, J. S. Gallagher, III, & P. B. Stetson, 2002: The Star Formation History of the Large Magellanic Cloud. ApJ, **566**, 239–244.

Smith, J. A., D. L. Tucker, S. Kent, M. W. Richmond, M. Fukugita, T. Ichikawa, S. Ichikawa, A. M. Jorgensen, A. Uomoto, J. E. Gunn, M. Hamabe, M. Watanabe, A. Tolea, A. Henden, J. Annis, J. R. Pier, T. A. McKay, J. Brinkmann, B. Chen, J. Holtzman, K. Shimasaku, & D. G. York, 2002: The u'g'r'i'z' Standard-Star System. AJ, **123**, 2121–2144.

Soderblom, D. R., E. Nelan, G. F. Benedict, B. McArthur, I. Ramirez, W. Spiesman, & B. F. Jones, 2005: Confirmation of Errors in Hipparcos Parallaxes from Hubble Space Telescope Fine Guidance Sensor Astrometry of the Pleiades. AJ, **129**, 1616–1624.

Soderblom, D. R., J. R. Stauffer, J. D. Hudon, & B. F. Jones, 1993: Rotation and chromospheric emission among F, G, and K dwarfs of the Pleiades. ApJS, **85**, 315–346.

Stassun, K. G., R. D. Mathieu, P. A. Cargile, A. N. Aarnio, E. Stempels, & A. Geller, 2008: Surprising dissimilarities in a newly formed pair of 'identical twin' stars. Nature, **453**, 1079–1082.

Stassun, K. G., R. D. Mathieu, T. Mazeh, & F. J. Vrba, 1999: The Rotation Period Distribution of Pre-Main-Sequence Stars in and around the Orion Nebula. AJ, **117**, 2941–2979.

Stassun, K. G., R. D. Mathieu, & J. A. Valenti, 2006: Discovery of two young brown dwarfs in an eclipsing binary system. Nature, **440**, 311–314.

—, 2007: A Surprising Reversal of Temperatures in the Brown Dwarf Eclipsing Binary 2MASS J05352184-0546085. ApJ, **664**, 1154–1166.

Stassun, K. G., R. D. Mathieu, L. P. R. Vaz, N. Stroud, & F. J. Vrba, 2004: Dynamical Mass Constraints on Low-Mass Pre-Main-Sequence Stellar Evolutionary Tracks: An Eclipsing Binary in Orion with a 1.0 Msol Primary and a 0.7 Msol Secondary. ApJS, **151**, 357–385.

Stauffer, J. R., D. Barrado y Navascués, J. Bouvier, H. L. Morrison, P. Harding, K. L. Luhman, T. Stanke, M. McCaughrean, D. M. Terndrup, L. Allen, & P. Assouad, 1999: Keck Spectra of Brown Dwarf Candidates and a Precise Determination of the Lithium Depletion Boundary in the $\alpha$ Persei Open Cluster. ApJ, **527**, 219–229.

Stauffer, J. R., J. Caillault, M. Gagne, C. F. Prosser, & L. W. Hartmann, 1994: A deep imaging survey of the Pleiades with ROSAT. ApJS, **91**, 625–657.

Stauffer, J. R., M. S. Giampapa, W. Herbst, J. M. Vincent, L. W. Hartmann, & R. A. Stern, 1991: The chromospheric activity of low-mass stars in the Hyades. ApJ, **374**, 142–149.

Stauffer, J. R., L. W. Hartmann, G. G. Fazio, L. E. Allen, B. M. Patten, P. J. Lowrance, R. L. Hurt, L. M. Rebull, R. M. Cutri, S. V. Ramirez, E. T. Young, G. H. Rieke, N. I. Gorlova, J. C. Muzerolle, C. L. Slesnick, & M. F. Skrutskie, 2007: Near- and Mid-Infrared Photometry of the Pleiades and a New List of Substellar Candidate Members. ApJS, **172**, 663–685.

Stauffer, J. R., G. Schultz, & J. D. Kirkpatrick, 1998: Keck Spectra of Pleiades Brown Dwarf Candidates and a Precise Determination of the Lithium Depletion Edge in the Pleiades. ApJ, **499**, L199+.

Stern, R. A., J. H. M. M. Schmitt, & P. T. Kahabka, 1995: ROSAT All-Sky Survey Observations of the Hyades Cluster. ApJ, **448**, 683–+.

Strom, K. M., S. E. Strom, S. Edwards, S. Cabrit, & M. F. Skrutskie, 1989: Circumstellar material associated with solar-type pre-main-sequence stars - A possible constraint on the timescale for planet building. AJ, **97**, 1451–1470.

Swenson, F. J., J. Faulkner, F. J. Rogers, & C. A. Iglesias, 1994: The Hyades lithium problem revisited. ApJ, **425**, 286–302.

Tody, D., 1993: IRAF in the Nineties. In R. J. Hanisch, R. J. V. Brissenden, & J. Barnes, ed., *Astronomical Data Analysis Software and Systems II*, vol. 52 of *Astronomical Society of the Pacific Conference Series*, pp. 173–+.

Tonry, J. & M. Davis, 1979: A survey of galaxy redshifts. I - Data reduction techniques. AJ, **84**, 1511–1525.

Torres, G., J. Andersen, & A. Giménez, 2009: Accurate masses and radii of normal stars: modern results and applications. A&A Rev., 13–+.

Tull, R. G., 1998: High-resolution fiber-coupled spectrograph of the Hobby-Eberly Telescope. In S. D'Odorico, ed., *Society of Photo-Optical Instrumentation Engineers (SPIE) Conference Series*, vol. 3355 of *Presented at the Society of Photo-Optical Instrumentation Engineers (SPIE) Conference*, pp. 387–398.

Ushomirsky, G., C. D. Matzner, E. F. Brown, L. Bildsten, V. G. Hilliard, & P. C. Schroeder, 1998: Light-Element Depletion in Contracting Brown Dwarfs and Pre-Main-Sequence Stars. ApJ, **497**, 253–266.

van Leeuwen, F., 2009: Parallaxes and proper motions for 20 open clusters as based on the new Hipparcos catalogue. A&A, **497**, 209–242.

Vasilevskis, S., A. Klemola, & G. Preston, 1958: Relative proper motions of stars in the region of the open cluster NGC 6633. AJ, **63**, 387–395.

Vilhu, O., 1984: The nature of magnetic activity in lower main sequence stars. A&A, **133**, 117–126.

Vilhu, O. & F. M. Walter, 1987: Chromospheric-coronal activity at saturated levels. ApJ, **321**, 958–966.

Weber, E. J. & L. Davis, Jr., 1967: The Angular Momentum of the Solar Wind. ApJ, **148**, 217–+.

West, A. A., S. L. Hawley, J. J. Bochanski, K. R. Covey, I. N. Reid, S. Dhital, E. J. Hilton, & M. Masuda, 2008: Constraining the Age-Activity Relation for Cool Stars: The Sloan Digital Sky Survey Data Release 5 Low-Mass Star Spectroscopic Sample. AJ, **135**, 785–795.

Westerlund, B. E., K. Lundgren, B. Pettersson, R. Garnier, & J. Breysacher, 1988: UBV and uvby-beta photometry of stars in the region of the Zeta SCULPTORIS cluster. A&AS, **76**, 101–120.

Wilson, O. C., 1966: Stellar Convection Zones, Chromospheres, and Rotation. ApJ, **144**, 695–+.

Yee, J. C. & E. L. N. Jensen, 2010: A Test of Pre-Main-Sequence Lithium Depletion Models. ApJ, **711**, 303–311.

Yi, S. K., Y. Kim, & P. Demarque, 2003: The Y-Squared Stellar Evolutionary Tracks. ApJS, **144**, 259–261.

Yudin, R. V., 2001: Statistical analysis of intrinsic polarization, IR excess and projected rotational velocity distributions of classical Be stars. A&A, **368**, 912–931.

Zacharias, N., S. E. Urban, M. I. Zacharias, G. L. Wycoff, D. M. Hall, D. G. Monet, & T. J. Rafferty, 2004: The Second US Naval Observatory CCD Astrograph Catalog (UCAC2). AJ, **127**, 3043–3059.

Zucker, S. & T. Mazeh, 1994: Study of spectroscopic binaries with TODCOR. 1: A new two-dimensional correlation algorithm to derive the radial velocities of the two components. ApJ, **420**, 806–810.